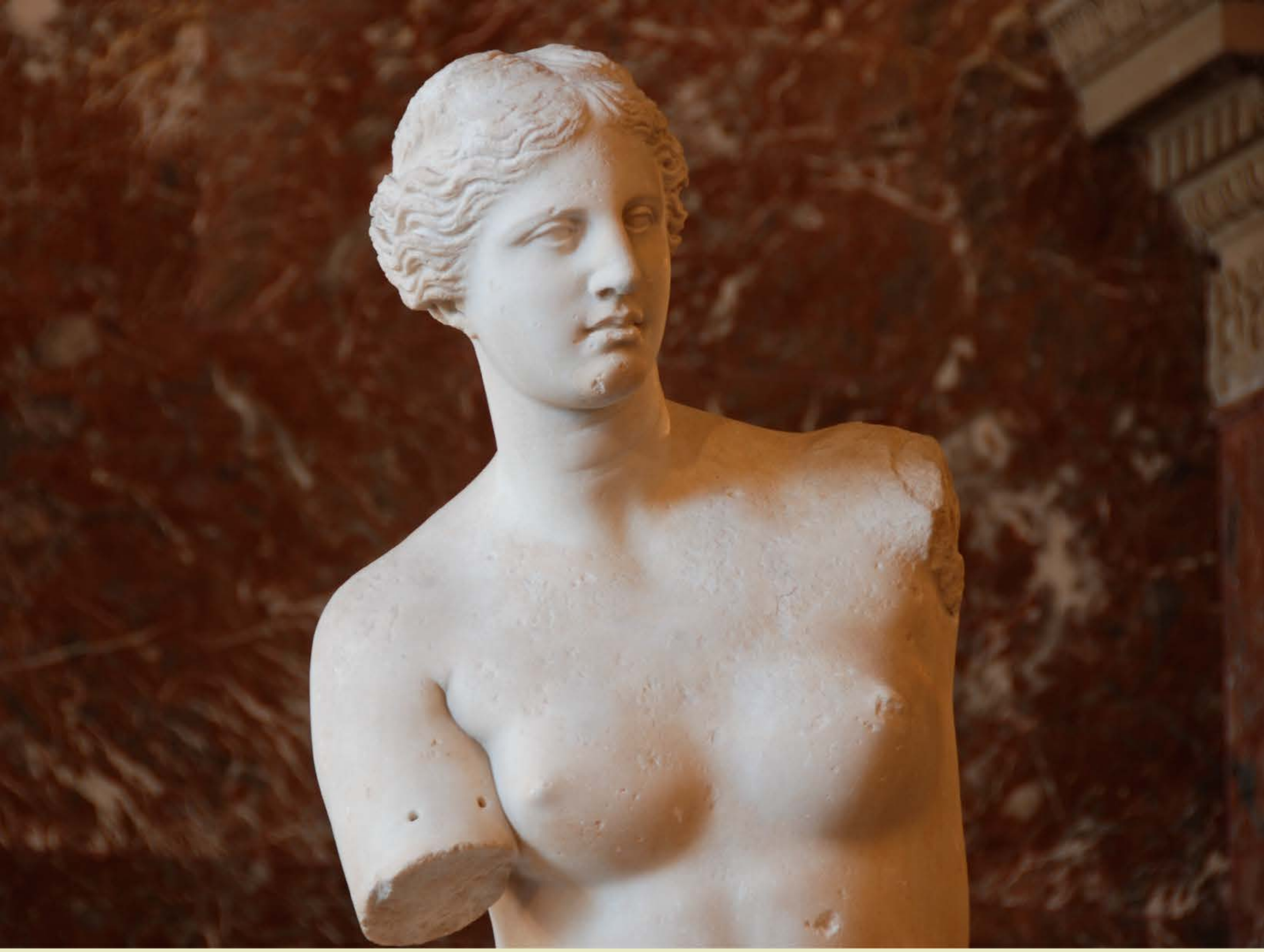

Maria João Nunes Rodrigues

Influence of Scatter Radiation on Dose Optimization and Image Quality in Digital Breast Tomosynthesis

Dissertação de Mestrado Integrado em Engenharia Biomédica,
apresentada ao Departamento de Física da Faculdade de Ciências e Tecnologia da Universidade de Coimbra.

Setembro 2016

· U C ·

UNIVERSIDADE DE COIMBRA

• U C •

FCTUC FACULDADE DE CIÊNCIAS
E TECNOLOGIA
UNIVERSIDADE DE COIMBRA

Maria João Nunes Rodrigues

Influence of Scatter Radiation on Dose Optimization and Image Quality in Digital Breast Tomosynthesis

Dissertation presented to the University of Coimbra
in order to complete the necessary requirements to
obtain the Master's degree in Biomedical Engineering.

Supervisors:

Ph.D. Salvatore di Maria (IST-C2TN)

Prof. Ph. D. Pedro Vaz (IST-C2TN)

Prof. Ph.D. Isabel Lopes (UC-DF)

Coimbra, 2016

This work was developed in collaboration with:

Centro de Ciências e Tecnologias Nucleares

Instituto Superior Técnico

Universidade de Lisboa

Bobadela, Portugal

Instituto Português de Oncologia de Lisboa Francisco Gentil

Lisboa, Portugal

À Maria e ao Eduardo,

a quem tudo devo.

Acknowledgments/Agradecimentos

Ao terminar esta dura etapa, o fim de uma caminhada de cinco anos chegou e para sempre irei guardar na memória tudo o que Coimbra me ensinou. Coimbra deu-me a conhecer pessoas fantásticas, viver momentos incríveis e outros não tão incríveis, mas acima de tudo, fez-me crescer e a ela estou imensamente grata. Agora que cruzo a linha da meta vejo em retrospectiva todos os que, de uma maneira ou de outra, contribuíram para que este momento se concretizasse.

Em primeiro lugar quero agradecer ao Salvatore di Maria por ter sido um excelente orientador ao longo de todas as fases deste trabalho, sem o seu supervisionamento e apoio, nada disto teria sido possível. Agradeço também ao prof. Doutor Pedro Vaz e à profª. Doutora Isabel Lopes pelo interesse em desenvolver este projecto e por terem confiado em mim para fazê-lo.

Em segundo lugar, agradeço ao Instituto Português de Oncologia Francisco Gentil de Lisboa, mais concretamente ao director do Departamento de Radioterapia e Imagem, o Dr. José Venâncio e ao físico hospitalar, o engenheiro José Afonso, que permitiram utilizar o equipamento de tomossíntese para as medições de dose e aquisição de imagens.

Quero também deixar um especial agradecimento à Tânia Marques por me ter esclarecido várias dúvidas sobre o código PenEasy e por me ter facultado todo o trabalho que desenvolveu sobre a tomossíntese mamária, que veio a ser essencial para iniciar este projecto.

Obrigado a todos os que me acompanharam e ajudaram durante este ano no CTN, especialmente à Ana Belchior e à Mariana Baptista por sempre terem mostrado disponibilidade para esclarecer uma dúvida, por muito descabida que possa ter sido (e ainda foram algumas), e principalmente pelas horas de almoço muito descontraídas que me proporcionaram. Aos meus colegas de sala: Débora, Jéssica e Daniel; obrigada por tudo, malta!

À Lígia, ao Rui e à Sara, que foram uma segunda família e que muito me ensinaram, um enorme obrigada. Vocês são pessoas incríveis e nunca haverá Coimbra sem a vossa presença. Agradeço muito à Inês, à Laura, à Clarissa e ao Zé por, ao longo de todos estes anos, terem o dom da palavra e motivarem-me de modo a enfrentar e vencer todos os meus gigantes Adamastores que foram surgindo pelo caminho.

Estarei para sempre grata à minha tia Fátima pois sem a sua ajuda não teria podido vir para Lisboa fazer este trabalho.

E os meus últimos e mais importantes agradecimentos vão para o meu irmão e para aos meus pais. Obrigado mano por sempre teres acreditado que era capaz, mesmo quando eu própria não acreditava. Pela tua força e resiliência és, para mim, uma figura inspiradora...

Não há palavras suficientes para descrever o sentimento de gratidão que tenho para contigo pai e para contigo mãe. Por todos os sacrifícios que vocês tiveram que fazer para que eu pudesse chegar ao dia de hoje, pelo amor incondicional, pela tremenda paciência que têm para me aturar e por nunca me terem cortado as asas quando quis correr atrás de um ideal, um enorme obrigado, amo-vos muito.

Abstract

Mammography is still considered the standard technique for breast screening, however, its main limitation is due to the superposition of tissues. Digital breast tomosynthesis (DBT), which employs a limited number of low-dose projections through a limited arc rotation around the breast, is being explored as an alternative modality. However, one of the main concerns is the amount of scatter that significantly worsens the image quality and consequently the lesion detectability. In DBT this is still more crucial, since an anti-scatter grid is not included.

In this work, the PENELOPE code as Monte Carlo (MC) method was used to model the scatter distribution allowing a deep understanding of its behavior in DBT geometries. After a successful validation of the MC model, an image quality optimization study for different compositions and breast thicknesses was performed using a figure-of-merit (FOM). The results showed that, the inclusion of scatter does not change the optimal energy value but only FOM's absolute value decreases. It was observed that, thicker breasts require higher energies but the deterioration of lesion detectability is also higher (about 80% of signal loss for 8 cm thick breast). For each breast composition and lesion types, 18 keV was found to be the optimal energy for most of the tasks analyzed.

In DBT, scatter showed a great dependence on projection angle (scatter-to-primary ratio increased 14% between projection angles of 0° and 24°). Glandular fraction and position of measurement was found to have a small effect. Using a W/Rh anode/filter combination, simulations showed that about 17% scatter reduction is achievable when passing from about 20 to 40 kVp. The contribution of multiscatter and secondary on total scatter was found to be higher than expected (of order of 30%). A subtraction-based method for scatter reduction on DBT projection images acquired from a Siemens Mammomat Inspirations system was proposed. An imaging analysis (signal difference to noise ratio) revealed that the detectability of tumor and calcification increased. The scatter correction is still more crucial in DBT than in standard mammography and the method proposed has the potential to be used at clinical level. Finally, a dosimetric study was performed and for different PMMA thicknesses, the results showed that the mean glandular dose was always below the reference values defined by the European protocol.

Keywords: Digital Breast Tomosynthesis; Scattered Radiation; Monte Carlo simulations, Image Quality; Scatter Reduction Method

Resumo

A mamografia ainda é considerada a técnica padrão para o rastreio do cancro da mama, contudo, a sua maior limitação deve-se à sobreposição de tecidos. A tomossíntese digital mamária (TDM), que utiliza um número limitado de projecções de baixa dose através de uma rotação limitada em arco em torno da mama, está a ser explorada como uma modalidade alternativa. No entanto, uma das principais preocupações é a quantidade de radiação dispersa que piora significativamente a qualidade de imagem e, consequentemente, a detectabilidade da lesão. Em TDM, este problema é ainda mais importante uma vez que uma grelha de "anti-scatter" não é incluída.

Neste trabalho, usou-se o código PENELOPE, como método de Monte Carlo (MC), para modelar a distribuição da radiação dispersa permitindo uma profunda compreensão do seu comportamento em geometrias TDM. Após uma validação bem-sucedida do modelo MC, foi realizado um estudo de optimização da qualidade de imagem para diferentes composições e espessuras de mama utilizando uma figura-de-mérito (FdM). Os resultados mostraram que, a inclusão de radiação dispersa não faz alterar o valor de energia óptima, apenas diminui o valor absoluto da FdM. Observou-se que, mamas densas requerem energias mais elevadas, mas a deterioração da detectabilidade da lesão é também mais elevada (perda do sinal cerca de 80% para uma mama com 8 cm de espessura). Para cada composição de mama e tipo de lesões, 18 keV foi a energia óptima para a maioria das tarefas.

Em TDM, a radiação dispersa mostrou ser muito dependente do ângulo de projecção ("scatter-to-primary ratio" aumentou 14% entre projecções de 0° e 24°). A fracção glandular e a posição de medição mostraram ter um pequeno efeito. Utilizando uma combinação ânodo/filtro o W/Rh, as simulações mostraram que houve uma redução de cerca de 18% da radiação dispersa quando se passa de 20 kVp para 40 kV. A contribuição dos fotões secundários e dos que sofreram múltiplas interacções com a matéria na radiação dispersa total foi mais elevada do que o esperado (na ordem dos 30%). Foi proposto um método baseado em subtração para a redução da dispersão em imagens de projeção TDM adquiridos a partir de um sistema Siemens Mammomat Inspiration. A análise da imagem (relação sinal-ruído) demonstrou que a detectabilidade do tumor e da calcificação aumentou. A correcção da radiação dispersa é muito mais crucial em TDM do que na mamografia convencional e o método proposto neste trabalho tem potencial para ser utilizado a nível

clínico. Finalmente, realizou-se um estudo dosimétrico e para as diferentes espessuras de PMMA, os resultados mostraram que a dose média glandular foi sempre menor do que os valores de referência definidos pelo protocolo Europeu.

Palavras-chave: Tomossíntese mamária digital; Radiação dispersa; Simulações de Monte Carlo, Qualidade da imagem; Método para reduzir a radiação dispersa

Contents

List of Figures

List of Tables

Acronyms

AEC	Automatic exposure control
AG	Air gap
ALARA	As Low As Reasonable Achievable
BC	Breast cancer
BI-RADS	Breast Imaging Reporting and Data System
BSF	Backscatter factor
CC	Cranio-caudal
CT	Computed tomography
DBT	Digital Breast Tomosynthesis
DM	Digital mammography
ESD	Entrance surface dose
FBP	Filtered backprojection
FDA	Food and Drug Administration
FFDM	Full-field digital mammography
FOM	Figure-of-merit
HVL	Half-value layer
IC	Ionization chamber
IDC	Invasive ductal carcinoma

IPOLFG Instituto Português de Oncologia de Lisboa Francisco Gentil

MC Monte Carlo

MGD Mean glandular dose

MLEM Maximum likelihood expectation maximization

MLO Mediolateral oblique

MR Mortality rate

MRI Magnetic resonance imaging

PENELOPE PENetration and Energy Loss of Positrons and Electrons

PHS Pulse height spectrum

PMMA Polymethylmethacrylate

PSF Point spread function

ROI Region-of-interest

SDNR Signal difference-to-noise ratio

SF Scatter fraction

SFM Screen-film mammography

SID Source-to-image distance

SL Signal loss

SPR Scatter-to-primary ratio

US Ultrasound

WCRF World Cancer Research Fund

WHO World Health Organization

Chapter 1

Introduction

1.1 Motivation and Goals

Cancer is a major health problem in Portugal and in many parts of the world. Besides death by heart disease, in 2014 cancer was the main cause of mortality in Portugal concerning 25% of all deaths [1].

Breast cancer has a large influence in Portuguese society, more specifically in women, since around 6000 new cases are discovered each year and among them, 1500 cases take to death [2,3]. Even though BC is more frequent and deadly in women it is important to mention that about 1% of all cases diagnosed are in men [2,4].

BC is the most common cancer worldwide in women with 1.7 million new cases diagnosed in 2012 according to the World Cancer Research Fund (WCRF) [5]. Reports developed by the WCRF [5,6] and the World Health Organization (WHO) [7,8] revealed that the incidence rates of BC over the years tend to increase and it could be explained due to the urbanization and industrialization but also due to the screening techniques for earlier detection.

Another interesting detail in those reports shows that the BC is more common in countries with a high-income profile, for instance: Northern America, Western Europe, and Northern Europe. In those regions, also named as the developed countries, the incidence rates are nearly three times higher than countries with medium- and low-income profiles like for example: Middle Africa, Eastern Asia, and South-Central Asia, see Figure 1.1. On the other hand, the Mortality rate (MR) tend to decrease as the time passes and the reasons are related to a better quality of BC treatment and to appropriate healthcare

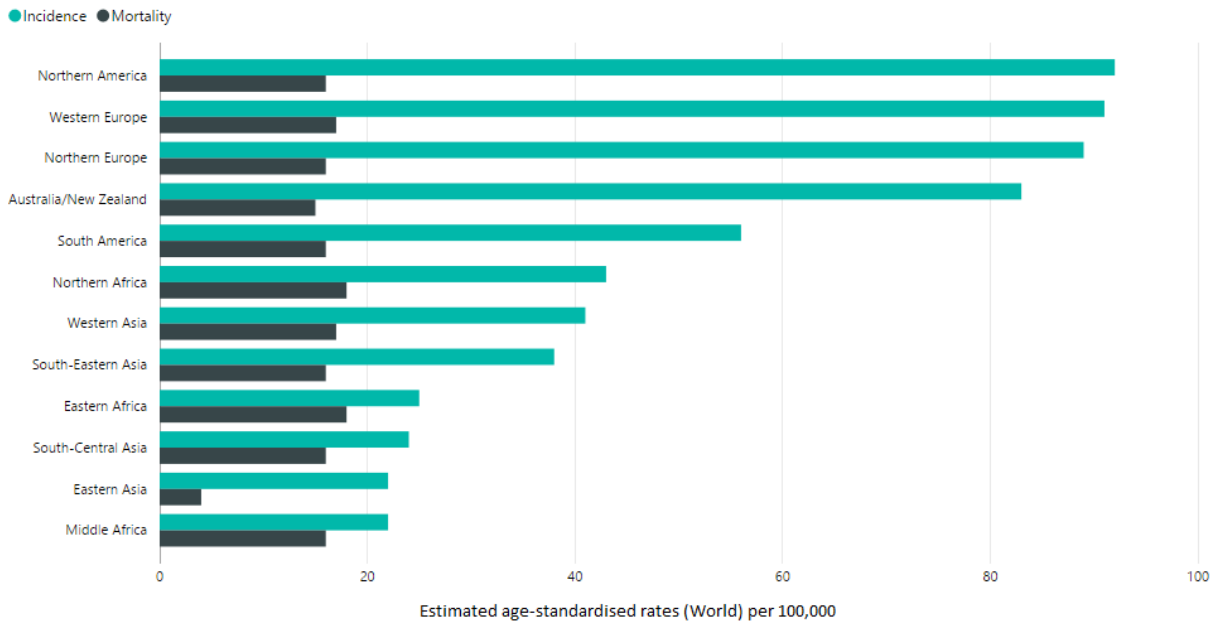

Figure 1.1: Incidence and mortality of BC worldwide [8].

plans which promotes earlier detection [6, 7, 9].

In face of these numbers and statistics, many solutions have appeared along the decades to properly detect, at an earlier stage, breast malignant lesions. The development of better breast screening techniques has been active since 1930 and in 1960 the first images from xeromammography were obtained [9, 10]. This technique [11] is an adaptation of the xerographic photocopying process and it surpassed the direct-film exposure mammography. However, the longer exposure, high radiation dose and difficulties on processing the image led to the discontinuation of this method and to its replacement by Screen-film mammography (SFM).

In the 70's decade SFM [11] was introduced in clinical practice, making the breast imaging technique faster and with lower radiation dose associated. In addition, the images showed better contrast allowing the differentiation of tissues in the breast. At the same time the concept of the uniform-thickness compression was implemented.

Later on, SFM became more common for breast screening and by the 90's it was necessary to create a system of regulations for image quality and dose delivered to the patient [9–11] for radiologists working in this X-ray diagnostic area. An example is the Breast Imaging Reporting and Data System (BI-RADS), developed by the American College of Radiology [12]. This system provides a standard method to describe mammogram findings and results, sorting them into categories numbered 0 to 6 [12–14]. Therefore, these

standardized protocols started to provide a universal language to technicians, physicists, and radiologists in order to communicate their findings and recommendations.

At the turn of the century, the Food and Drug Administration (FDA) approved the first Digital mammography (DM), the Senographe 2000D [10]. The Full-field digital mammography (FFDM) changed the way with which images are acquired since it involves a detector capable of detecting with effectiveness the incident X-ray instead of a film. Studies were performed to evaluate and compare the ability of diagnosis on both techniques [15–17] and results concluded that FFDM has an equivalent or slightly higher capability of detecting lesions and has better image quality with a superior image contrast.

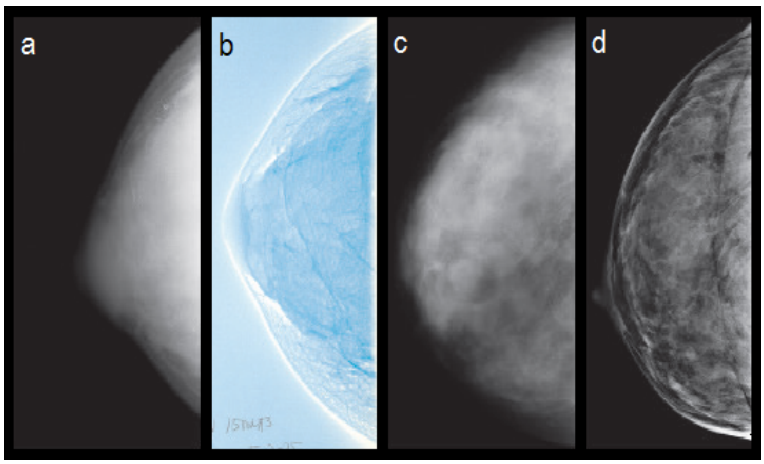

Figure 1.2: Breast images obtained from different breast imaging techniques [11]. a) Mammogram obtained from direct-exposure film. In this technique the patient receives a higher dose and the image quality is very poor. b) This image come from xeromammography and its color is blue because it is printed on paper with blue powder allowing no need for a light box. c) Image resulted from screen-film mamography and d) digital mammography.

Nowadays DM is the standard procedure for breast imaging and its use has been controversially discussed among the scientific community about its potential of decreasing the MR of BC.

As aforementioned, the MR is decreasing over the years and some authors declare that mammography as breast screening is one of the reasons for it, pointing to a 20-30% reduction [18,19]. For instance, Gelder et al. created a predictive model [20] based on data from a 2-year follow-up of FFDM data and they concluded that the MR would decrease 4.4% but with an overdiagnosis rate of 21%. An overview of the Swedish randomized trials performed by Nyström et al. stated that for women aged 50-69 the MR reduction was equal to 29% but it was not significant for younger female (aged 40-49) [21]. In this

latter observation, a randomized screening trial performed in Canada [22] also concluded that an annual breast screening among women aged 40-59 does not have in impact on MR of BC. However, there are some authors like Gotzsche and Olsen [23] which declared, after a 12-year follow-up, that screening programs do not show any significant evidence in reducing the MR and that maybe a breast screening with mammography seems to be unjustifiable.

Despite the divergent results on the matter, the screening technique is still considered one of the most powerful methods able to prevent from death cancer, and for this reason further efforts should be done in order to improve these diagnostic tools.

Considering breast imaging, it is important to point out that mammography has one major limitation which is the tissue superposition. Mammogram is a 2D projection of a tri-dimensional structure and so the overlapping effect leads to two main problems which are: the low sensitivity (difficulty to detect lesions) and low specificity (non-negligible percentage of false positives). According to the work of Elmore et al. [24], one-third of the women who undergo mammography will have a false positive result over 10 years of biannual screening. Obtaining a false-positive may cause negative reactions in women such as anxiety, stress, fear of having BC and also the increasing of monetary costs [25,26].

For the past few years new and improved techniques have been studied with the main goal of overcoming limitations in mammography. Digital Breast Tomosynthesis (DBT) and breast Computed tomography (CT) are two of these examples [27]. So far only the DBT is a clinical technology while breast CT is under investigation and its use is still limited to prototype systems.

DBT was first introduced by Niklason et al. [28] in 1997 and they proposed a new way of image acquisition using the same detector that FFDM uses. The innovative idea was to rotate the X-ray tube in one plane around the compressed breast in a limit angular range while the detector remains stationary. In the end of a series of acquisitions the projection images go through a post-processing algorithm that returns a reconstructed image. This quasi-3D-reconstructed [29] image is composed of several slices and it has anisotropic spatial resolution which means higher spatial resolution through parallel planes to the detector and lower resolution in the perpendicular direction. Despite of the loss of resolution at this direction, it is still good enough to differentiate the localization of lesions, making it possible to overcome the limitation of mammography.

Although DBT is now in clinical practice it remains under investigation for optimization studies in terms of choosing the most suitable parameters that maximizes the image quality but keeping the radiation exposure within the limits of breast dosimetry. Acquisition time [30, 31], number of projections and angular range [31], total radiation dose [32–35], breast thickness, glandular composition of the breast [32, 36] and tomosynthesis reconstruction algorithm [37, 38] are some of the issues taken into consideration when performing DBT optimization studies.

Scattered radiation is also an issue that must be taken into account because the DBT equipment does not operate with an anti-scatter grid like in standard mammography. The anti-scatter grid has the function of absorbing the radiation that reaches the grid from non-perpendicular angles to the aperture of the septa so it seems logical that this method cannot be applied to a DBT system since the non-zero angle projections would promote a large absorption of primary x-rays by the grid [29]. In a matter of fact, in mammography the anti-scatter grid is a good solution to reduce scatter and to improve the image contrast, but at the expense of increased dose to the patient [39]. In DBT, the available radiation per projection is already low, so the use of an anti scatter-grid will decrease the exposure even more.

There are two possible solutions in order to reduce the scatter in DBT. The first one is to develop a new design of anti-scatter grids where the septa's aperture could align parallel to the incident angle projection. However, the aforementioned inconvenient about the use of a grid in DBT could stop the search for such new designs of grids. The second solution relies on post-acquisition software-based scatter reduction on images [40–42] and nowadays the scientific community has invested a lot in this field. Therefore it is of extreme importance to have knowledge about its magnitude and spatial distribution, sources that contribute to scattering and its influence on image quality in DBT.

The presence of scatter on DBT images is related to the degradation of contrast and a loss in accuracy of attenuation values inferred from the reconstructed images. In the work published by Wu et al. [43] the degree of degradation on image quality by scatter was measured through quantitative methods. The results shows a reduction of 30%, 28% and 60% in contrast on the reconstructed central slice image, inferred attenuation coefficient (voxel value) and signal difference-to-noise ratio (SDNR), respectively.

Several authors have been studying the effects of scatter on DBT images and they

reported the sources that contribute to its appearance. The calculation of Scatter-to-primary ratio (SPR) from Monte Carlo (MC) simulations allows a comprehensive knowledge about the magnitude of scatter that strikes the detector [44–46]. Thereby the SPR is a function of the incident angle projection and compressed breast thickness. The SPR is also a function of the effect of glandular composition and breast size but in a minor scale. It turns out that X-ray spectrum does not have a considerable influence on SPR [47, 48]. In DBT a loss of spatial distribution was observed.

Surprisingly, Sechopoulos et al. [48] discovered that the compression paddle and cover plate have a significant impact on the SPR near the edges of the breast, and its contribution increases with the increasing of breast thickness. Also, Diaz et al. [49] showed that the total scattered radiation increases more than 30% when those mammographic components are included.

DBT is a recent technique with a prosperous future as a complementary tool to mammography or even to become a number one option for breast screening. Nowadays, DBT is still under optimization studies in order to find the best parameters which maximize the image quality. However, one significant problem that DBT must overcome is the inclusion of scattered radiation in the projection images. Scatter, as mentioned above, degrades the image contrast and promotes the loss of accuracy.

Taking all of this into consideration, the aim of this work is to minimize the influence of scatter on image quality of a DBT system by applying a method of scatter reduction into projection images. But first, a well characterization of X-ray scatter in terms of its magnitude is fundamental.

1.2 Thesis Outline

This dissertation is divided in seven chapters. **Chapter 1** presents the numbers and statistics of BC around the world and in Portugal. However, a brief discussion about the evolution of mammography from the sixties until nowadays is reported. Finally, in this chapter, the motivation and thesis organization are described.

In **Chapter 2**, information related to the breast like its anatomy and how the cancer develops in this organ is explained. The differences, vantages, and disadvantages between mammography and DBT, which are the two main techniques related to this work, are

presented in here.

The explanation of all the physical interactions involved in X-ray mammography and how the process of scattered radiation occurs is described in **Chapter 3**. Also, in this chapter, the fundamentals of dosimetry and breast dosimetry are introduced.

In **Chapter 4** all the information about scatter in mammography, its effect on image quality and the parameters used to quantify it is showed. Given the importance of scatter on images, a list of all the mammographic features that contributes to its presence is reported.

Chapter 5 includes the materials used and methods applied in this work. The MC simulations are briefly summarized and the PENELOPE code is explained. The characteristics of the DBT equipment, the phantoms and the geometries created for MC simulations are described in this chapter as well. The results and discussion are included in **Chapter 6**. Finally, in **Chapter 7**, the general conclusions are summarized and future work is discussed.

Chapter 2

Breast imaging

In this chapter is described the anatomy of the breast and is explained the development of cancer within the breast tissues. An overview of the breast imaging techniques using X-ray radiation is also presented.

2.1 Breast anatomy

The breast consists of (see Figure 2.1) [50] adipose tissue, lobules (glandular tissue which produces milk), ducts (tubes that carry milk from the lobules to the nipple) and stroma (ligaments, fibrous connective tissue, nerves, lymph vessels and nodes, and blood vessels). The fibrous connective tissue and glandular tissue are commonly designated as fibroglandular tissue due to theirs similar radiographic properties. The composition of breast tissue varies with age [51]. The breast of younger women is composed mainly of fibroglandular tissue and, over time, occurs its replacement by fatty tissue.

2.2 Breast cancer (BC)

BC is a malignant tumor that begins in breast tissue, specifically in the glandular tissue. When it is discovered, the definition of whether it is or not a non-invasive (in situ) or invasive (or infiltrating) BC is crucial to an appropriate treatment. According to the origin of the tumor, there are two kinds of BC in situ: the ductal carcinoma in situ (the tumor grows inside the ducts) or the lobular carcinoma in situ (the tumor is confined in the lobules). With increasing of tumor size, the ducts or lobules walls could break and

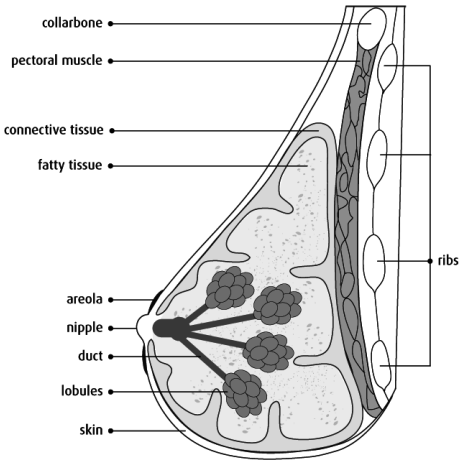

Figure 2.1: Breast anatomy [50].

the BC invades the surrounding healthy tissue of the breast, so they are called invasive or infiltrating BC. There also two types: the invasive ductal carcinoma (IDC) (the tumor starts inside the ducts) or invasive lobular carcinoma (if its origin is in the lobules). Its level of aggressiveness is too high and it could lead to spread (or metastasize) the tumor to other parts of the body. The American Cancer Society revealed that most of the BC detected is invasive or infiltrating [52].

2.3 Breast imaging techniques

Besides mammography, there are others techniques used to narrow the evidence and obtain an accurate diagnostic. The breast ultrasound (US) and breast magnetic resonance imaging (MRI) are two examples of complementary modalities and, in both, it is not used radiation.

In Portugal [53], breast US is the first option to screen younger women and it is a common complementary tool, especially, for women with denser breasts. Breast US has demonstrated the capability to detect small malignant lesions that were occulted in mammography [54, 55]. Breast MRI is used for screening women who are at increased risk of BC and it is recommended for pre-therapeutic evaluation for this segment of the population [53, 56]. Further details about those techniques are out of the scope of this work.

Either conventional mammography or DBT are radiographic techniques and the con-

trast of their images are formed based on the difference of the linear X-ray attenuation coefficients (explained in detail in Chapter 3) of different types of breast tissue. Fibroglandular tissue is more radiographically opaque than fat and thus it appears light on mammograms while fat appears dark [51, 57]. According to Johns and Yaffe work [57] (see Figure 2.2), the fibroglandular tissue has similar radiographic properties to BC tissue, namely the IDC. This observation explains the difficulty of identifying a lesion on dense breasts which have a higher composition of fibroglandular tissue than fat.

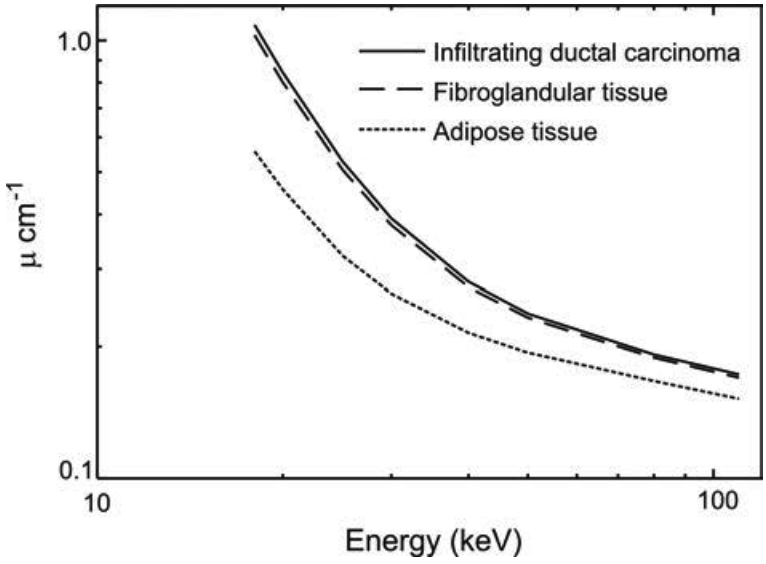

Figure 2.2: Relation between the energy and X-ray linear attenuation coefficients of adipose tissue, fibroglandular tissue and IDC [57].

2.3.1 Mammography

Mammography is a radiographic modality optimized for breast examination and is the gold standard technique for breast screening. In Portugal, mammography is used for the screening of asymptomatic women aged 50-69 every two years (or every 3 years for women with age superior to 69 years old) and for the investigation of symptomatic patients (diagnostic mammography) [58]. During a screening exam, two common views are acquired for each breast, the cranial-caudal (CC) and mediolateral oblique (MLO) view.

In a mammography unit is common to include: an anode that operates at low peak voltage (24-31kVp) with the addition of a filter for spectral shaping and a beam defining aperture [59]. In general, the mammography operates with a molybdenum anode with

molybdenum filter, however, other combinations of anode/filter can be used, for example: molybdenum/rhodium, rhodium/rhodium and tungsten/rhodium [59].

In the mammography geometry system, a perpendicular line from the focal spot of the X-ray source passes through the chest-wall and intersects with the edge (x's plane) of the image receptor [59]. In order to reduce the scattered radiation and maximize the image quality, an anti-scatter grid is placed between the breast support and the detector. To reduce dose and scatter, a flat panel (compression paddle) that compresses the breast into the breast support is used. Modern mammography units also include an automatic exposure control (AEC), which is a sensor that controls automatically the tube voltage or the target/filter/tube combination by estimating the compressed breast thickness and the transmitted exposure rate [59].

There are two types of mammography techniques: screen-film mammography (SFM) and digital mammography (DM). In SFM, a high spatial resolution fluorescent intensifying screen is used to absorb the transmitted radiation by the breast and convert them into an image [60]. The film has three different functions: it is an image acquisition detector, storage, and a display device. This is also its main disadvantage because, once the image is created, the manipulation of the film, like brightness or magnification, is extremely difficult [60]. Although SFM was, for many decades, the gold standard technique for breast screening, studies demonstrated that it is less sensitive in younger women (less than 50 years old) than for older female and the reason relies upon the differences in breast densities [61, 62].

DM [63] appeared in clinical practice in the beginning of the 21^{th} century with the aim to solve the limitation of the SFM. Instead of a film-screen, the DM detector is digital and the image acquisition, image processing and image display are performed independently allowing for individual optimization of each of these parts. Several studies [15–17] revealed that DM has a faster image acquisition, superior image quality, better contrast and fewer artifacts than compared to SFM but they were similar in terms of detecting lesions. Nowadays, SFM has almost entirely replaced by DM, around the world, as breast screening tool.

Despite the improving of mammography as an imaging modality of the breast, its main limitation has not be solved yet. In other words, the accuracy of mammography is still limited by anatomical noise resulted from the overlapping of normal structures within the

breast. The superposition of tissues can hide lesion detection, making them not visible on mammograms. Specifically it has been shown that this effect is more pronounced in denser breasts [22, 51]. In addition, the overlapping tissue effect is also a cause that contributes for the significant false-positive findings in mammograms [24].

2.3.2 Digital breast tomosynthesis (DBT)

DBT for eventual clinical use was described in 1997 by Niklason et al. [28] but the original concept of tomosynthesis was first introduced by Grant [64], 25 years before, in 1972. The development of DBT was in suspension for many years due to the lack of suitable X-ray imaging detectors. However, in the past decade, the advances in the digital flat-panel detectors increased the interest on DBT [65] as a possible alternative to mammography.

Nowadays, DBT has been used in adjunction with conventional mammography. In the past few years, many studies have proven the important role of DBT for breast screening. When it is used mammography plus DBT, besides the use of mammography alone, a reduction of false positives, fewer recalls and increase of cancer detection were observed [66, 67]. Furthermore, comparison studies revealed that DBT has a superior diagnostic accuracy for the visualization of lesions than SFM and DM [66–70] which may imply that DBT have a higher sensitivity for BC detection [66, 70].

The DBT device is usually based on an existing FFDM system. Mammography units capable to performing a DBT exam have been developed over the past few years. In 2011, the Food and Drug and Administration (FDA) approved the Hologic Selenia Dimensions to be used in clinical practice in the United States. In Europe, several other DBT equipments are being used such as the Siemens Mammomat Inspiration [65]. This last system is also in operation at the Instituto Português de Oncologia de Lisboa Francisco Gentil (IPOFGL) and it was used for the experimental part of this work. Depending on manufacturers, some technical specifications of the DBT equipment (prototype and commercial system) can be slightly different (see Table 2.1).

DBT technique consists on the acquisition of, typically, 9-25 [29], low-dose X-ray projections over the breast from a narrow angular range. This angular range could vary to 15-50° [29]. The X-ray source describes an arc movement around the compressed breast and the detector could rotate in the opposite direction of the source or remains

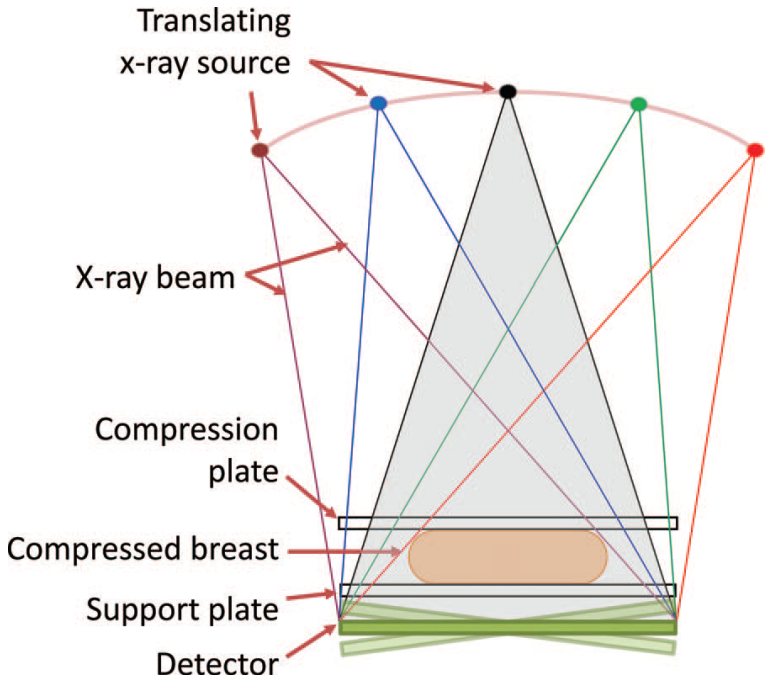

Figure 2.3: Schematic of a DBT acquisition system. A limited number of low X-ray projections are acquired while the X-ray source rotates around the compressed breast describing an arc. Depending of the DBT system, the detector can rotate at the same time as the X-ray source (but in the opposite direction) or remains static during the acquisition time. Image taken from the article "A review of breast tomosynthesis. Part I. The image acquisition process", I. Sechopoulos (2013) [29].

stationary (see Figure 2.3). The images resulted from the low-dose X-ray projections are then submitted to a reconstructed algorithm that creates a tomographic cross-sectional image or "slices" of the breast volume. These slices are very thin, typically of the order of 1 mm thick [29, 71].

Depending on the DBT system, the source can perform two types of motion: continuous (the tube moves continuously while pulsing short exposures during the scan) or "step-and-shoot" motion (one exposure at each position of the tube between movements). In theory, the step-and-shoot motion reduces the blur effect on images but in reality, the exam takes longer which results in more image artifacts due to patient motion [71].

Due to the limited angle of scanning, the DBT images are only "quasi-3-dimensional" and they are characterized by its anisotropic spatial resolution, which means high spatial resolution in the parallel planes (x-y plane) of the detector and lower resolution in planes parallel to the z-axis (perpendicular planes to the detector). This low spatial resolution in depth remains good enough to reduce the issue of tissue overlapping, however, it is known that a wide angle allows better depth resolution while narrowing it enhances the

Table 2.1: Technical specifications of the two DBT systems approved for clinical pratice [29]. The Siemens Mammomat Inspiration was used in the experimental part of this work.

DBT system	Hologic Selenia Dimensions	Siemens Mammomat Inspiration
Type of detector	Full-field-direct (Se)	Full-field-direct (Se)
Detector pixel size (μm)	70 (binned 2x2)	85
Target filter/combination	W/(0.7mm Al)	W/(0.05mm Rh)
Detector motion	Rotating	Static
X-ray tube motion	Continuous	Continuous
Angular range (deg)	15	50
Number of projections	15	25
Scan time (s)	3.7	25
Reconstruction method	Filtered backprojection	Filtered backprojection

in-plane resolution [29, 65, 71].

Apart the issue of superposition of tissues partially solved by DBT, another relevant topic is related to the possible breast compression reduction in this technique. As seen before, the compression is important in mammography because reduces the overlapping tissue effect but it is uncomfortable and painful for women undergoing to this type of examination. The available DBT systems apply a similar compression force as used for FFDM. Saunders et al. [72] and Förnvik et al. [73] have studied this issue and they concluded that the compression could be reduced without affecting lesion conspicuity or radiation dose. However, further investigation is still ongoing.

The reconstruction methods applied in DBT are well described in the review performed by Dobbins and Godfrey [74]. They categorize the reconstruction techniques in three different families: the Fourier techniques, algebraic methods and statistical methods. This last algorithm uses a statistical model such the maximum likelihood expectation maximization (MLEM) [37] which its main goal is to maximize the probability of producing the projection images to converge on a solution.

The filtered backprojection (FBP), an example of a Fourier technique, is the most common algorithm for tomosynthesis reconstruction and is especially used in CT. However, due to the limited angle, not all of the frequency space volume is sampled which leads to problems in accuracy in the final reconstruction images [37, 74].

The algebraic methods include: the algebraic reconstruction technique, the simultaneous iterative reconstruction technique and the simultaneous algebraic reconstruction

technique. In general, these methods set up a system of simultaneous linear equations linking each voxel element to project pixel values in a number of projection images [37,74]. Studies comparing several methods of reconstruction, like the work developed by Wu et al. [38] and Sidky et al. [75], revealed that either algebraic methods (SART) or the MLEM can provide higher image quality and fewer artifacts compared to FBP, but at the expense of longer computational time.

Another relevant topic to discuss the DBT is in terms of radiation exposure and dose absorbed by the patient. The total dose in DBT consists of the cumulative sum of the doses for the set projections. In dosimetric studies using Monte Carlo simulations [32,33] reported that a single tomosynthesis acquisition has a comparable dose to one or two-view FFDM mammographic images.

Chapter 3

Diagnostic radiology physics

Since the discovery of X-rays by Wilhelm Conrad Röentgen in 1895 and the inherent ability of X-rays to visualize the anatomical structures of a human body, the use of X-rays made a huge contribution to the evolution of medical imaging. Over time, the combination of knowledge from several areas (e.g. physics, medicine, and engineering), allowed the development of improved medical imaging systems. Nevertheless, the limits of dosimetry and principles of radioprotection must always be taken into account and respected.

In this chapter, an overview of the types of interaction of photons with matter, within the mammography energy range, is presented. In addition, the basic theoretical concepts of dosimetry and breast dosimetry are explained.

3.1 Interaction of photons with matter

Photons are considered indirectly ionizing radiation [76]. In medical imaging and treatment of diseases (radiotherapy), high-energy photons, such X-rays and γ-rays, are commonly used. When a photon passes through some medium, three different results may occur: the photon does not interact with the material; the interaction happens and the photon is totally absorbed by the medium or the photon interacts depositing some of its energy but its original trajectory is changed. The probability of occurring photon interactions with matter depends on the photon energy, density of the medium and its atomic number [76].

3.1.1 Cross section

As mentioned above, the interaction of photons with matter is estimated using probabilistic calculations, since this phenomenon occurs in a stochastic form. Cross section is the parameter used to express the probability of interaction for photon radiation. It is important to point out that not all the photons coming from the same beam will have the same interaction with the matter.

When considering the interactions of photons in an atomic scale, the cross section is generally defined as the atomic cross section and it represents the effective area for an interaction between an X-ray photon and an atom of a particular material [77]. The differential cross section expresses the number of particles scattered, dN, per unit time per unit solid angle, $d\Omega$, divided by the incident flux, Φ, and is given by:

$$\frac{d\sigma}{d\Omega} = \frac{dN}{\Phi} \tag{3.1}$$

Integrating the previous equation for all solid angles it is obtained the total cross section:

$$\sigma = \int \frac{d\sigma}{d\Omega} d\Omega \tag{3.2}$$

The cross section unit is the barn (1b=$10^{-24} cm^2$).

Considering a photon beam, Φ, to be incident on a surface of material of area A containing n targets of cross section σ, the variation of interactions, $\Delta\Phi$, between photons and targets are [77]:

$$\Delta\Phi = \Phi n \frac{\sigma}{A}. \tag{3.3}$$

There are four types of X-ray interactions (photoelectric effect, coherent scattering, incoherent scattering and pair and triplet production) and each has a specific cross section [77]. The pair and triple production are not discussed in this work because this interaction takes place at high-energy (MeV scale) while the X-ray mammography energy range is between about 18 and 40 keV.

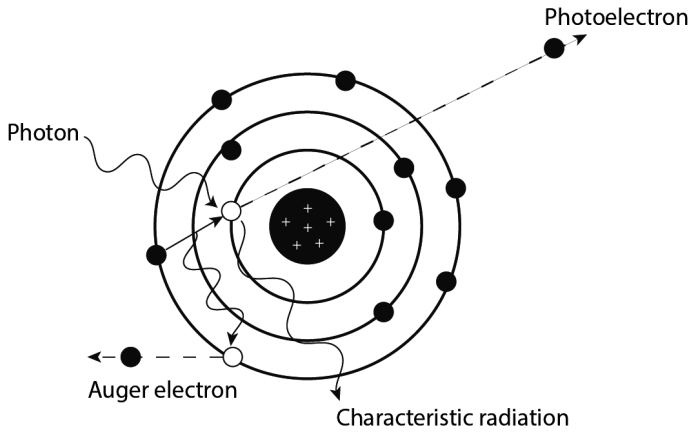

Figure 3.1: Scheme of the photoelectric effect. Figure adapted from [77].

3.1.2 Photoelectric effect

A photon is an elementary particle characterized for having no mass and its energy depends only on its frequency or its wavelength. Therefore, the energy of a photon can be expressed by the following formula:

$$E = h\nu = \frac{hc}{\lambda}, \tag{3.4}$$

where h is the Planck's constant, ν is the photon frequency, c is the speed of light and λ is the wavelength of the photon [76].

In the photoelectric effect, an incident photon with initial energy E_0 collides with an orbital electron bound to an atom of the absorber material and all its kinetic energy is transferred to the electron [77]. However, this process only occurs if the energy E_0 of the incident photon exceeds the binding energy of the electron. In this case, the electron, also called photoelectron, is ejected from its atomic shell with kinetic energy, as it is represented in Figure 3.1. When a photoelectron is ejected, for example, from the K-shell of the atom, its kinetic energy corresponds to the difference between the E_0 and the binding energy, BE_K, of the K-shell [76]. Characteristic photon (fluorescence) and Auger electron are produced by outer shell electrons when they are trying to reorganize in order to fill the vacancy left by the photoelectron.

Within the diagnostic energy range (below 150keV), the photoelectric effect cross section [59], τ, is a function of the incident photon energy E_0 and the atomic number Z of a given absorber element:

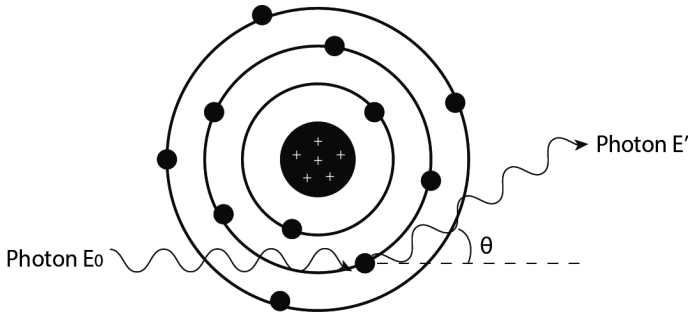

Figure 3.2: Diagram of the Rayleigh effect. The incident photon is scattered with angle θ and similar energy (E'=E_0). Figure adapted from [77].

$$\tau(h\nu, Z) = k\frac{Z^n}{(E_0)^m}, \tag{3.5}$$

where k is a constant, n and m represent exponents in the range 3.6-5.3 and 2.5-3.5, respectively. Considering the diagnostic energy range, a typical dependence of τ is showed in the following expression, where the values of n and m are equal to 4 and 3, respectively [59]. Therefore, the τ strongly depends on (directly proportional) the fourth power of the atom's number atomic and it is inversely proportional to the cube of the photon energy

$$\tau \sim \frac{Z^4}{E_0^3}. \tag{3.6}$$

3.1.3 Coherent (Rayleigh) effect

In the coherent effect, or Rayleigh effect, a photon hits an electron bound to the atom shell and is scattered with an angle θ as shown in Figure 3.3. A small fraction of the incident photon energy E_0 is lost, however, it is small enough to consider that the scattered photon leaves the atom with similar energy E' as E_0.

During the Rayleigh effect, the atom does not become excited or ionized and after the interaction, the orbital electrons return to their original state. For this reason, the scattering angles are relatively small [76]. The differential Rayleigh atomic cross section per unit solid angle,$\frac{d\sigma_{coh}}{d\Omega}$,is expressed in the following equation:

$$\frac{d\sigma_{coh}}{d\Omega} = \frac{r_0^2}{2}(1 + cos^2\theta)F^2(x, Z), \tag{3.7}$$

where r_0 is the classical electron radius (r_0=2.81794$\times 10^{-15}$m), θ is the angle of the scattered photon with respect to its initial trajectory, F(x, Z) is known as the coherent

form factor, x is a measure of the momentum transfer ($x = \frac{sin(\frac{\theta}{2})}{\lambda}$), λ is the wavelength of the incident photon and Z is the atomic number of the absorber element [59].

3.1.4 Incoherent (Compton) effect

To occur the Compton effect the energy of the incident photon must be higher than the binding energy of the electron that is in the outer shell of the atom. As a result of this interaction, a scattered photon with lower energy (i.e. it has bigger wavelength than the incident photon, $\lambda' > \lambda_0$, (see Equation 3.4) is produced and an electron (recoil electron) is ejected with kinetic energy and an angle φ, as shown in Figure 3.3. The atom enters in an ionized state. Furthermore, after this interaction, the trajectory of the photon changes its original direction and the θ angle is the angle between the previous photon trajectory and the new course of the scattered photon and its range is from 0° (forward scatter) to 180° (backscatter) [76].

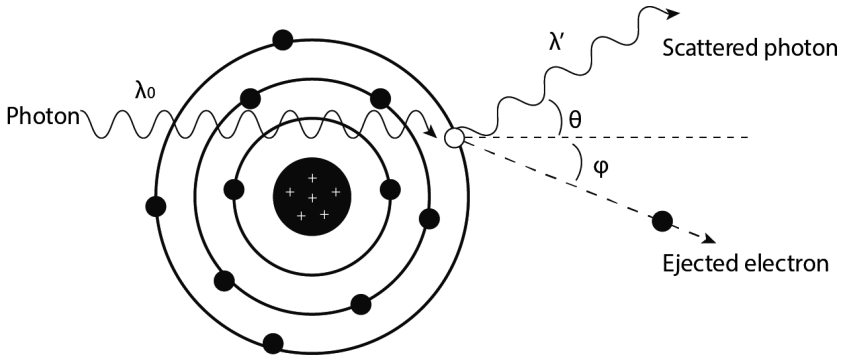

Figure 3.3: Diagram of the Compton effect. Figure adapted from [77].

The energy of the scattered photon is expressed using the laws of the conservation of energy and momentum [59]:

$$E' = \frac{E_0}{1 + \alpha(1 - cos\theta)}, \tag{3.8}$$

where $\alpha = \frac{E_0}{m_0 c^2}$ and its denominator corresponds to the rest-mass of the electron and it is a constant value equal to 511keV. Another important relation is the one between the θ and φ angle [59]:

$$cot\theta = (1 + \alpha)tan(\frac{\theta}{2}). \tag{3.9}$$

The energy of the recoil electron T_e results from the difference between the energy of incident photon and the energy of the scattered photon, ($T_e = E_0 - E'$).

The differential cross section for Compton scattering of photons by a single free electron at rest can be described using the formula firstly described by Klein-Nishina:

$$\frac{d\sigma_{KN}}{d\Omega} = \frac{r_0^2}{2}(1 + cos^2\theta) \times (\frac{1}{1 + \alpha(1 - cos\theta)})^2(1 + \frac{\alpha^2(1 - cos\theta)^2}{[1 + \alpha(1 - cos\theta)][1 + cos^2\theta]}), \quad (3.10)$$

where r_0 is the classical electron radius.

The Equation 3.10 is a theoretical calculation for the differential cross section and cannot expressed with accuracy what happens in reality, since, the electrons are neither free or at rest. Therefore, the contributions from individual electrons bounded to an atom have to be taking in account and, then, multiply this incoherent scattering function S(x,Z) to correct the previous equation:

$$\frac{d\sigma_{incoh}}{d\Omega} = \frac{d\sigma_{KN}}{d\Omega} \times S(x, Z). \quad (3.11)$$

Integrating the Equation 3.11, the cross section for Compton scattering σ_{incoh} is obtained. In most cases, the values of σ_{incoh} are very similar to those resulted from the multiplication of the cross section of single electron at rest by the number of electrons in the atom [59]:

$$\sigma_{incoh} \approx Z\sigma_{KN} \quad (3.12)$$

3.2 Photon attenuation coefficients

As it passes through the material, photons may undergo one or more interactions with the atoms of the medium and some are absorbed or scattered leading to their removal from the initial beam. The information about the passage of the photon beam through the bulk material is given by the linear and mass attenuation coefficients. Both the primary and the scattered photons are contained in the information provided by these coefficients.

3.2.1 Linear attenuation coefficient

Consider a collimated photon beam to be normally incident on a thin slab of a uniform material of thickness dx as shown in Figure 3.4. The probability of a photon interacts in that thin slab is:

$$N_a \sigma dx, \tag{3.13}$$

where N_a is the number of atoms per unit of volume and σ is the total cross section per atom. In addition, the product $N_a\sigma$ defines the linear attenuation coefficient (μ) and its unit is the inverse of length, generally in (cm^{-1}). The μ depends on the type of interaction, energy of the incident photon beam and physical state of the absorber material.

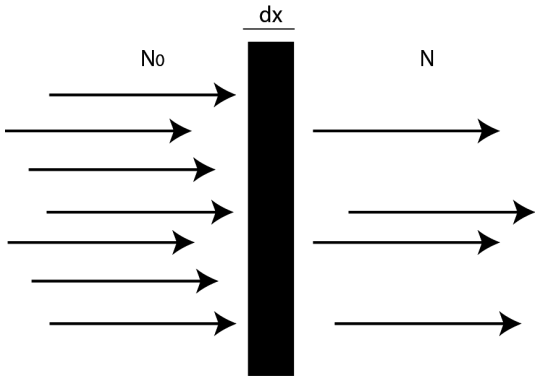

Figure 3.4: A collimated monoenergetic beam of photons passes through a thin slice of material of thickness dx. At the exit surface of the material a reduction in the number of photons is observed.

An initial number of photons, N_0, with the same monoenergetic energy, hit the entrance surface of the material. As it passes through the thin slab of material, the probability of the N_0 to interact along the material is given by $N_0\sigma dx$. Like it was said above, some photons are removed from the photon beam due to absorption or scattered processes, so the number of photons is lower at the exit surface of the material. As a result, a photon variation dN is observed and it is expressed by the following formula:

$$dN = -N_0 \mu dx. \tag{3.14}$$

The minus sign is used to show the reduction of the number of photons. Integrating the above equation leads to:

$$N = N_0 e^{-\mu x} \tag{3.15}$$

This equation is also known as the Beer-Lambert law and represents the exponential attenuation of a photon beam.

Although the use of monoenergetic radiation in medical imaging is the desirable goal, in practice it is very difficult to achieve a radiation beam with such characteristic, therefore, the Beer-Lambert law as is described in Equation 3.15 cannot be applied. As mentioned previously, the linear attenuation coefficient depends on the energy of the source beam, E, thus, for a polyenergetic beam the Beer-Lambert law is given by:

$$N(E) = \int_{E_{min}}^{E_{max}} N_0(E) e^{-\mu(E)x} dE \tag{3.16}$$

3.2.2 Mass attenuation coefficient

The division of the linear attenuation coefficient, μ, by the density of the absorber material, ρ, results in the mass attenuation coefficient, μ/ρ, and its dimensions are square meters per kilogram (m^2/kg). This quantity is independent of density and is suitable for data compilations. Although (m^2/kg) is the SI unit for mass attenuation coefficient, it is often used cm^2/g as unit.

When a material is composed by a compound or a mixture, the μ/ρ is calculated as the summation of the mass attenuation coefficients of the elements i (or mixture of components) and each of the elements or mixture of components are weighted using the normalized weight fraction w_i. The formula is given by the Equation 3.17.

$$(\frac{\mu}{\rho}) = \sum_i (\frac{\mu}{\rho})_i w_i \tag{3.17}$$

3.2.3 Total mass attenuation coefficient

The cross section of each of the interaction process described above is independent from each other and its occurrence only depends of its individual probability. As a result, the total mass attenuation coefficient is the sum of all the individual mass attenuation coefficients:

$$\frac{\mu}{\rho} = \frac{\mu_{photo}}{\rho} + \frac{\mu_{cohe}}{\rho} + \frac{\mu_{incoh}}{\rho} \tag{3.18}$$

The mass attenuation coefficient depends on two parameters: the photon energy and the atomic number of the absorber material.

3.3 Fundamentals of dosimetry

3.3.1 Quantities and units

There are several quantities and units used to quantify and characterize radiation fields, since, there are many different aspects of an X-ray beam that can be used to measure the amount of radiation. The use of a given quantity depends on the specific application considered. In the following sections, the common radiometric quantities are explained.

3.3.1.1 Fluence and energy fluence

The fluence, Φ, is the quotient between the number of particles, dN, incident upon a cross sectional area, dA, of a sphere and its unit is the inverse of the square meter (m^{-2}):

$$\Phi = \frac{dN}{dA} \tag{3.19}$$

The energy fluence, Ψ, defines the sum of energies of all incident particles (dR) upon a sphere with cross sectional, dA. The energy fluence unit is J/m^2.

$$\Psi = \frac{dR}{dA} \tag{3.20}$$

3.3.1.2 Kerma

Kerma (K) is an acronym for *kinetic energy released to matter* and it represents the sum of the initial kinetic energies of all charged particles released by the uncharged ionizing particles (such photons and neutrons), dE_{tr}, in a material of mass dm. The SI unit is gray (1Gy = 1J/kg).

$$K = \frac{dE_{tr}}{dm} \tag{3.21}$$

The kerma quantity is subdivided in two components: the collision kerma (K_{col}) and the radiative kerma (K_{rad}):

$$K = K_{col} + K_{rad} \tag{3.22}$$

where, the collision kerma translates the net energy transferred to charge particles per unit mass at the point of interest, excluding the radiative loss and energy transferred from one charged particle to another. The radiative kerma expresses the portion of the initial kinetic energy of the secondary charged particles that is converted into photon energy. In general the average fraction related to the radiative processes is represented by the bremstrahlung fraction, $\bar{g}$. As a result, the relation between the total kerma and the collision kerma can be expressed using the following equation:

$$K_{col} = K(1 - \bar{g}) \tag{3.23}$$

3.3.1.3 Absorbed dose

The absorbed dose (D) measures the absorbed energy, independently from the type of radiation (ionizing and non-ionizing radiation) and medium. The absorbed dose is related to the mean energy imparted, $\bar{\varepsilon}$.

The mean energy imparted is the sum of all energy entering the volume of the material, R_{in}, minus the sum of all energy that leaves that same volume, R_{out}, taking into consideration the sum of the mass-energy conversion,$\sum Q$. Within the energies for diagnostic radiology, the quantity $\sum Q$ is equal to zero. The SI unit for the mean energy imparted is Joule (J).

$$\bar{\varepsilon} = R_{in} - R_{out} + \sum Q. \tag{3.24}$$

Therefore, the absorbed dose is defined as the mean energy imparted to matter of mass, dm, in a certain volume of interest:

$$D = \frac{\bar{\varepsilon}}{dm}. \tag{3.25}$$

The unit for the absorbed dose is Gray (1Gy = 1J/kg).

3.3.1.4 Equivalent dose

The equivalent dose, H_T, of a given organ or tissue, is the sum of all absorbed doses,D_T, in that organ or tissue. Each type of radiation, R, has its own radiation weighting factor,W_R, that must be taken into account. As a result, the equivalent dose is given by:

$$H_T = \sum_R D_T W_R. \tag{3.26}$$

The SI unit for the equivalent dose is Sievert (1Sv = 1J/kg). For photons, the radiation weighting factor is equal to 1.

3.3.1.5 Effective dose

The effective dose, E, is the result of the product between the sum of all equivalent doses for each organ or tissue, H_T, and the tissue weighting factor for that organ or tissue, W_T:

$$E = \sum_R H_T W_T = \sum_T W_T \sum_R W_R D_{R,T}. \tag{3.27}$$

The SI unit for the effective dose is Sievert (1Sv = 1J/kg). The tissue weighting factors are independent from the type of radiation and energy. Table 3.1 shows the tissue weighting factors provided by the ICRP-103 for different organs or tissues [78].

Table 3.1: Tissue weighting factors for different organs or tissues. Table adapted from the ICRP-103 [78].

Tissue	Tissue weighting factor, W_T
Lung, stomach, colon, bone marrow, breast, remainder	0.12
Gonads	0.08
Thyroid, oesophagus, bladder, liver	0.04
Bone surface, skin, brain, salivary glands	0.01

3.3.1.6 Exposure

Exposure is the quantity that is used to measure the ability of a radiation field to ionize air. Roentgen (R) is the unit used to express exposure, however, the SI unit is

coulomb per kilogram on air (C/kg), where:

$$1R = 2.58 \times 10^{-4} C/kg \tag{3.28}$$

3.3.1.7 Relationship between Kerma and absorbed dose

In the previous sections, it was explained the definition of both kerma and absorbed dose and while kerma express the energy transferred due to interactions of uncharged particles, the absorbed dose takes into account all the energy deposited within the volume of interest [59].

For diagnostic photon beams, the electrons, resulting from photon interactions, have low energies, thus, they are absorbed almost in the same region where the interactions occurred and their radiative energy losses are negligible [79]. As a result, the values of absorbed dose and kerma are very similar [79] and its relationship is expressed in the following formula [59]:

$$D = \beta K_{col} = \beta K(1 - \bar{g}) \tag{3.29}$$

where β is a constant of proportionality between the quantities of absorbed dose, D, and collision kerma, K_{col}. For diagnostic radiology and low Z materials, it is assumed that the factor β is approximately equal to 1 [59].

3.4 Breast dosimetry

Mammography revealed to be capable in preventing BC, however, as it is a technique based on ionizing radiation, so, it has associated a small, yet significant, risk of radiation to induce a tumor [80]. The breast is a high radiosensitivity organ with a tissue weighting factor of 0.12 [78] for the estimation of the effective dose. Therefore, the technique that allows the detection of malignant lesions, also, promotes the development of tumors inside the breast.

Another aspect to consider is the relationship between dose and image quality. Improvements on the equipment and in the procedure are desirable in order to obtain better image quality with lower dose possible delivered to the patient. The estimation of breast dose is, then, fundamental for the quality control of mammography.

Nowadays, the mean glandular dose (explained in detail in the following sections) is the quantity recommended by the ICRP [81] to express the values of dose absorbed by the breast glandular tissue. This quantity is also used in several protocols like for instance the European Protocol [82].

3.4.1 Mean glandular dose

The concept of mean glandular dose (MGD) was introduced in 1976 by Karlsson et al. [83]. When exposed, the energy is deposited in all of the breast components: skin, adipose tissue and fibroglandular tissue. At the time, Karlsson and colleagues believed that is the glandular tissue which has the highest risk-induced carcinogenesis and nowadays it is a fact supported by the ICRP [81] and European Protocol [82].

MGD expresses the average deposited energy in the glandular tissue of the breast, however, it is very difficult or even impossible to directly measure the MGD on individual breasts. Nevertheless, there are two alternative methods to assess indirectly the MGD: by direct surface measurements on the patient or by measurements using a breast phantom [80]. The type of information obtained from those procedures is different. In the first, it is obtained information about the radiographic technique and how the dose varies with size and composition of the breast in a specific target of population (e.g. symptomatic patients or screened population). In the second method, the use of phantoms allows inter-system comparisons and it is appropriate for quality control [80].

In this work, the MGD was determined using a polymethylmethacrylate (PMMA) phantom.

3.4.1.1 Mammography

The European Guidelines for quality assurance [82] adopted the same dosimetric formalism as the one developed by Dance et al. in their extensive work [84, 85]. Therefore, the MGD for digital mammography (DM) can be measured using the following formula:

$$MGD_{DM} = K \times g \times c \times s, \tag{3.30}$$

where, K is the incident air kerma at the upper surface of the breast or phantom, measured free in air without backscatter. The conversion factors g, c and s were calculated

using Monte Carlo techniques. The g factor gives the MGD value for a breast of 50% of glandularity. The factor c allows for breast of different glandularity and the s factor allows for the use of different x-ray spectra. The conversion factors are tabulated as a function of breast thickness and PMMA thickness and are provided in the Appendix A: Tables A.1–A.3.

In addition, the European Guidelines for quality assurance [82] set maximum values for the mean glandular dose per PMMA thickness. These values are shown in Table 3.2.

Table 3.2: Reference values for MGD at different thicknesses of PMMA for mammography [82].

Thickness of PMMA (mm)	Equivalent breast thickness (mm)	Average glandular dose to equivalent breast	
		Acceptable level (mGy)	Achievable level (mGy)
20	21	1.0	0.6
30	32	1.5	1.0
40	45	2.0	1.6
45	53	2.5	2.0
50	60	3.0	2.4
60	75	4.5	3.6
70	90	6.5	5.1

3.4.1.2 DBT

In 2011 [86], Dance et al. proposed a formalism for the estimation of MGD for breast tomosynthesis. In 2015, a protocol for the quality control of DBT was released by the European Guidelines [87] in their fourth edition, in which they use the Dance et al. [86] formalism for breast dosimetry in DBT.

In fact, this formalism is an extension of the existing standard protocols, explained in the previous section, but with the introduction of a new conversion factor, the t-factor. As a result, the dose absorbed by the breast for a given angle of projection (θ) is given by the Equation 3.31.

$$MGD_{DBT}(\theta) = K \times g \times c \times s \times t(\theta), \tag{3.31}$$

where, t(θ) is the tomo factor for projection angle θ, K is the incident air kerma measured in the 0° and the rest of the conversion factors have the same definition as

described above. The factor t(θ) can be calculated using:

$$t(\theta) = \frac{MGD_{DBT}(\theta)}{MGD_{DBT}(0)}, \tag{3.32}$$

where, $MGD_{DBT}(0)$ is the absorbed dose for an angle of 0° and is an equal dose as the one obtained from a mammography exam using the same X-ray spectra and tube loading (mAs) [86]. It is clear that for the 0° projection, the t-factor is equal to 1. For a complete tomosynthesis exam the breast dose can be expressed by:

$$MGD_{DBT} = K_T \times g \times c \times s \times T \tag{3.33}$$

with

$$T = \sum_i \alpha_i t(\theta_i), \tag{3.34}$$

where the K_T is the incident air kerma at 0° but for the total tube loading for the complete exam. T is the T-factor for the complete exam and is the summation over all of the projections and α_i refers to the partition of the total tube loading for the different projections. If each projection has the same fraction of tube loading, the T-factor is then expressed using:

$$T = \frac{1}{N} \sum_i t(\theta_i), \tag{3.35}$$

where N is the number of projections. In Appendix A: Table A.4 is provided the T-factors for different scan ranges as function of different thicknesses of PMMA.

Until the present moment, there are no limiting values for dose concerning DBT, however, the European Guidelines [87] advise the use of the limiting values referenced for mammography examination, see Table 3.2.

It is important to point out that the breast dosimetry formalism described in here only applies for a DBT system with full-field geometry. The Siemens Mammomat Inspiration, DBT system used in this dissertation, works using full-field geometry. The scanning geometry is out of the scope of this work.

Chapter 4

Scattered radiation on breast imaging

The main limitation of DBT is the amount of scattered radiation in the image receptor in each projection, which is significantly higher compared to the one in DM. The reason relies on the absence of an anti-scatter grid in most of DBT units. Therefore, other methods such post-acquisition algorithms for scatter reduction are being developed, requiring, a priori, the estimation of scatter present in the projection images.

The scattered radiation and its influence on image quality in DBT are the main subjects of study in this dissertation. First of all, it is necessary to know the reasons that cause the appearing of scatter, how scatter behaves and, consequently, how it affects the quality of the image.

In this chapter, a review of the literature about the scattered radiation on X-ray mammography imaging is performed. It is listed and detailed, the parameters that, when changed, affects the quantity of scatter present in the image (e.g. compressed breast thickness, glandularity, incident angle, etc.). In addition, the typical techniques used for scatter reduction are briefly described, with a great emphasis on the one chosen for this work.

4.1 Effects of scatter on image quality

When the X-ray beam traverses the breast, it suffers from attenuation by the different tissues that it encountered along the way. The X-rays that reach into the image receptor creates the image, where both primary and scattered radiations are included. As a result, the radiographic image, like the mammogram and DBT projections, expresses the

variations in the attenuation of different tissues inside the breast. However, only the primary X-rays contain relevant information to create the mammography image, since the scattered radiation contributes to the reduction of image contrast and for the increasing of image noise [43].

In digital detectors, the contrast, contrary to what happens in SFM, can be adjusted to improve the image display. However, the imaging performance is influenced by three factors: the efficiency of the detector, geometry alignment and x-ray scatter [43].

For digital imaging systems, the signal difference-to-noise ratio (SDNR) is used to measure the detectability of an object [88]. This parameter can be also influenced by the scattered radiation. The relationship between the SDNR and contrast with scatter is explained below with a simple example [89].

Considering an X-ray beam penetrating a uniform material with thickness x_1 and inside there is an object with thickness x_2, as shown in Figure 4.1. The material and the object have different linear attenuation coefficients, μ_1 and μ_2 respectively.

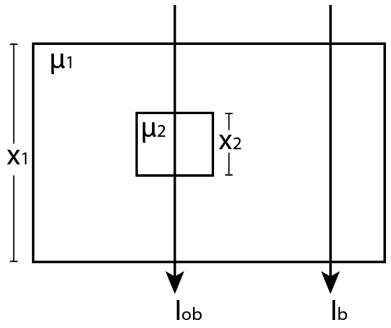

Figure 4.1: An X-ray beam traverses a material with thickness x_1 and inside it contains a small object with thickness x_2. The material and the object have different compositions, which means they have different linear attenuation coefficients. After the X-rays exit the material, the intensity of the transmitted radiation in the background is higher than that one that passes through the object. This example is an adaptation taken from the book "Handbook of Medical Imaging: vol. 1 Physics and Phychophysics" [89].

The contrast of the object is given by the following formula:

$$C = \frac{I_b - I_{ob}}{I_b} \tag{4.1}$$

where the I_b is the intensity in the background surrounding the object and I_{ob} is the intensity within the region of the object of interest. The intensity signal is the combination of the primary X-ray signal (P) and the scattered X-ray signal (S):

$$I_b = P + S \tag{4.2}$$

Furthermore the intensity signal can be also be described according to the Beer-Lambert law (Equation 3.15). The scatter signal has a small variation within the object region and the adjacent background, so it is assumed that the scatter intensity signal (S) is the same for both [90]. The intensity signal for the object is then:

$$I_{ob} = P.e^{(\mu_1(E)-\mu_2(E))x_2} + S \tag{4.3}$$

Rearranging the Equation 4.1, the contrast can be given by the next formula:

$$C = \frac{1 - e^{(\mu_1(E)-\mu_2(E))x_2}}{1 + \frac{S}{P}} \tag{4.4}$$

The Equation 4.4 shows that contrast depends on the thickness of the object of interest (x_2), beam energy ($\mu_1(E) - \mu_2(E)$) and also on the scattered radiation. The degree of contrast degradation increases with the increase of amount of scatter. According to Barnes [90], even small quantities of scatter can cause significant loss of contrast.

As previously stated, the SDNR characterizes the detectability of an object and it has been used in several optimization studies to find the optimal energy which maximizes the quality of the image [88, 91, 92]. This quantity is most valued due to its capability to be independent of many image-processing operations such windowing (e.g. changes in the contrast window and level settings) [88]. The SDNR can be expressed as:

$$SDNR = \frac{I_b - I_{ob}}{\sigma_b} \tag{4.5}$$

where σ_b is the noise in the background and it corresponds to the average value of an area in the background which has the same size as the object [88].

Combining the Equation 4.1 and 4.5, it is obtained the equation that relates the SDNR with contrast:

$$SDNR = \frac{C.I_b}{\sigma_b} \tag{4.6}$$

It is clear now that scattered radiation has a deleterious effect on image quality and, therefore, the reduction of scatter to the minimum amount possible is the main goal for

mammography and especially for DBT to obtain images with the maximum SDNR and contrast achievable.

4.2 Quantification of scattered radiation

The scatter is characterized by its magnitude and its spatial distribution upon the image receptor. These information is very useful for the development of methods for scatter reduction.

4.2.1 Magnitude

The magnitude of scattered radiation that hits in the imaging detector can be measured using the scatter-to-primary ratio (SPR) or the scatter fraction (SF) [44].

$$SPR = \frac{S}{P} \tag{4.7}$$

$$SF = \frac{S}{P+S} \tag{4.8}$$

where S is the integrated energy due to the scattered radiation within the region of interest and P is the integrated energy due to the primary radiation within the region of interest. These quantities depends on many parameters such the compressed breast thickness, glandularity of the breast, incident angle, X-ray spectrum, etc. (see Section 4.3).

4.2.2 Spatial distribution

In terms of spatial distribution, the point spread function (PSF) is commonly used to assess the performance of the imaging system.

Considering a narrow X-ray beam hitting perpendicularly at the center of the imaging detector, the total PSF of the system is composed of the contributions of primary and scattered PSF. The PSF is given in polar coordinates because it was demonstrated by Sechopoulos et al. [48] that PSF loses its radial symmetry with the increase of the incident angle. Therefore, the PSF of the system is given as [93]:

$$PSF_{sys}(r,\theta) = PSF_p(r,\theta) + PSF_s(r,\theta) \tag{4.9}$$

where $PSF_p(r,\theta)$ is the primary PSF component and $PSF_s(r,\theta)$ is the scatter PSF component. For the study of the distribution of scatter within the image receptor it is the $PSF_s(r,\theta)$, also called scatter PSF, which is important to measure. In general the scatter PSF is normalized to the number of X-ray primary photons that are detected:

$$PSF'_s(r,\theta) = \frac{PSF_s(r,\theta)}{\int_{\theta=0}^{2\pi}\int_{r=0}^{\infty} PSF_p(r,\theta)drd\theta} \tag{4.10}$$

According to Boone et al. [93], the SPR can be measured and is equal to the area under the curve of $PSF'_s(r,\theta)$, thus, the resulting expression of SPR is defined in the Equation 4.11.

$$SPR = \int_{\theta=0}^{2\pi}\int_{r=0}^{\infty} PSF'_s(r,\theta)rdrd\theta \tag{4.11}$$

4.3 X-ray scatter behavior in breast imaging

Several studies have been performed in order to estimate the scattered radiation both in mammography and in DBT. The common method used for this purpose is by Monte Carlo (MC) simulations, however, its main disadvantage is the extensive computation time required [49].

In this section, the behavior of scatter, in terms of its magnitude and spatial distribution, is discussed with respect to some physical parameters related to DBT and mammography, such as: compressed breast thickness and composition, incident angle, X-ray spectrum, air gap and mammography components (compression plate, breast support and cover plate). The following sections are mainly devoted to a review of the literature of scatter radiation problem in mammography and DBT.

4.3.1 Compressed breast thickness

Compressed breast thickness, or breast thickness to simplify, is one of the main causes for the variation of the scatter signal quantity within the image receptor [47, 48, 94–96].

In MC studies about the dependence of scattered radiation on breast thickness, the breast is computationally described as a semi-cylindrical object, in a D-shape, made of a homogenous mixture of 50% of adipose and 50% of glandular tissue with a thin layer of adipose tissue as coating [47, 48]. Nevertheless, those kinds of studies do not have to

be ruled by the same geometrical description of the breast and neither the same material type. For instance, in the work of Barnes and Brezovich [94], the breast thickness was studied on a computational circular phantom made of PMMA, however, their results do not directly apply to a breast composed of 50% of glandular tissue with the same thickness since PMMA is a higher density material.

Despite the differences in experimental setups (considering different X-ray spectrum and different values of air gaps), the conclusion is the same: when the breast thickness increases, the SPR values also increase. Also it was demonstrated that the amount of scattered radiation, that hits the image receptor, has a linear dependence on breast thickness [47, 48, 94–96]. For the 0° projection, Sechopoulos et al. [48] reported a maximum difference in SPR value between breast thickness of 2 cm and 8 cm equal to 70% while Boone et al. [47] achieved a maximum difference of 60%. In the work of Cooper and colleagues [96], the SPR value for a breast thickness of 8 cm was 5.5 times higher than for a 2 cm thick breast considering 43% of glandular composition. Barnes and Brezovich [94] also reported a significant increase of SPR (about 45%) between the PMMA phantom with thickness range of 2 to 6 cm using an X-ray spectrum energy of 27 kVp. However, these values cannot be applied to a real breast phantom with the same thicknesses [46].

Although some divergences are found in the SPR results in the works mentioned above, due to the geometric model adopted by the authors, the breast thickness is the parameter which has the greatest influence on SPR [47, 48, 94–96].

4.3.2 Glandularity

It was found that the glandular composition of the breast has a small effect either on SPR as in the spatial distribution of the scattered radiation [48, 94, 95].

Sechopoulos et al. [48] performed a MC simulation using a breast phantom with 5 cm of thickness, a 31 kVp Rh/Rh X-ray spectrum, a chest wall to nipple distance of 11.6 cm and a glandular tissue composition range of 0 to 100%, in 25% steps. Making use of the geometry and X-ray spectrum described above, Boone et al. [95] measured the SPR in breasts with different thicknesses for three different glandular compositions: 0%, 50% and 100% of glandular tissue. Besides the typical glandular compositions simulated, Cooper et al. [96] quantified the scattered radiation for a breast phantom composed of 43% of glandular tissue using a 28 kVp Mo/Mo X-ray spectrum.

They all revealed that both the SPR and spatial distribution of scatter have a small dependence on breast composition. The maximum difference on SPR between the possible limits of glandular composition (0% and 100%) was about 10% and it was found in the work of Sechopoulos et al. [48].

4.3.3 Incident angle

When studying the behavior of scattered radiation on DBT an important parameter has to be taken into account, which is the incident angle (ϕ). The incident angle defines the angle between the X-ray photon beam and the line normal to the surface of the detector.

With the increase of the incident angle, the distance traveled inside the breast by the X-rays also increases, by a factor of $\frac{1}{cos\phi}$ [43,97]. Since scattered radiation increases with breast thickness, it is expectable that the incident angle has also a notable influence on scatter.

Sechopoulos and colleagues [48] studied the spatial distribution of scattered radiation on a breast phantom with 5 cm thick from a range of incident angle from 0° to 30°, in 6° steps. For a 0° angle projection, the scatter PSF has a radial symmetry, however, with the increase of the incident angle, the scatter PSF progressively loses its symmetric shape and it is more evident for angles superior to 10° [48]. Even so, this effect becomes more perceptible when the breast thickness increases, nevertheless, the breast glandularity and X-ray spectrum have a small influence on the behavior of the scatter PSF [48]. In the work of Liu et al., the asymmetry of the scatter PSF was also observed with increasing of the incident angle [41].

These authors also measured the SPR for different breast compositions, X-ray spectrums, breast sizes and breast thicknesses as function of the incident angle. In all cases, the SPR increases with increasing projection angle [48].

4.3.4 X-ray spectrum

In the literature the X-ray spectrum revealed to have a little dependence on the SPR [47, 48, 94–96, 98, 99]. Different anode/filter combinations were evaluated, for instance: Mo/Mo [47, 48, 96, 98, 99], Rh/Rh [47, 48], Mo/Rh [48] and Tungsten/Aluminum (W/Al) [47]. Except for the W/Al X-ray spectrum, all the others slowly increased their SPR values

for increased energy spectrum. Nevertheless, the differences are small and its influence on SPR and on scatter PSF is not significant.

4.3.5 Air gap

The air gap distance between the bottom of the breast and the detector is present on both mammography and DBT modalities and its value depends on the manufacturer. Nowadays, the values for air gap in the commercial DBT systems ranges from 1.7 cm (Siemens Mammomat Inspiration) to 2.5 cm (Hologic Selenia Dimensions) [29].

Boone et al. [47] studied the behavior of scattered radiation for a range of air gaps from 0 mm to 30 mm, in 1 mm steps, using a 26 kVp Mo/Mo spectrum and a circular breast of 4 cm thick and composed of 50% of glandular tissue. The authors found out that the scatter PSF has a more gradual fall-off when the air gap distance is increased. The SPR demonstrates little variation with air gap distance and the maximum difference is observed for a breast with 8 cm of thickness and it was equal to 11%.

4.3.6 Compression plate, breast support plate and cover plate

Most of the MC studies on mammography and DBT use an ideal geometry, this is: the breast phantom, X-ray source and the detector. However, it was demonstrated that besides the breast, some of the breast imaging components such the compression plate, breast support plate and cover plate, also causes a significant variation on the SPR, especially near the edges of the breast [48, 49, 100].

According to Sechopoulos et al. [48], if those system components are included in the simulation geometry, the estimation of the SPR can increase its value by up to 31% for a DBT exam. In the work of Diaz and colleagues [49], it is stated that within the total of scattered radiation recorded in the detector, 30% is due to the compression plate and breast support plate.

4.4 Techniques for scatter reduction

As seen in the previous sections, scattered radiation could seriously affect the image quality and consequently the detection efficiency of tumor masses or calcification during screening examinations. It is then of paramount importance to introduce techniques

able to try to eliminate or at least attenuate the magnitude of the scatter radiation. The scatter reduction techniques adopted in DBT are usually applied to the projection images before undergoing to reconstruction, otherwise, the excess of scatter contributes for cupping artifacts and to a loss of contrast, which leads to a lower ability to detect lesions, especially for those with similar radiographic properties to the surrounding breast tissue [45, 96, 100].

There are two general types of techniques for scatter reduction: through geometrical scatter rejection [39, 100–102] or by post-processing methods [41, 45, 103]. The two main methods for the geometrical scatter rejection includes: the anti-scatter grids [39, 101, 102] and the use of large air gap [102, 104]. As previously stated, the anti-scatter grids helps to reduce a great fraction of scattered radiation in mammography systems but its application on DBT units is a challenge. Therefore, post-processing methods, described in the following section, appear to be the best alternative for scatter reduction on DBT.

4.4.1 Post-processing methods

The scattered radiation can be attenuated or corrected of the images using post-processing methods. Such methods became to be investigated when digital detectors appeared in breast imaging systems, which allowed the manipulation of images after their acquisition. Using post-processing methods, the scatter can be reduced from the images by a subtraction approach [41, 45, 103, 105] or by a deconvolution [106–108].

In this work, a scatter reduction method based on subtraction was applied onto the projection images.

4.4.1.1 Subtraction

As seen in section 4.1, the intensity signal, for a given pixel of the image receptor, is the sum of primary and scatter X-ray photons. Liu et al. [41] described a method based on the removal of the scatter component of the projection image, in which are included the primary and scattered radiation. In that work, Liu and colleagues obtained 15 projection images from a DBT system (GE tomosynthesis prototype), then, they simulated the exact experimental configuration for each projection angle using MC simulations. In these simulations it was produced two separate images containing only primary and scatter radiation, respectively. After the normalization of the scatter image over the "original"

projection image, it was removed the scatter fraction from the original projection image, and, then, these images free of scatter underwent a reconstruction algorithm.

Other authors implemented a similar subtraction approach to reduce the scatter component on the projection images [45, 103, 105]. This type of approach is very easy to implement, the MC simulations can provide accurate scatter estimations and image quality studies revealed an increase of contrast in the scatter-corrected images [41]. However, the scatter correction method based on a subtraction approach, such the one developed by Liu et al. [41], is characterized by the increase of noise. In addition, scatter estimations, for each acquired image, through MC simulations demands several hours of computation time, making a real challenge the application of this method in clinical practice. Nevertheless, the arrival of powerful computer processors (which lowers the computational time required) and the development of faster strategies to estimate the scatter field can, in a near future, allow the introduction of such method in clinical practice.

4.4.1.2 Deconvolution

Techniques for scatter reduction based on image deconvolution are implemented in the Fourier domain [106-108]. The method's theory is well explained in the works of Ducote and Molloi [106] and Siebert and Boone [107]. The X-ray scatter correction based on a deconvolution showed an improvement in image contrast, better visualization of low-contrast objects and the time of the method's application is a reasonable time to apply the method in a clinical environment [106–108]. However, the use of Fourier transform requires a special attention due to its dependency on the spatial distribution of scatter, since the scattered radiation varies with position in the image, which can lead to an increase of computational time [107]. Moreover, Seibert and Boone [107] reported an increase of noise in the deconvolved images.

Chapter 5

Materials and Methods

In this chapter, a description of the materials and the applied methodology is performed. This chapter is subdivided into ten sections. In Section 5.1, the relevant features of the DBT system used for the experimental measurements are presented. According to its finality, two types of phantoms were considered in the clinical environment: for dose measurements, using an ionization chamber that is described in Section 5.3, a breast-shaped rigid phantom was used and for image acquisitions, a PMMA phantom made of several slabs of PMMA of different thicknesses. In Section 5.2, a brief description of both phantoms is showed.

This work has a very strong component in computing by Monte Carlo (MC) methods, specifically through the PENELOPE code, thus, the basic concepts of MC simulations and computer code system PENELOPE and also the structure of PenEasy, a general-purpose main program of PENELOPE that was used for dose calculations and image acquisitions, are summarized in Section 5.4. In Section 5.5, the procedure to create the spectral data of the several polychromatic X-ray spectrums is explained.

Finally, in the sections 5.6 to 5.13 several methodologies were introduced for: backscatter factors and MGD determination, evaluation of image quality, determination of signal loss and SPR, the study of scatter dependence on W/Rh X-ray energy spectrum, the pixel-by pixel analysis of the X-ray energy spectrum and, at last, the description of the subtraction-based method for scatter reduction.

5.1 DBT system

For the DBT image acquisition and data measurements, a Siemens Mammomat Inspiration system [109] was used (see Figure 5.1). This equipment is in operation at the Instituto Português de Oncologia de Lisboa Francisco Gentil (IPOLFG) in Lisbon, Portugal.

Figure 5.1: DBT unit used in this work.

This unit has the flexibility to perform screening and diagnostic standard mammography, biopsies and breast tomosynthesis [109]. Therefore, due to this multitasking functionality, a direct comparison of dose between FFDM and DBT exams can be done. For DBT acquisition, some technical specifications of this equipment can be consulted in Table 2.1 of Chapter 2. The imaging detector has dimensions of 24 cm x 30 cm, nevertheless, the area for survey exposure can also have the dimensions of 18 cm x 24 cm. The image matrix is composed of 2816 x 3584 pixels (24 cm x 30 cm) or 2016 x 2816 pixels (18 cm x 24 cm), and in both cases the pixel size is equal to 85 μm.

The Siemens Mammomat Inspiration allows three different acquisition modalities: manual, OpDose and AEC (Automatic Exposure Control). In manual mode, all the parameters related to the exposure (tube voltage and current-exposure time product) can be manually adjustable by the operator. In OpDose mode the exposure parameters are automatically chosen by the equipment system for optimized patient dose and the AEC is a semi-automatic mode that allows the operator to adjust manually the voltage but the current-exposure time product (mAs) is pre-determined by the system according to the breast thickness.

In terms of compression force, this unit enables to choose between a manual mode and an automatic adjustment by the system (OpComp mode), where a function selects the optimum compression force for a given breast thickness.

5.2 Phantoms

According to the type of measurements to be performed, two types of phantoms were used in this work.

For the system validation, determination of MGD and backscatter factors, different slabs of PMMA (Mammographic Phototimer Consistency Tool, model 159A, Gammex Inc.) [110] were employed (see Figure 5.2). These slabs had different thicknesses, which in combination allow the measurement of entrance surface dose for different thicknesses. Each PMMA slab has dimensions of 14 cm x 14 cm.

Figure 5.2: Slabs of PMMA.

A breast-shaped rigid phantom (MTM 100) [111] was used for image acquisition. The 4 cm thick phantom is composed homogeneously of equal parts of glandular and adipose tissue, and coated with 5 mm layer of adipose tissue. This phantom is appropriate for imaging studies since in its interior has several lesions, such as microcalcification clusters, tumor masses, and fibrous structures in different proportions (see Figure 5.3).

5.3 Ionization chamber (IC)

An IC is a type of radiation detector and consists of a certain volume filled with gas between two electrodes connected to a high voltage supply. Ion pairs are created when

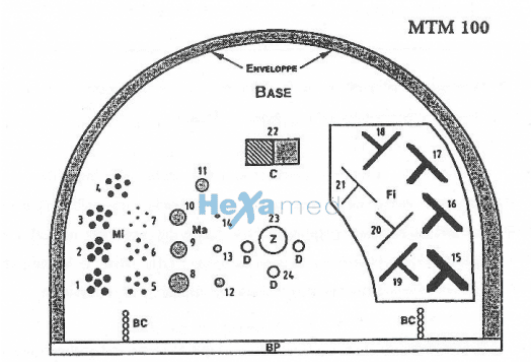

Figure 5.3: Interior of the MTM 100 phantom [111].

ionizing radiation traverses the gas volume, thus, as they are positive and negative charged carriers they are attracted by the electrodes creating a current possible to be measured.

For this study a spherical IC (6 cm^3 SFD Mammo Chamber Type 34069) [112] was used (see Figure 5.4). This IC has a sensitive volume of 6 cm^3 filled with air and its thin external protection is made of PMMA. The calibration of this radiation detector was performed by the Metrology Laboratory of Ionizing Radiations (Campus Tecnológico e Nuclear, IST/UL) and has an associated uncertainty of approximately 5%.

Figure 5.4: A similar IC was used in this work [112].

Two types of measurements were performed using the IC. Firstly, for a given phantom thickness (2, 4, 6 and 7 cm) the IC was placed on the upper surface of the PMMA phantom, as shown in Figure 5.5a, to measure the entrance surface dose (ESD). Secondly, the phantom was removed but the IC was kept in the same position in order to measure the air kerma free in air (K_{air}), as shown in Figure 5.5b. The importance of measuring the ESD and K_{air} is explained in Section 5.6.

For reproducibility purpose, the PMMA phantom was aligned with the center of the detector and one of the sides was coincident to the chest wall plane. The IC was placed at the top surface of the phantom and 6 cm ahead of the chest wall plane.

Figure 5.5: Experimental configurations. a) To measure the ESD, the PMMA phantom has to be included and for b) the measurement of K_{air}, the IC remains in the same position even with the absence of the phantom.

5.4 Monte Carlo methods

Monte Carlo (MC) methods designate a set of modeling techniques and a class of numerical methods based on the principles of probability theory and statistics to simulate the stochastic nature of the interactions of ionizing radiation with matter and particle physics.

In MC simulations, the trajectory of each simulated particle, and its secondary particles (if any), is tracked individually and it is usually named as history. Furthermore, each history terminates when the particle suffers an interaction causing its absorption, or its energy decreased to a value below than a pre-defined threshold or after multiple scattering interactions. In order to simulate these histories an interaction model is required. Each interaction process has to be characterized in terms of its corresponding differential cross section [113] which determines the distribution of probabilities of the random variables that characterizes the trajectory of particles, such as: the mean free path between successive interaction events, type of interaction, loss of energy and angular deflection of each particle, energy and direction of the generated secondary particles (if any) and also the final states of the interactions [113].

For a minor statistical uncertainty and more reliable results, a great number of histories must be simulated but at the expense of the increase of computational time. However, the introduction of powerful computer processors and reasonable memory storage allowed the easy implementation of MC simulations in several computational physics areas. Furthermore, nowadays, it is an essential tool for a wide range of studies in the physics area,

since it represents a cheaper, flexible and safer method to evaluate system configurations and also to explore new configurational rearrangements.

Over time, different MC codes have been developed for the simulation of radiation transport and the most used in physic of radiations are: the ETRAN [114], EGS4 [115] and PENELOPE [116] for the electron-photon transport; the MCNP/MCNPX [117,118], GEANT4 [119] and FLUKA [120] that besides photon-electron transport also tracks neutrons and heavy charged particles.

In this work, the PENELOPE code as MC method was used [116].

5.4.1 PENELOPE

PENELOPE code [113] is an acronym for PENetration and Energy Loss of Positrons and Electrons which performs MC simulations of electrons, photons and positrons transport in arbitrary materials in the energy range from 50 eV to 1 GeV. The PENELOPE code system consists of subroutines written in FORTRAN code, a database that contains the necessary information for creating material cross-section files and three main programs (penmain, pencil and penslab) which differ in terms of geometry description.

The FORTRAN sub-routines are organized in five source files: the penelope.f which includes the routines for transport simulation, the pengeom.f which allows the particles transport through quadric geometries, the penvared.f that contains routines for variance-reduction, the material.f which is the main program for the creation of cross-section material files and the timer.f which includes routines associated with simulation time.

Apart the main PENELOPE programs listed above, another general-purpose main program was used, which was PenEasy. Both Penmain and PenEasy have a tally that reports the energy deposited per history in each material and allows the simulation of particle transport in quadric surfaces, even though, PenEasy also enables the use of voxelized geometries and the combination of overlapping quadrics and voxelized models. However, for this work, the PenEasy program was the one that best fits the required purposes, since it has a specific tally that allows the creation of a simulated image.

5.4.2 PenEasy

PenEasy (version 2015-05-30, compatible with PENELOPE 2014) [121] is a general-purpose main program for the PENELOPE MC system and, since it is an open source

code, its modulation is doable.

This program, like the other main PENELOPE programs, is coded in FORTRAN language and its algorithm consists of repeating the sequence of calls to subroutines JUMP (calculates the distance to the next interaction event), STEP (determines if an interface is crossed before completing the step) and KNOCK (simulates the effect of the interaction and returns the energy lost by the particle) [122].

There are four different ways to halt the simulation: (1) the number of histories defined by the user at the beginning of simulation has been completed, (2) the statistical uncertainty defined by the user for a certain tally has been reached, (3) the allotted time has been exhausted or (4) the user itself terminates the simulation by using a "stop" command [122].

The goal of PenEasy program is to allow users to make use of PENELOPE code without having to write their main program. The operation of PenEasy is completely oriented from the input file that contains the following sections:

•**General simulation settings** – In this section is defined the total number of histories to simulate and allotted time (real time or CPU time).

•**Source description** – PenEasy allows the user to choose between two types of source models: Source box isotropic gauss spectrum or Souce phase space file (initial particle states are read from an external phase space file), within the scope of this work only the first option is detailed. The source box isotropic gauss spectrum model allows the definition of a wide variety of sources shapes and spectra, in this way, the user defines the type of particles, coordinates of the source, its direction and semi-angular beam aperture and also introduces the values of spectral energy or monoenergetic energies.

•**Geometrical section (section PENGEOM+PENVOX)** – Like it was mention above, three possible geometry models are feasible with PenEasy: quadratic geometries, voxelized geometries or a combination of both geometries. For this study, only quadric geometries were considered. In these geometry files (files with extension .geo) are defined all bodies that represent the real geometric system. Each body represents a volume limited by quadric surfaces and is composed of homogeneous material. The definition of a body is done by indicating its limits (quadric surfaces) and the index value of Side Pointer of each quadric surface (-1 if the geometry is inside the quadric surface or +1 if the geometry is outside the quadric surface) and specify the material that composes it.

• **Description of each body's material and transport parameters** – According to the ascending number of bodies that are listed in the geometry file, in this section, the material files also appeared in an ascending mode in order to match its geometrical description. The user can create its own material files through the application available in PENELOPE code (executable material.exe). In this application, the material's files can be generated in two different ways: by inputting an index number associated with the PENELOPE's database (which contains 280 pre-defined materials) or by the introduction of some essential information about the material (chemical composition, density and mean excitation energy). Moreover, the transport simulation parameters which controls the simulation are expressed for each material and they are:

◦**EABS** – Cutoff energy, which means that the value introduced in this parameter represents the maximum value of energy for a given particle (photon and charged particle) before it is locally absorbed.

◦**C1** – Average angular deflection produced by multiple elastic scattering between two consecutive hard collisions of charged particle.

◦**C2** – Maximum average fractional energy loss between consecutive elastic events of charged particle.

◦**WCC** – Cutoff energy for inelastic collisions of charged particles.

◦**WCR** – Cutoff energy for bremsstrahlung emission.

•**Tally sections** – In this section, several tallies according to its finality are available. Each tally has specific parameters needed to be set and a relative statistical uncertainty that can be defined by the user. In this work, only the Tally pixelated imaging detector (to obtain the simulated images) and Tally energy deposition (to estimate the absorbed dose in each material) were used.

5.4.2.1 Tally pixelated imaging detector

To generate an image of the simulated configuration system, the pixelated imaging detector tally has to be activated and in Figure 5.6 an example of its interface is shown. In all MC simulations, an ideal detector with 100% of absorption efficiency was considered.

Firstly, the body identification in the geometry file that corresponds to the detector is performed. This step is accomplished by using the number of the detector's material that was defined in the section PENGEOM+PENVOX. The primary photons are not the only

```
[SECTION TALLY PIXELATED IMAGING DETECTOR v.2015-02-06]
 OFF                              STATUS (ON or OFF)
 1                                DETECTION MATERIAL
 0                                FILTER PHOTON INTERACTION (0=NOFILTER, -1=UNSCATTERED, 1=RAYLEIGH, 2=COMPTON,
                                  3=SECONDARIES, 9=MULTISCATTERED)
 0   100                          X-PIXEL SIZE(cm), No. X-PIXELS (ENTER 0 IN EITHER FIELD FOR AUTO)
 0   100                          Y-PIXEL SIZE(cm), No. Y-PIXELS (ENTER 0 IN EITHER FIELD FOR AUTO)
 1                                DETECTION MODE (1=ENERGY INTEGRATING, 2=PHOTON COUNTING, 3=PHOTON ENERGY DISCRIMINATING aka SPECTRUM)
 1.0e3                            ENERGY DEPOSITION THRESHOLD (eV) FOR MODE=2 (IGNORED FOR OTHER MODES)
 0.0  1.0e9  100                  EMIN,EMAX(eV), No. OF E BINS FOR MODE=3 (IGNORED FOR OTHER MODES)
 0.0  0.0                         ENERGY RESOLUTION, ENTER A(eV^2),B(eV) FOR A GAUSSIAN WITH FWHM[eV]=sqrt(A+B*E[eV])
 1                                REPORT FORMAT (1=COLUMNAR, 2=MATRIX, 3=BINARY)
 0.0                              RELATIVE UNCERTAINTY (%) REQUESTED
[END OF PID SECTION]
```

Figure 5.6: Tally pixelated imaging detector from the input file of PenEasy.

type of photons that reach the detector and also photons that suffer scattering events (one or multiple scattering interactions) are detected. Therefore, the user can obtain different images by choosing the filter of photons according to the interactions they have undergone and three possible detection mode choices are available:

•Energy integrating - the image signal is, for each pixel, the energy deposited (eV) per unit pixel area (cm^2) per simulated history;

•Photon counting - the image signal is the number of counts per unit pixel area per simulated history, where a count is scored when the energy deposited in a pixel exceeds the threshold value defined by the user;

•Photon energy discriminating mode - a full pulse height spectrum is tallied for each pixel.

5.4.2.2 Tally energy deposition

The tally energy deposition has been set ON whenever it was necessary to make dose calculations and its relative uncertainty was defined to be 2%. In the tally's report, the total energy deposited is shown in each material and is represented as electron-volt per history (or particle).

To avoid the misinterpretation of the results, it is advisable to generate material files with a unique name for the situation when different geometric components are made of the same material, for instance, the outer shell of the IC and the phantom slabs are both made of PMMA, so, two equal material files were created but with different names (PMMA.mat and PMMA2.mat respectively). Otherwise, the value of energy deposited in the PMMA material reports to the sum of energy deposited in both components.

As mentioned above, the result is presented in electron-volt per particle (E(eV/part)) but the units of dose, particularly in breast imaging, is given in mGy. First, it is important

to have in mind the definition of electron-volt and Gray. An electron-volt is defined as the amount of energy an electron gains after being accelerated by one volt and given the definition of Gray (see Section 3.3.1.3):

$$1eV = 1.602 \times 10^{-19} J \tag{5.1}$$

$$1Gy = 1J/kg \tag{5.2}$$

Taking this into consideration the energy deposition value can be converted into mGy with the following equation:

$$E(mGy) = \frac{E(eV/part) \times 1.602 \times 10^{-19}}{M_{mat}(kg) \times 1000} \times N_{part} \tag{5.3}$$

where $M_{mat}(kg)$ is the mass of a given material in kilograms and N_{part} is the total number of particles.

5.4.3 Definition of geometries and materials

Over this work, some mammographic features, such as the breast support, compression plate and cover plate, were included in the geometry file for a more realistic system configuration but also because it was proved that they have an influence on the amount of scattered radiation that is present in the image [48, 49].

Due to the lack of information about the real thickness of each component (cover plate, breast support and compression plate) for the Siemens Mammomat Inspiration system, the values of thickness reported in published data [48, 49] for the Hologic Selenia Dimensions system were used. Moreover, the air gap distance between the breast support and the detector was considered to be 17 mm, according to the information available in the review article of Sechopoulos [29].

In Table 5.1 the components that were designed for the simulations, description of their dimensions, material type and density are reported. The material files for those components were generated through the material files available in the database of PENELOPE code.

To create the material files for the adipose and glandular tissue (in different glandular percentages), their elemental compositions were taken from Hammerstein et al. [123].

Table 5.1: List of components used in the MC simulations.

Name of component	Dimensions (cm)	Material	Density (g/cm^3)
Detector	24x30x0.025	Selenium	4.50
Cover plate	24x30x0.0127	Mylar	1.40
Breast support	24x30x0.1	Carbon fiber	1.70
Compression plate	24x30x0.2	Polycarbonate	1.20
IC (interior)	Radius = 1.5 cm Height = 0.859 cm	Air	0.001
IC (outer shell)	Radius = 2 cm Height = 1 cm	PMMA	1.19

Table 5.2: Density of glandular tissue considering 25%, 50%, 75% and 100% glandular fractions, adipose tissue and microcalcification.

Tissue	Density (g/cm^3)
Adipose tissue	0.950
25% glandular tissue	0.9575
50% glandular tissue	0.9850
75% glandular tissue	1.0125
100% glandular tissue	1.040
Microcalcification composition (calcium fluoride)	3.180

The tumor mass and microcalcification were considered to be made of 100% of glandular tissue and calcium fluoride, respectively. In Table 5.2, the corresponding density for each tissue used in this work is shown.

5.5 Energy spectrum

In this study several polychromatic X-ray spectra were considered in the MC simulations, between 25 kVp and 29 kVp for a tungsten target and a 0.05 mm thick rhodium filter. The spectral data used as input source were obtained through the X-ray spectrum simulation tool available online on the website of Siemens [124], which is based on the algorithms developed by Boone et al. [125, 126].

In this free application, the user selects the peak tube voltage (within the range of 18 to 40 kVp, in 1 kVp steps), chooses the filter's material and introduces its thickness, and input the value of the air kerma behind the last filter [124]. As a result, an excel

file with the information about the spectral data is obtained. These spectral data has an uncertainty in photon fluence and spatial and energy distribution, of approximately 10-15% [124, 125].

5.6 Determination of backscatter factors

The dosimetric formalism for breast imaging is described in Section 3.4 of Chapter 3 and the mean glandular dose for a complete DBT acquisition is given in the Equation 3.33. In such equation, the K_T parameter expresses the incident air kerma measured at the upper surface of the breast without the effect of backscatter, however, in this study another parameter to assess the MGD was used, which is the entrance surface dose (ESD).

The ESD is the average absorbed dose in air with the contribution of backscatter effect from the phantom. Therefore, the new equation to assess the MGD (see Section 5.7) uses the ESD quantity but also needs a backscatter correction factor. The backscatter factor (BSF) can be estimated using the following formula:

$$BSF = \frac{ESD}{K_{air}} \tag{5.4}$$

where K_{air} is the air kerma free in air and is measured with the use of an IC without the presence of the phantom. For a complete DBT acquisition, the total ESD and BSF are the cumulative sum of their values in each of the 25 projections.

Besides the ESD and K_{air} values obtained from experimental measurements, theirs values were also calculated through MC simulations for comparison purpose, therefore, two values of BSF were determined: the $BSF_{measured}$ and the $BSF_{simulated}$ respectively.

5.7 Determination of MGD

Taken into account what was explained in the previous section, the new formula to calculate the MGD can be then defined by:

$$MGD_{DBT} = ESD \times g \times c \times s \times T \times \frac{1}{BSF} \tag{5.5}$$

where the values for g-, c-, s- and T-factors are tabulated as function of breast thickness and PMMA thickness and are provided in the Appendix A: Tables A.1–A.4.

For each PMMA thickness, two MGD results were obtained: the $MGD_{measured}$ and the $MGD_{simulated}$. The $MGD_{measured}$ derives from the Equation 5.5 using the ESD and BSF values obtained from experimental measurements and $MGD_{simulated}$ from MC simulations estimations.

5.8 Evaluation of image quality

The image quality optimization of the DBT system involves a compromise between radiation dose and image quality. This last parameter can be accomplished by applying a higher dose as long the image noise is only dominated by quantum noise [88], thus, the mean glandular dose should be kept at the lowest value possible to achieve a reasonable image quality, according to the ALARA (As Low As Reasonably Achievable) principle.

In this work only quantum noise was taken into account while the other noise components (electronic noise and structured noise) were neglected. The image quality was assessed by the determination of two parameters: difference signal-to-noise ratio (SDNR) and figure-of-merit (FOM).

5.8.1 SDNR

To measure the detectability of an object such as a tumor mass or a calcification in an image, the SDNR is used. According to P. Bernhardt et al. [88], this parameter is defined as the ratio between the mean signals differences of the object of interest S_O and the background S_B and the standard deviation of the noise σ_B in the background, as the Equation 5.6 describes. The noise is averaged over an area which has the same size as the object of interest.

$$SDNR = \frac{S_B - S_O}{\sigma_B} \tag{5.6}$$

This quantity is also influenced by the scattered radiation and the relationship between SDNR and contrast is explained in the Section 4.1 of Chapter 4.

5.8.2 FOM

The FOM [36, 91] is a quality factor that is used to compare techniques and to find the one that is optimal for the system under investigation. This parameter is set in terms of image quality and dose delivered to the patient, as it is described in the following equation:

$$FOM = \frac{SDNR^2}{MGD} \tag{5.7}$$

It is known that scatter degrades the image contrast [43], therefore, and according to the Equation 4.6 the SDNR quantity is lower for images that include scatter than for those who are scatter-free. A study to determine the optimal energy that maximizes the image quality when scattered radiation is (and not) included on images was performed. The determination of FOM was done only through the analysis of images resulted from MC simulations using the imaging tally of PenEasy. Those simulated images were obtained only for the CC view and 0° projection.

First of all, the breast was defined as a semi-cylinder of radius 8.75 cm with a certain thickness (2, 4, 6 and 8 cm) with 5 mm layer of adipose tissue and is composed of a homogeneous mixture of adipose and glandular tissue. Three glandular compositions were considered: 25%, 50% and 75%. Furthermore, two lesions, each with variable thicknesses, were considered: a microcalcification (50, 100 and 200 µm) and a tumor mass (3, 5 and 10 mm). The calcification (calcium fluoride) was designed as a cylinder with a radius of 1.5 mm and it was placed at the center of the breast. The same geometrical surface was used to design a tumor mass with 5 mm radius and composed of 100% of glandular tissue.

The Selenium detector with dimensions of 24 cm x 30 cm was implemented as a matrix of 600 x 750 pixels, which means that each pixel has a size of 0.04 cm x 0.04 cm. The X-ray source was considered to be an isotropic point source and the source-to-image distance (SID) was 65 cm. Monoenergetic X-ray energies from 16 to 32 keV, in 2 keV steps, were taken into consideration. In Table 5.3 the parameters used in this study are summarized.

The MGD was estimated for each monoenergetic energy and for each case study. Within each of the two sets of MGD values, the maximum value of dose was found and a 2 mGy dose was attributed as maximum dose achievable, the rest of the values were normalized over this result. Consequently, the results of FOM become independent from

Table 5.3: Values of the geometric parameters used in Monte Carlo simulation for the determination of the optimal energy in images with and without considering the inclusion of scattered radiation.

(1) Case study	**Breast thickness study**
Glandular composition	50%
Breast thickness	2, 4, 6 and 8 cm
Thickness of tumor	5 mm
Radiation filter	Only primary and no filter (primary+scatter)
(2) Case study	**Breast composition study**
Glandular composition	25%, 50% and 75%
Breast thickness	4 cm
Thickness of tumor	3, 5 and 10 mm
Thickness of microcalcification	50, 100 and 200 μm
Radiation filter	Only primary and no filter (primary+scatter)

dose, which means that deviations in FOM are due to variations in SDNR measurements.

5.9 Determination of signal loss

After completing the tasks proposed for Section 5.8, an optimal energy for each task of both case studies is obtained. This energy maximizes the value of FOM and its absolute value is important for measuring the signal loss due to the presence of scattered radiation on images. The signal loss, SL (%), is given by:

$$SL(\%) = (1 - \frac{val1_{max}}{val2_{max}}) \times 100\% \tag{5.8}$$

where $val1_{max}$ is the absolute value of the maximizing energy for the task free of scatter and the $val2_{max}$ is the absolute value of the maximizing energy for the same task that includes scatter in its images.

5.10 Determination of SPR

The SPR quantifies the magnitude of scattered radiation that reaches the image receptor and its formula is given by the Equation 4.7. In this study, the scatter dependence on glandular composition, projection angle and position of measurement was evaluated. In order to calculate the SPR, the no photon interaction filter (primary + scatter) was

used considering the optimal energies of the case study number 2 (see parameters in 5.3). In addition, further simulations were performed for each task adding two new projection angles: 12° and 24°.

After the new pack of simulations was completed, two separate images from each task were acquired: one image was generated only with primary radiation and the second one with the no photon interaction filter, which means that, all the radiation (primary + scatter) hitting the detector was included. Using the Image J program [127], an image subtraction was made in order to obtain a scatter-only image. Then, dividing the scatter-only image to the primary radiation image, maps of SPR for each task were obtained.

With the help of Image J, the SPR was measured in three regions-of-interest (ROIs) located in different positions: (1) near the chest wall, (2) in the center of the breast which includes the lesion (microcalcification or tumor mass) and (3) near the nipple area. In Figure 5.7 the position of the three ROIs is shown. An image matrix of 600 x 750 pixels was implemented with a pixel size of 0.04 cm x 0.04 cm. Each ROI had the same pixel area that covered an area of 4256 pixels. In this type of study the simulated pixel dimensions are not the same as the real pixel dimensions of the DBT/DM system used for phantom measurements (85 μm pixel size). However, since the simulation of detectors with such as pixel dimensions is very time consuming, and since the radial lesion dimension here simulated was of 3 mm, the choice of the simulated pixel dimension was chosen according to a compromise between these two factors [91].

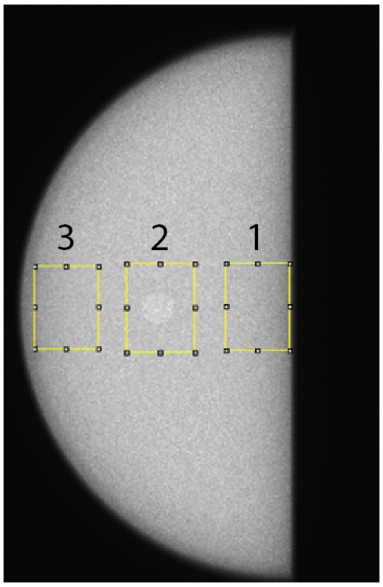

Figure 5.7: The SPR was measured inside of each ROI that is shown in the image. In this case, a 5 mm thick tumor is visible at the phantom center.

5.11 Scatter dependence on W/Rh X-ray energy spectrum

To the author's knowledge, in the published literature, no study was performed in order to evaluate the scatter dependency on a W/Rh X-ray energy spectrum. As seen in Section 4.3.4, the X-ray spectrum revealed to have a little or no dependence on the SPR when the filter/anode combination considered was Mo/Mo, Rh/Rh, Mo/Rh or W/Al [47,48,94–96,98,99]. Thus, a geometrical configuration (described below) to calculate the SPR was set using MC simulations.

The DBT unit used in this work (Siemens Mammomat Inspiration) operates with a tungsten anode with 50 µm thick rhodium filter as the anode/filter combination. The mathematical breast phantom has a radius of 9.25 cm and is composed of a homogenous mixture of 50% of adipose tissue and 50% of glandular tissue coated with a 5 mm of adipose tissue. Also in the simulation setup are included: a 2 mm thick compression plate made of polycarbonate, a breast support with 1 mm thick and made of carbon fiber and, at last, a detector cover plate made of mylar and a thickness of 127 μm (see Table 5.1). An air gap (AG) of 1.7 cm between the upper surface of the cover plate and the bottom surface of the breast support was implemented. The source-to-image distance (SID) is 65 cm and the stationary Selenium detector has dimensions of 24 cm x 30 cm. This geometrical configuration (see Figure 5.8) is a close approximation of what occurs in real practice [29].

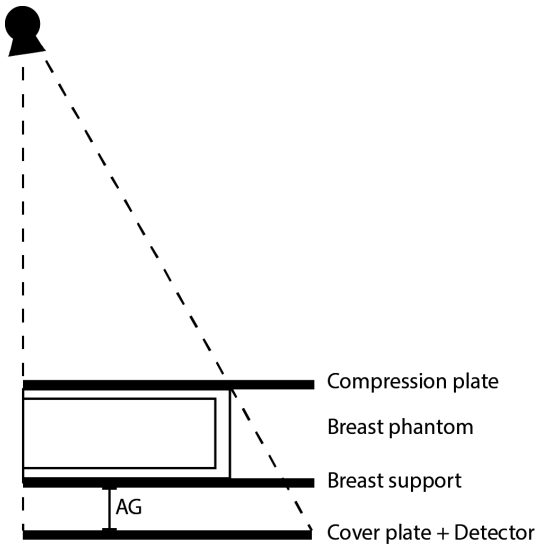

Figure 5.8: Geometry used for the MC simulation of the DBT acquisition system.

In MC simulations, 1×10^8 histories were run for zero angle projection and tube voltage range between 22 kVp and 40 kVp, in 2 kVp steps. The SPR was measured using a circular ROI over the center of the breast phantom.

5.12 Pixel-by-pixel X-ray energy spectrum analysis

Another approach to study the influence of scattered radiation on projection angle and position of measurement is by analyzing the pulse height spectrum (PHS) of primary, Compton, and Rayleigh photons that reach the detector through MC simulations. The PHS gives information about the energy distribution curve of the X-ray source, which in this study was generated by a W/Rh anode/filter combination.

After the generation of the total and only primary maps, an energy spectrum analysis in the lesion and background ROIs (for the projection angles of 0°, 12° and 24°) was performed. For this study, the photon energy discriminating mode was selected as the mode of detection in the tally pixelated imaging detector (see Figure 5.6). Therefore, a full PHS is tallied for each pixel, which means, that it is possible to obtain information of the number of counts, per pixel area unit (cm^2) and per simulated history in each energy bin. The user pre-defines the maximum ($E_{max}(eV)$) and minimum energies ($E_{min}(eV)$) and also the number of energy bins (N_{EB}). Each energy bin has a width (EB_{width}) equal to:

$$EB_{width} = \frac{E_{max}(eV) - E_{min}(eV)}{N_{EB}} \tag{5.9}$$

In this study, a polychromatic spectrum of 28 kVp was simulated, so an energy range from 6 keV to 28 keV and 30 energy bins were selected, causing an energy bin width equal to 733.33 eV.

For the X-ray energy spectrum analysis, a 4 cm thick breast phantom composed homogeneously of 50% adipose and 50% of glandular tissue (with a 5 mm thick tumor mass) was simulated. The selenium detector has dimensions of 24 cm x 30 cm and a pixel matrix of 300 x 375 pixels was considered, making each pixel size equal to 0.08 cm x 0.08 cm. The center of the breast (which includes the tumor) is coincident with the center of the detector. In this way, for the spectrum analysis, three pixels in the matrix that correspond to the location of the tumor, and another three pixels in the background near

Table 5.4: Localization and pixel index of the 6 pixels considered for this study.

Pixel localization	Pixel number	Pixel Index X	Pixel Index Y
Inside the tumor	1	150	188
	2	151	188
	3	150	187
Background	4	163	188
	5	164	188
	6	163	187

the lesion (as shown in Figure 5.9) were considered. In Table 5.4 the localization of the six pixels and its corresponding pixel index are reported.

It is relevant to point out that the tally's output file increases its file size when the number of pixels in the image matrix and the number of energy bins are increased. In the first attempt to simulate the geometrical configuration above described, a matrix of 600 x 750 pixels and 40 energy bins were considered, which led to an output file with more than 2 GB of size. These huge files presented some difficulties to be opened with the available text editors (for instance, the Notepad ++, notepad, WordPad), therefore, an image matrix of 300 x 375 pixels and 30 energy bins were selected in order to create an output file of 400MB size.

The summation of counts for primary, Compton and Rayleigh results were used for the determination of SPR, according with the following equation:

$$SPR = \frac{\sum_{i=1}^{31}(counts_C(i) + counts_R(i))}{\sum_{i=1}^{31} counts_P(i)} \tag{5.10}$$

where $counts_C$(i) is the counts for photons that underwent one Compton interaction in the i-th energy bin, $counts_R$(i) is the counts for photons that underwent one Rayleigh interaction in the i-th energy bin and $counts_P$(i) is the counts for photons that reach into the detector without suffering any interactions in the i-th energy bin.

In order to obtain a discriminated X-ray energy spectrum for each photon interactions (Compton or Rayleigh) or primary photons, the photon interaction filter in the tally was set for the correspondent number (see Figure 5.9). The mean energy (E') for each PHS (see Equation 5.11) and for the entrance spectrum of 28 kVp was also assessed according to:

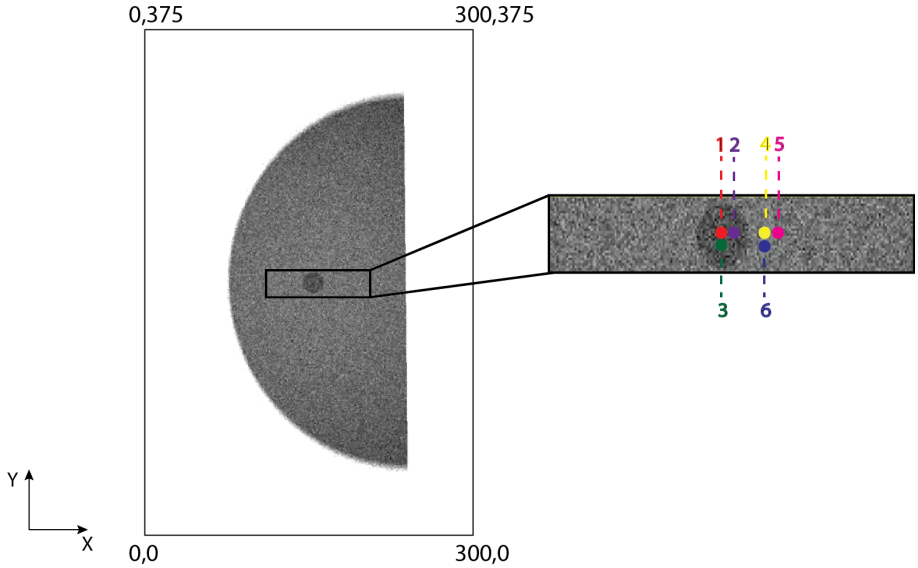

Figure 5.9: Pixel index in image matrix and measured pixel positions (the pixel number corresponds to the number presented in Table 5.4). The represented pixel size is exaggerated for visual effects.

$$E' = \frac{\sum_{i=1}^{31}(EB_{middle}(i) \times counts(i))}{\sum_{i=1}^{31} counts(i)} \tag{5.11}$$

where $EB_{middle}(i)$ is the middle energy of the i-th energy bin and counts(i) is the number of counts in the i-th energy bin.

5.13 Scatter reduction method based on a subtraction approach

As already described in Chapter 4, in this study a subtraction-based method for scatter reduction was applied in order to try to improve the image quality of a DBT image.

A complete DBT image acquisition (25 projection images which are going to be named as "original projection images" to facilitate the method's description) from a Siemens Mammomat Inspiration was performed with a breast rigid phantom (MTM 100), as shown in Figure 5.10a. The values of tube voltage and exposure were determined by the OpDose mode of the DBT system, therefore, a tube voltage of 28 kVp and 160 mAs as current-exposure time product were used in the 4 cm thick breast phantom.

The flat-panel detector made of amorphous selenium (a-Se) has an image matrix of 2816 x 3584 pixels, which means that each pixel has a size of 85 μm. Inside the breast-

shape rigid phantom several lesions (clusters of microcalcifications, tumor masses and fibers, see Figure 5.3) with different dimensions can be observed, however, for the simulation only the cluster of microcalcifications and the greater mass lesion was considered. Each microcalcification of the cluster has 300 μm size and the mass lesion has a radius of 3.2 mm, as it is represented in Figure 5.10c.

A geometry file that best matched the experimental configuration was designed, like shown in Figure 5.10b. For each projection angles of 0°, 12° and 24°, two separate images were obtained: one with only primary radiation (I_P) and the second image includes all the X-ray photons that reaches the image receptor (I_{total}). After this step, maps of scatter (I_S) are obtained using the Image J software [127] by subtracting the image I_P of the image I_{total}. It is important to remark that both simulated images have the same matrix pixel as the original projection images and only the craniocaudal (CC) view was evaluated.

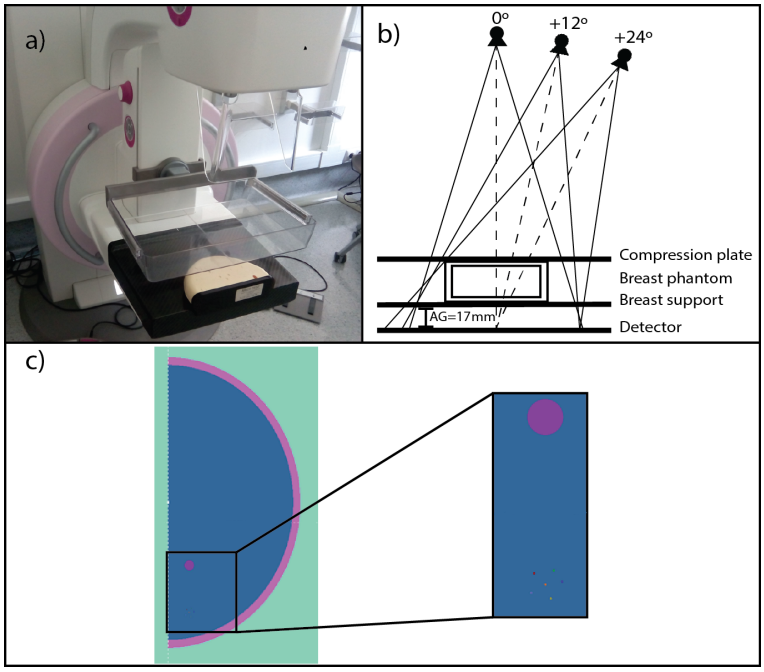

Figure 5.10: Representation of the (a) experimental setup used during the image acquisitions and (b) the geometry adopted for the PENELOPE simulations in profile view. Inside of the simulated breast phantom (c), it was placed a microcalcification cluster of 300 µm thick and a tumor mass of 3.2 mm thick to mimic the lesions that are present in the phantom MTM 100 (see Figure 5.3).

The scatter map subtraction method was applied in a local way. Namely a circular ROI centered with the center of the lesion and also including some near background was created in the original image projection and its maximum pixel value was noted. Meanwhile, the same procedure in the simulated I_{total} was applied to also note the maximum pixel value.

The ratio between those maximum pixel values was used as a normalization factor which was applied over the same ROI within the scatter image.

A pixel-by-pixel subtraction was performed with the help of Image J program, in other words, the scatter component within the ROI from the scatter map was removed from the ROI in the original projection image, and thus, a scatter-corrected image was created. To evaluate the performance of this method, the determination of SDNR within the ROI's area was calculated before and after the application of the method.

Assuming that quantum noise is the predominant noise and the effect of the additional noise (electronic and structured noise) is neglected, Poisson statistics can be applied, thus, the SDNR was calculated according to the following equation:

$$SDNR = \frac{S_B - S_O}{\sigma_B} = \frac{S_B - S_O}{\sqrt{S_B}} \tag{5.12}$$

Chapter 6

Results and Discussion

This chapter aims to analyze the different strategies that were applied, in order to obtain a complete characterization of the scattered radiation behavior and its influence on image quality and dose in DBT examinations. In Section 6.1, the results of the validation of the implemented MC model for the DBT image acquisition system are presented. Using the measured and simulated values obtained from the previous section, the backscatter factors were determined in Section 6.2. The mean glandular dose for each PMMA thickness (2, 4, 6 and 7 cm) using the dosimetric formalism proposed by Dance et al. [86] was assessed and the results are shown in Section 6.3. In addition, in Section 6.4, the influence of compression plate on dose assessment was determined.

For different breast thickness and breast compositions, an optimal X-ray energy that maximizes the image quality was found for breasts with tumors and calcifications of different sizes. The results are shown in Section 6.5. The determination of the signal loss due to the presence of scattered radiation is presented in Section 6.6. In Section 6.7, the results of SPR as a function of projection angle, breast composition, lesion sizes and position of measurement for a 4 cm thick breast are shown. The dependence of scattered radiation on W/Rh X-ray energy spectrum was studied and the result of SPR at different tube voltages is shown in Section 6.8. A different approach to calculate the SPR is by the X-ray energy spectrum analysis which was also useful to compare the pulse height spectrum of the entrance spectrum with the different components of the total spectrum that reaches into the detector (primary, Compton and Rayleigh photons). These results are shown in Section 6.9. Finally, in Section 6.10, an evaluation, in terms of SDNR analysis, of the subtraction-based method applied for scatter reduction in projection images of a

DBT examination is presented.

6.1 System validation

In Table 6.1 the parameters used in the experimental setup and PENELOPE simulations are listed. In order to find the optimal values for tube voltage and current-exposure time product in DBT, the OpDose mode was chosen without placing the IC on the top surface of the PMMA phantom. Also, to protect and avoid eventual damages in this step, the IC equipment (the OpDose mode automatically adjusts the compression force, making impossible to control the process by the user) was removed.

Once the optimal values for current-exposure time product and for tube voltage are known the acquisition mode was changed to Manual and the IC was placed at the top surface of the phantom, like described in Section 5.3. Here the compression force was not a limitation since it can be manually adjustable. With increasing of PMMA thickness, the OpDose mode selected higher values of tube voltage and current-exposure time product.

Table 6.1: Parameters used for the experimental setup and then for the MC simulations.

PMMA thickness (mm)	Equivalent breast thickness (mm)	Glandularity of equivalent breast (%)	Exposure (mAs)	Tube voltage (kVp)	HVL (mmAl)
20	21	97	71	25	0.445
40	45	41	125	27	0.471
60	75	9	200	29	0.491
70	90	4	320	29	0.491

It is known that PMMA is a material with similar effective nuclear charge as the breast composed with 35% of glandular tissue, nevertheless, its density is superior to the density of such breast [94]. Consequently, dose measurements using a certain PMMA thickness do not translate the absorbed dose for breasts with the same thickness, thus, in Table 6.1 the values of equivalent breast thickness and glandularity corresponding for PMMA thickness of 2, 4, 6 and 7 cm which are provided. These values were taken from the European guidelines for quality assurance in BC screening and diagnosis [82] and from the Protocol for the quality control of DBT [87]. The values for half-value layer (HVL is a quantity defined as the thickness of any given material necessary to reduce in 50% the

X-ray beam intensity and , in general, its units is expressed in mmAl) were obtained from the spectral data file provided by the simulation tool [124].

For each PMMA thickness, three values of ESD and K_{air} were measured using the IC, so, the results provided in Table 6.2 are an average of the measurement values. The validation of the image acquisition system of the DBT equipment was done by comparing the average measured values of ESD and K_{air} with the simulated results. The relative difference between results is calculated using the following formula:

$$Relative.Difference(\%) = \frac{value_{measured} - value_{simulated}}{value_{measured}} \times 100\% \quad (6.1)$$

In Table 6.2, the ESD and K_{air} measured and simulated results for each PMMA thickness are reported. Regarding the ESD results obtained from experimental measurements and from calculations, the higher difference (10.96%) was observed for the PMMA phantom with 70 mm of thickness and the lower difference (0.80%) was found for the 40 mm thick PMMA phantom. For K_{air} results, the highest difference was achieved for the PMMA phantom with 20 mm thickness with value equal to 13.65%, while the lowest discrepancy was verified for the PMMA phantom of 60 mm thickness with a 0.55% of difference.

Table 6.2: ESD and K_{air} values obtained from experimental measurements and PENELOPE simulations. The uncertainty related to measurements is 5% and to the simulations is 15%.

PMMA thickness (mm)	$ESD_{measured}$ (mGy)	$ESD_{simulated}$ (mGy)	Relative difference (%)	$K_{air-measured}$ (mGy)	$K_{air-simulated}$ (mGy)	Relative difference (%)
20	1.810 ± 0.091	1.682 ± 0.034	7.07%	1.810±0.091	1.563±0.031	13.65%
40	4.227 ± 0.211	4.261 ± 0.085	-0.80%	4.162 ± 0.208	3.864 ± 0.077	7.16%
60	9.435 ± 0.472	10.179 ± 0.204	-7.89%	9.167 ± 0.458	9.117 ± 0.182	0.55%
70	13.993 ± 0.700	15.527 ± 0.311	-10.96%	13.507 ± 0.675	13.825 ± 0.277	-2.35%

For each simulation, 3×10^9 histories were run which led to a statistical uncertainty of approximately 2%, nevertheless, the spectral data used in the input file also has an associated uncertainty of about 10-15% [124, 125]. Therefore, considering the spectral data uncertainty to be 15%, the simulations results had an overall uncertainty of about 15%. On the other hand, the uncertainties associated with dose measurements are related to the uncertainty of the IC which is about 5%.

In general, a good agreement between experimental values and simulation results was achieved, despite the maximum differences in ESD and K_{air} results were slightly higher than expected (10.96% and 13.65%, respectively), nevertheless, at the level of the uncertainty associated with the simulations, which was 15%, it can be considered that the implemented computational model reproduces the clinical DBT system with reliable results.

6.2 Determination of backscatter factors

Two BSF were determined using the Equation 5.4: the $BSF_{measured}$ for the experimental measurements and $BSF_{simulated}$ for the MC simulation results. Table 6.3 shows the results for both BSF for each PMMA thickness.

The uncertainties related to $BSF_{measured}$ are related with the uncertainty of the IC, which is 5%, while the uncertainties of the $BSF_{simulated}$ are related to the overall uncertainty of the MC simulations (15%).

Table 6.3: $BSF_{measured}$ and $BSF_{simulated}$ for breast thicknesses of 20, 40, 60 and 70 mm.

PMMA thickness (mm)	$BSF_{measured}$	$BSF_{simulated}$	Relative difference (%)
20	1.000 ± 0.050	1.076 ± 0.161	-7.61%
40	1.016 ± 0.051	1.103 ± 0.165	-8.58%
60	1.029 ± 0.051	1.116 ± 0.167	-8.48%
70	1.036 ± 0.052	1.123 ± 0.168	-8.41%

These $BSF_{simulated}$ results were obtained using a W/Rh X-ray spectrum and are in agreement with the published data by the European protocol on dosimetry in mammography [128]. In this protocol, the BSF are tabulated for HVL between 0.25 and 0.65 mmAl and their values ranged from 1.07 to 1.13, while in the absence of HVL information, the BSF is considered to be 1.09. Baptista et al. [129] published results of BSF for a complete DBT using the same DBT system and anode/filter combination as the one used in this work. In their study, the BSF were calculated for different breast thickness and different tube voltages and it ranged from 1.065 to 1.083, which are inferior results than those obtained in this work. This discrepancy becomes more evident with the increase of tube voltage, however, this could be explained due to the fact that they considered for the

current-exposure time product a constant value of 100 mAs, while in this work the mAs has a dependence on the breast thickness.

The results obtained for the measurements are relatively inferior to the MC simulated results for all PMMA thicknesses evaluated leading to an uncertainty between 7.61% and 8.58%, which could be explained due to two main reasons. Firstly, the IC was calibrated only for the tube voltage of 28 kVp and 0° projection, and secondly, the IC has a weak angular response when used for dose measurements in DBT examinations, which according to Bradley and colleagues [130] may underestimate the measured values.

6.3 Determination of MGD

The MGD assessment was based on the formalism described in Section 5.7. Following the MGD results will be reported as: the $MGD_{measured}$ (using the measured ESD and BSF) and $MGD_{simulated}$ (using the simulated ESD and BSF). The conversion factors (g-, c-, s- and T-factors) were obtained from the published data of Dance et al. [85, 86] and are available in the Appendix A: Tables A.1–A.4. In Table 6.4, the results of both MGD and conversion factor values correspondent of each task studied are shown.

The total uncertainty of the $MGD_{measured}$ was estimated to be 14% based on the uncertainty of the measurements using the IC (±5%), the error estimations on the conversion factors (±2.1%) [85] and the inherent uncertainty in the determination of K_{air} given by the European protocol on dosimetry in mammography (±12%) [131]. Concerning the $MGD_{simulated}$, an absolute uncertainty of about 15% was reached based on the uncertainty of the MC simulations (±15%) and error estimations on the conversion factors (±2.1%).

According with the results, the $MGD_{measured}$ values range between 0.825±0.115 mGy and 2.314±0.324 mGy while the $MGD_{simulated}$ varies from 0.712±0.107 mGy to 2.369±0.355 mGy. In this way, the lower difference achieved was for the PMMA phantom with 60 mm of thickness of value equal to 0.55% and the highest discrepancy was equal to 13.65% for the 20 mm thick PMMA phantom. Furthermore, both values of MGD are in agreement at the level of 14% (uncertainty associated with the measured MGD).

Although there are no MGD limits regarding the DBT examination, the European protocol for DBT system [87] advises the usage of the same limiting values established for

Table 6.4: $MGD_{measured}$ and $MGD_{simulated}$ considering a PMMA phantom thickness of 20, 40, 60 and 70 mm. The conversion factors were obtained from the data published by Dance et al. [85, 86] which are provided in Appendix A: Tables A.1–A.4.

PMMA thickness (mm)	g-factor	c-factor	s-factor	T-factor	$MGD_{measured}$ (mGy)	$MGD_{simulated}$ (mGy)	Relative difference (%)
20	0.496	0.908	1.042	0.971	0.825±0.115	0.712±0.107	13.65%
40	0.270	1.038	1.042	0.959	1.166±0.163	1.082±0.162	7.16%
60	0.166	1.225	1.042	0.954	1.853±0.259	1.843±0.276	0.55%
70	0.136	1.270	1.042	0.952	2.314±0.324	2.369±0.355	-2.35%

mammography, which can be consulted in Table 3.2. Taking those values into consideration, both measured and simulated MGD are below the reference value of each PMMA thickness of 20, 40, 60 and 70 mm, which are: 1.0, 2.0, 4.5 and 6.5 mGy, respectively.

6.4 Influence of compression plate on dose assessment

The compression plate is a mammography component which main goal is to uniformly compress the breast into the breast support in order to reduce its thickness causing an attenuation of the overlapping tissue effect. Furthermore, the inclusion of the compression plate on the mammography system also improves the image contrast and lesion conspicuity and lowers the radiation dose.

In this step of the work, the influence that compression plate has on dose was evaluated by measuring the ESD with the IC of a PMMA phantom thickness of 40 mm for a normal DBT acquisition and for a DBT acquisition without the compression plate. The results are provided in Table 6.5 and the parameters used in both tasks for tube voltage and current-exposure time product were the same and are available in Table 6.1.

Besides the value of ESD measured with the IC, its value was also estimated by MC simulations for comparison purposes. The uncertainty of the measurements using the IC was 5% while the simulation results have an associated uncertainty of 15%.

Regarding the results, the $ESD_{measured}$ (5.270±0.264 mGy) for the task that not included the compression plate was higher (more than 1 mGy) than the $ESD_{measured}$ (4.227±0.211 mGy) for a normal DBT acquisition. Assuming the same backscatter factor in both cases ($BSF_{measured}$=1.016±0.051 mGy, see Table 6.3), the values of MGD are:

Table 6.5: Results of measured and simulated ESD for DBT acquisitions with and without the presence of the compression plate.

PMMA thickness (mm)	With compression plate			Without compression plate		
	$ESD_{measured}$ (mGy)	$ESD_{simulated}$ (mGy)	Relative difference (%)	$ESD_{measured}$ (mGy)	$ESD_{simulated}$ (mGy)	Relative difference (%)
40	4.227± 0.211	4.261 ± 0.639	-0.80%	5.270± 0.264	5.887± 0.883	-11.71%

1.166±0.163 mGy for a normal DBT acquisition and 1.453±0.203 mGy for a DBT acquisition without the compression plate. Therefore, the presence of the compression plate, for this experimental setup, led to a dose saving of almost 20%.

For the normal DBT acquisition, the ESD calculated through MC simulations are in conformity with the measured value, revealing a small discrepancy of 0.80%. Regarding the MC simulations for a DBT system without the compression plate, an overestimation of the ESD calculated through simulations over the measured ESD was observed, which represented a relative difference of 11.71% between results. Nevertheless, both ESD values for the two DBT scenarios are in agreement at the level of uncertainty of 15%, which is the uncertainty associated with MC simulations.

6.5 Determination of FOMs

As described in Section 5.8.2, two study cases were evaluated in order to find the optimal energy which maximizes the FOM parameter using the Equation 5.7. In each case study, the MGD was obtained through MC simulations using the tally energy deposition of PenEasy program (see Section 5.4.2.2). The total absorbed dose corresponds to the cumulative sum of each absorbed dose in the glandular tissue for the 25 projections. Subsequently, in each case study (different breast thicknesses and different breast compositions), the maximum value of the total absorbed dose was found and a 2 mGy dose as the maximum dose achievable was attributed. For example, in the case study number 1, the 2 mGy dose was assigned to a breast with 8 cm thick for energy of 26 keV (Figure 6.1b). Also, in the case study number 2, the highest value of dose was found in a breast composed of 75% of glandular tissue for energy of 22 keV (Figure 6.1a). Then, in each case study, the rest of values of dose were normalized over these results.

In Figure 6.1 the curves of MGD for both cases are presented. In all the results, the

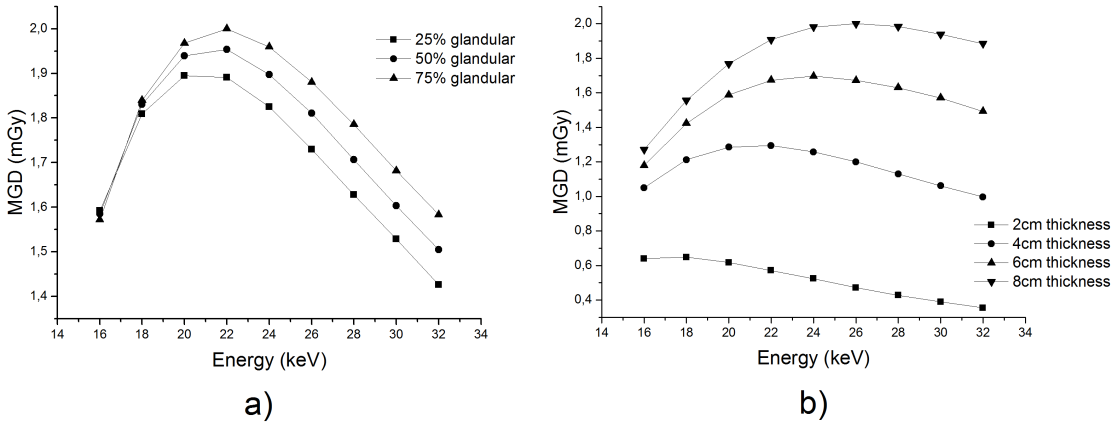

Figure 6.1: Cumulative sum of the doses for the 25 projections (in mGy), for each monoenergetic energy, taking into account (a) different glandular compositions (25%, 50% and 75%) and (b) different breast thicknesses (2, 4, 6 and 8 cm).

uncertainty of MC simulations was smaller than 1%, thereby the error bars on the plots were omitted.

Considering Figure 6.1a, for energies higher than 18 keV, the glandular composition effect begins to be relevant. In fact, it is possible to observe that the MGD is higher for denser breasts (i.e. higher value of glandular composition) than for fatty breasts (i.e. lower value of glandular composition). This effect occurs because in dense breasts the number of absorbed photons is much higher. The maximum dosage was reached at 22 keV for all of the glandular tissue fractions and starting from this energy, the dose values begins to decrease in a linearly way. At last, the MGD values have a maximum variation of about 10% between a 75% glandular composition and a 25% glandular composition breast.

Regarding Figure 6.1b, thicker breasts have higher MGD than breasts with a small thickness. The distance travelled by X-rays in the glandular tissue is bigger for breasts with a large thickness, thus, in this situation, the interactions with matter and subsequent energy deposited are much higher. Also in this case, for each thickness, a maximum value of absorbed dose can be observed. Moreover, as shown in 6.1b, the increasing of breast thickness shifts the maximum of absorbed dose towards higher energies.

In addition, in all PenEasy input files used for this study, 1×10^{10} histories were simulated leading to an associated uncertainty with the FOM analysis smaller than 1%, thereby the graphics presented in the following sections have the error bars omitted.

6.5.1 Case study 1 - Breast thickness study

In this case, a comparison between the optimal X-ray energy for both types of photon interaction filter and for each breast thickness is done (see Table 6.6). It was found that, for each breast thickness, the optimal X-ray energy does not change its value between images simulated with only primary photons and simulated images in which all radiation that hits into the detector is considered.

Furthermore, these results suggest that, for thicker breasts, better image quality is achieved through the use of higher energies, even though, for breast thicknesses of 4 and 6 cm the same optimal X-ray energy of 18 keV was obtained. This observation can be explained due to the fact that higher energetic X-rays have great probabilities to reach into the detector while the X-ray photons with less energy are easily absorbed by the breast tissues.

In the work of di Maria et al. [92], a different MC code was used to also study the optimal X-ray energy for a breast phantom of 50% of glandular composition with a 5 mm thick tumor mass in its center and a monochromatic range of energies. For a breast thickness of 2, 4, 6 and 8 cm the optimal X-ray energy was 14.4, 18.9, 21.9 and 25.4 keV, respectively. Comparing results, a good agreement can be found with the exception of the breast of 6 cm thick which differs from the published value of about 18%. Also, the influence of scattered radiation in the determination of FOM was assessed and, like it was also observed in this work, the optimal energies are not affected by its presence.

Table 6.6: Optimal X-ray energy for which FOM is maximum taking into account different breast thicknesses and two types of photon interaction filters. Those breasts have a glandular composition of 50% and a tumor mass of 5 mm thick placed at the center.

Breast thickness (cm)	Photon interaction filter	
	Only primary photons	No filter (primary+scatter)
2	16	16
4	18	18
6	18	18
8	24	24

The main difference in these results is related to the absolute value of FOM which is lower for images that consider all the radiation. In Figure 6.2a, 6.2b, 6.2c and 6.2d, the

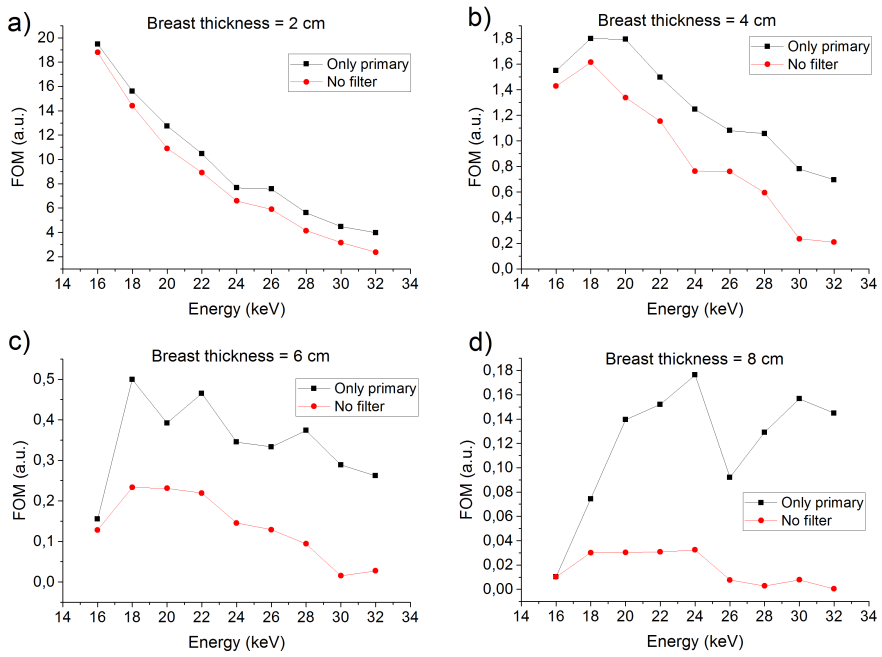

Figure 6.2: Dependence of FOM with X-ray energy and type of photon filter interaction, for the detection of a 5 mm thick tumor mass: (a) for a breast of 2 cm thick, (b) for a 4 cm thick breast, (c) for a breast of 6 cm thick and (d) for a breast of 8 cm thick. All breast phantoms are homogeneously composed of 50% of glandular tissue.

behavior of the FOM parameter in the energy range of 16 and 32 keV for the study case number 1 is shown.

Despite the differences in the absolute values of FOM, for each breast thickness except for the breast of 8 cm thick, the curves of FOM values of the two types of photon interaction showed a very similar behavior. According to the Figure 6.2, the FOM values become smaller when the breast thickness increases, which means, that increasing breast thickness caused a deterioration of the detectability of the 5 mm thick tumor mass.

6.5.2 Case study 2 - Breast composition study

The results of simulations are described for a 4 cm thick breast with different glandular compositions (25%, 50% and 75%) and two lesions (tumor mass and calcification) of variable thicknesses. In Table 6.7 and 6.8, the optimal X-ray energies for the detection of tumors and calcifications for different breast glandular fractions and for the two types of photon interaction filters, respectively, are summarized. In Figure 6.3, the curve of FOM values for each tumor thickness and glandular composition considering both photon interaction filters is presented. Likewise, in Figure 6.4, the curve of FOM values for each

Table 6.7: Optimal X-ray energy for which FOM is maximum taking into account different glandular compositions and different thicknesses of tumors.

Photon interaction filter	Tumor thickness (mm)	Glandular composition (%)		
		25%	50%	75%
Only primary photons	3	18	18	18
	5	18	18	18
	10	18	18	22
No filter (primary+scatter)	3	18	18	18
	5	18	18	18
	10	18	18	18

Table 6.8: Optimal X-ray energy for which FOM is maximum taking into account different glandular compositions and different thicknesses of calcifications.

Photon interaction filter	Calcification thickness (μm)	Glandular composition (%)		
		25%	50%	75%
Only primary photons	50	20	18	18
	100	20	18	18
	200	20	18	20
No filter (primary+scatter)	50	18	18	18
	100	18	18	20
	200	18	18	20

calcification thickness and glandular composition considering both photon interaction filters is showed.

Relative to the detection of tumors, a monochromatic energy of 18 keV was found to be the optimal energy for all the tasks studied except for the tumor of 10 mm thick inside the breast composed of 75% of glandular tissue considering only primary photons as the photon interaction filter. According to the literature [88, 92], the optimal energy should slightly increase for denser breasts and for bigger sizes of tumor, for example, in the work of Bernhardt et al. [88], for the detection of tumors for a breast thickness of 5 cm, an increase of 4% in the optimal energy between breasts composed of 25% (24 keV) and 75% of glandular tissue (25 keV) was observed. In another work, developed by di Maria et al. [92], an increase of 6% in the optimal energy value between breasts with lower (18.5 keV) and higher density (19.7 keV) was found when a 5 mm thick tumor was inside of a breast with 4 cm of thickness. Moreover an increase of 1.5% in the optimal quantum energy between tumors of 1 (18.8 keV) and 10 mm (19.1 keV) was reported for a 4 cm thick

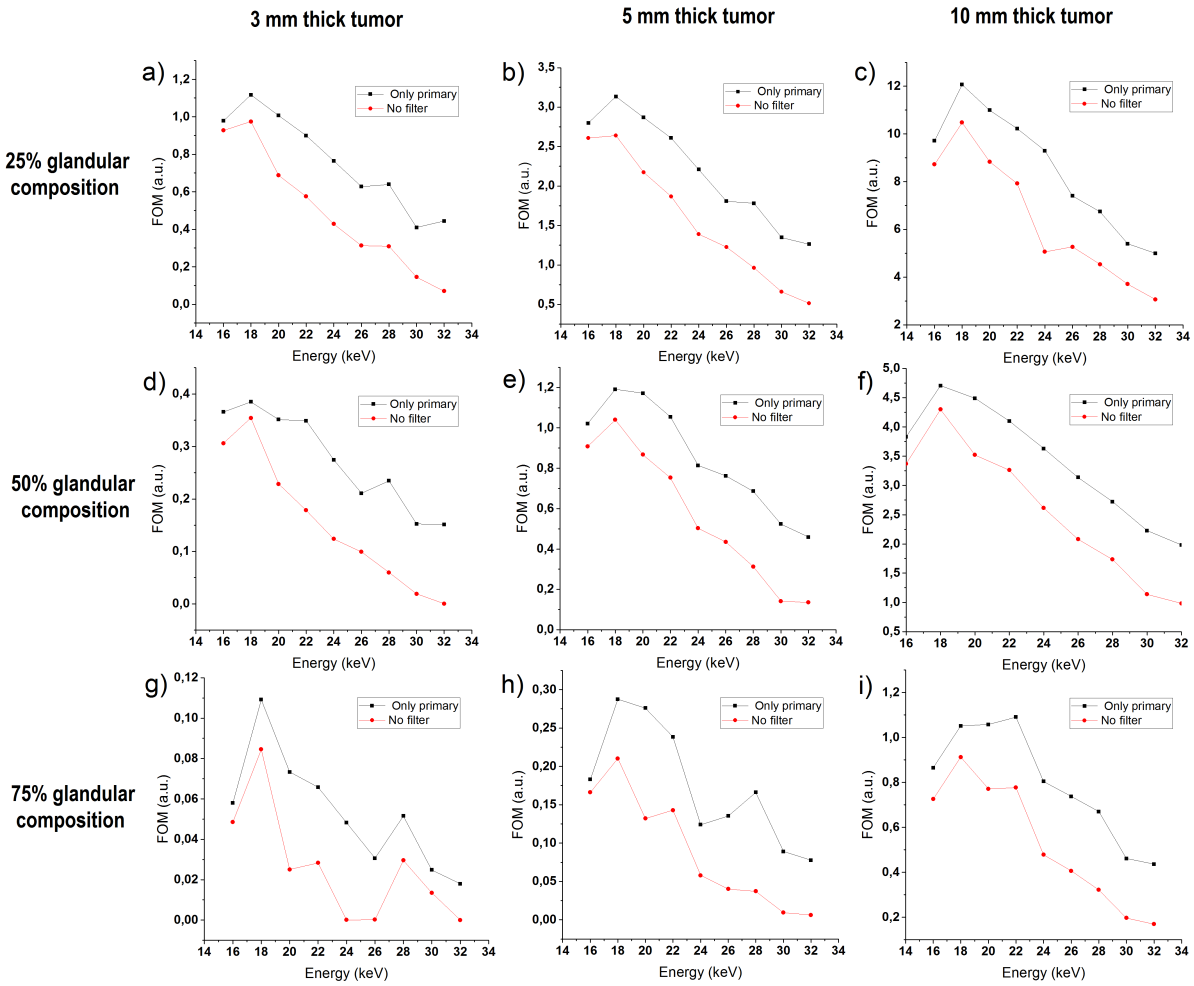

Figure 6.3: FOM results obtained by MC simulations for a 4 cm breast thick for different glandular compositions (25%, 50% and 75%) and sizes of the tumor mass (3, 5 and 10 mm) and types of photon interaction filter.

breast composed of 50% of glandular tissue. In this work, those increasing factors are very small to be noticed because it was considered a 2 keV steps between monoenergetic energies, therefore, 18 keV may not be the optimal energy and its true value may be located between 18 keV and 20 keV.

Regarding the calcification analysis, some changes in the optimal energy values between tasks with different photon interaction filter were obtained (see Table 6.8). For fatty breasts, 20 keV was the optimal energy to detect calcifications based on images free of scattered radiation. The same monochromatic energy was found to be the optimal energy to detect a calcification of 200 μm thick in denser breasts despite the type of radiation that is included in the images. For the rest of the tasks, the detectability of calcifications is improved when an energy of 18 keV is used.

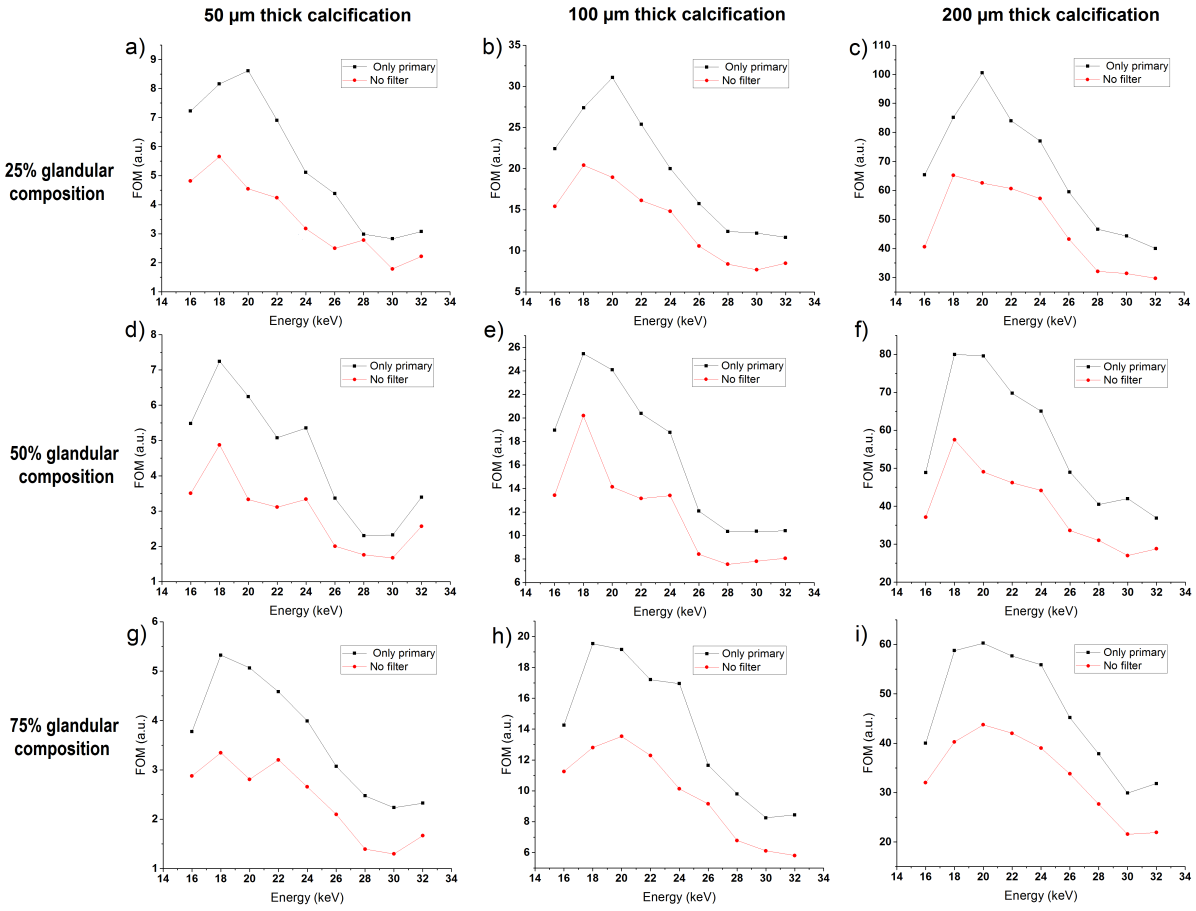

Figure 6.4: FOM results obtained by MC simulations for a 4 cm breast thick for different glandular compositions (25%, 50% and 75%) and sizes of the calcifications (50, 100 and 200 µm) and types of photon interaction filter.

Although the optimal quantum energy is the same, the curve of FOM for images with no photon interaction filter, (that show a similar behavior to those with only primary photons), has always smaller absolute FOM values. Furthermore, the same conclusions of the FOM analysis can be applied to both images with and without including the scattered radiation.

In Figure 6.3 and 6.4, it can be seen that the adipose-rich breast increases the FOM, this means that tumors and microcalcifications are easier to detect at the same dose load for the patient. The better detectability of lesions in a fatty breast (composed of 25% of glandular tissue) can be explained by the lower mass density (see Table 5.2) and the increased ratio of carbon to oxygen atoms, which increase the transmission of photons that consequently allows the usage of lower-energy photons [88].

In relation to tumor mass, the FOM values of the calcifications are much higher because calcifications have a higher density than tumors which density is very similar to the breast tissues (see Table 5.2), in this way, calcifications have greater contrast. Another important detail to be noticed is related to the size of the lesion, since, increasing the lesion thickness, an improvement of the lesion detectability is achieved due to the increasing size of the lesion itself.

6.6 Determination of signal loss

Considering the formalism presented in Section 5.9, the signal loss for both cases studied in Section 6.5 was assessed. As seen in Section 6.5, in general, the optimal energy that maximizes the FOM for images that includes both only primary and all radiation (primary+scatter) was the same. However, a decrease of the absolute value of FOM when scattered radiation is included was observed. In order to quantify the intensity signal that was lost due to scatter, the signal loss (SL) parameter was used. In Figure 6.5, the dependence of this parameter over the breast thickness is presented. In the center of the breast composed of 50% glandular tissue, a 5 mm thick tumor mass was placed.

Concerning the results in Figure 6.5, an increase of signal degradation with the increase of breast thickness, almost in an exponential way, is observed. For breast thickness of 2, 4, 6 and 8 cm the correspondent value of SL was 3.49%, 10.51%, 53.96% and 81.62%, respectively. Breast thickness is one of the most important causes that contributed to

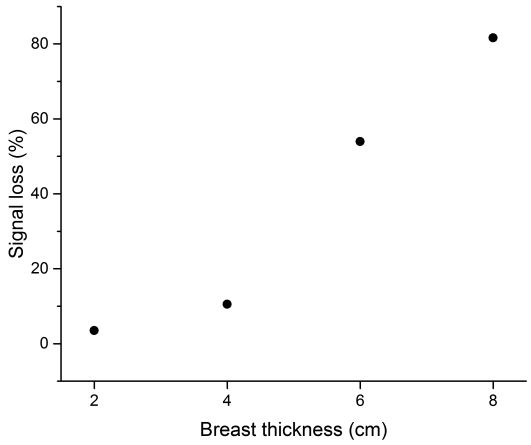

Figure 6.5: Signal loss due to scattered radiation as function of breast thickness. The 4 cm thick breast has a tumor mass of 5 mm thick on its center.

increasing the scatter signal within the image receptor [47,48,94–96] which can explain the greater signal loss found for a breast of 8 cm thick. Between the maximum and minimum thicknesses, the scattered radiation contributed to an increase of signal degradation of approximately 78%.

In terms of the signal loss as a function of breast composition for tumors and calcifications of variable sizes, the results are presented in Table 6.9. Relative to calcifications, its fraction of signal loss is always bigger than for tumors, independently of breast composition. On the other hand, for each lesion and thickness, the lowest degradation of the signal intensity was for a breast composed of 50% of glandular tissue.

6.7 Determination of SPRs

In Table 6.10, the results of SPR as a function of projection angle, breast composition, lesion sizes and position of measurement for a 4 cm thick breast are shown. In first reason, for each glandular composition and for each projection angle, the size of the lesions (both tumor and microcalcification) seems to be independent of the SPR, since in the ROI 2 (which includes the lesion plus near background) the values of SPR are almost identical.

It is important to point out that each ROI (considering the two lesions and their sizes) has a similar SPR value for each projection and for each glandular composition, except for the two largest calcifications in a breast consisting of 75% of glandular tissue whose values were slightly inferiors. This fact can be explained since the initial parameters

Table 6.9: Signal loss due to scattered radiation for different breast compositions and lesion sizes. The breast has a 4 cm of thickness. Note: T – tumor mass and M – microcalcification.

Glandular composition	Lesion and thickness	FOM_{max}		SL (%)
		Only primary	Primary+scatter	
25%	T. 3 mm	1.12	0.97	12.72
	T. 5 mm	3.13	2.64	15.78
	T. 10 mm	12.07	10.48	13.19
	M. 50 μm	8.62	5.66	34.37
	M. 100 μm	31.07	20.40	34.35
	M. 200 μm	100.53	65.20	34.15
50%	T. 3 mm	0.38	0.35	7.89
	T. 5 mm	1.19	1.04	12.61
	T. 10 mm	4.70	4.30	8.51
	M. 50 μm	7.25	4.88	32.69
	M. 100 μm	25.47	20.19	20.72
	M. 200 μm	79.98	57.51	28.09
75%	T. 3 mm	0.11	0.08	22.54
	T. 5 mm	0.29	0.21	26.87
	T. 10 mm	1.09	0.91	16.30
	M. 50 μm	5.32	3.35	37.17
	M. 100 μm	19.54	13.53	30.76
	M. 200 μm	60.25	43.72	27.43

(breast thickness and optimal x-ray energy of 18 keV) used for the MC simulations were the same, except for those calcifications in a glandular-rich breast whose optimal X-ray energy was 20 keV (see Table 6.8).

Taking this into consideration, an average of the SPR results was done (only for those whose optimal energy was 18 keV) in order to obtain two representative graphics of the dependence of scatter on breast composition (Figure 6.6a) and projection angle (Figure 6.6b).

The uncertainties associated with the values of SPR are related to the standard deviation given by the Image J.

Table 6.10: SPR results in three ROIs as function of projection angle, lesion size and breast composition for a 4 cm thick breast.

Glandular composition	Lesion and thickness	Optimal energy (keV)	Projection angle (°)	SPR ROI 1 Chest wall	SPR ROI 2 Center	SPR ROI 3 Nipple Area
25%	T. 3 mm	18	0	0.411±0.057	0.477±0.032	0.426±0.046
			12	0.426±0.060	0.495±0.035	0.441±0.050
			24	0.476±0.069	0.555±0.043	0.494±0.059
	T. 5 mm	18	0	0.411±0.057	0.478±0.034	0.426±0.046
			12	0.426±0.060	0.497±0.037	0.441±0.050
			24	0.476±0.069	0.557±0.046	0.494±0.059
	T. 10 mm	18	0	0.411±0.057	0.481±0.040	0.426±0.046
			12	0.426±0.060	0.500±0.044	0.441±0.050
			24	0.476±0.069	0.560±0.054	0.494±0.059
	M. 50 μm	18	0	0.411±0.057	0.476±0.032	0.426±0.046
			12	0.426±0.060	0.494±0.035	0.441±0.050
			24	0.476±0.064	0.554±0.043	0.494±0.059
	M. 100 μm	18	0	0.411±0.057	0.476±0.035	0.426±0.046
			12	0.426±0.060	0.495±0.038	0.441±0.050
			24	0.476±0.069	0.555±0.047	0.494±0.059
	M. 200 μm	18	0	0.411±0.057	0.477±0.047	0.426±0.046
			12	0.426±0.060	0.496±0.051	0.441±0.050
			24	0.476±0.069	0.551±0.064	0.494±0.059
50%	T. 3 mm	18	0	0.423±0.058	0.487±0.036	0.440±0.051
			12	0.439±0.063	0.507±0.039	0.455±0.055
			24	0.492±0.073	0.570±0.048	0.512±0.066
	T. 5 mm	18	0	0.423±0.058	0.488±0.036	0.440±0.051
			12	0.439±0.063	0.508±0.040	0.455±0.055
			24	0.492±0.073	0.571±0.049	0.512±0.066
	T. 10 mm	18	0	0.423±0.058	0.490±0.039	0.440±0.051
			12	0.439±0.063	0.510±0.043	0.455±0.054
			24	0.492±0.073	0.573±0.053	0.512±0.066
	M. 50 μm	18	0	0.423±0.058	0.487±0.036	0.440±0.051
			12	0.439±0.063	0.506±0.040	0.455±0.055
			24	0.492±0.073	0.570±0.049	0.512±0.066

Table 6.10: SPR results in three ROIs as function of projection angle, lesion size and breast composition for a 4 cm thick breast.

Glandular composition	Lesion and thickness	Optimal energy (keV)	Projection angle (°)	SPR ROI 1 Chest wall	SPR ROI 2 Center	SPR ROI 3 Nipple Area
75%	M. 100 μm	18	0	0.423±0.058	0.487±0.038	0.440±0.051
			12	0.439±0.063	0.507±0.042	0.455±0.055
			24	0.500±0.112	0.579±0.103	0.520±0.110
	M. 200 μm	18	0	0.423±0.058	0.489±0.051	0.440±0.051
			12	0.439±0.063	0.507±0.042	0.455±0.055
			24	0.492±0.073	0.573±0.069	0.512±0.066
	T. 3 mm	18	0	0.436±0.061	0.498±0.040	0.455±0.056
			12	0.452±0.065	0.519±0.043	0.472±0.060
			24	0.509±0.076	0.586±0.054	0.534±0.076
	T. 5 mm	18	0	0.436±0.061	0.499±0.040	0.455±0.057
			12	0.452±0.065	0.520±0.043	0.472±0.060
			24	0.509±0.077	0.586±0.054	0.534±0.076
	T. 10 mm	18	0	0.436±0.061	0.499±0.041	0.455±0.057
			12	0.452±0.065	0.521±0.044	0.472±0.060
			24	0.509±0.076	0.587±0.056	0.534±0.076
	M. 50 μm	18	0	0.436±0.061	0.498±0.040	0.455±0.056
			12	0.452±0.065	0.519±0.043	0.472±0.060
			24	0.509±0.076	0.586±0.054	0.534±0.076
	M. 100 μm	20	0	0.428±0.059	0.500±0.031	0.445±0.051
			12	0.442±0.061	0.517±0.033	0.459±0.019
			24	0.492±0.070	0.579±0.040	0.512±0.067
	M. 200 μm	20	0	0.428±0.058	0.501±0.039	0.445±0.051
			12	0.442±0.061	0.518±0.041	0.453±0.054
			24	0.492±0.070	0.580±0.050	0.512±0.067

The SPR is not a constant value for different breast thicknesses, however, for the same thickness, the SPR oscillates significantly over the area of the breast. This effect can be seen in both graphics presented in Figure 6.6. The SPR takes its higher value

at the center of the breast, independently from the breast composition and projection angle considered. Besides, the SPR is higher near the area of the nipple than near to the chest wall. These results are consistent with those published in the literature which describes the same behavior of scattered radiation by the analysis of SPR profiles and scatter spatial distribution [47, 48].

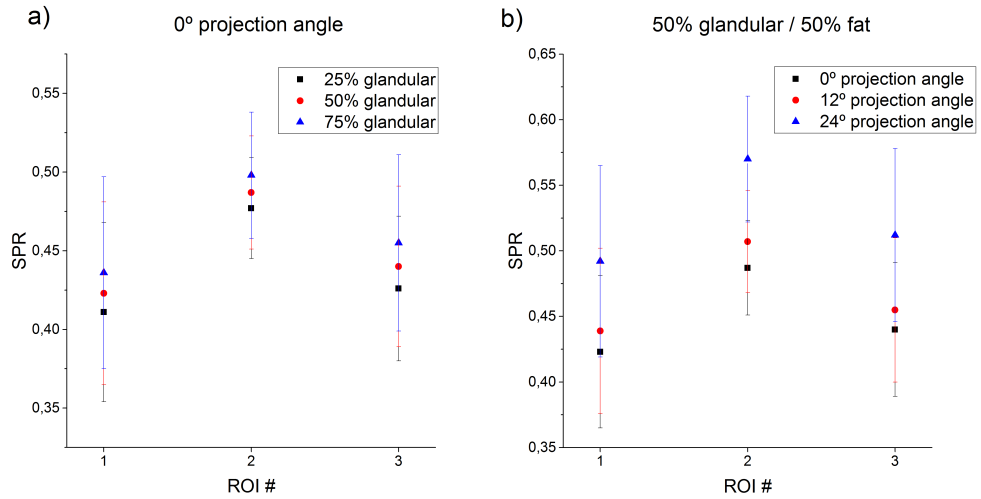

Figure 6.6: SPR results for a 4 cm thick breast as a function of position of measurement and a) breast composition considering a projection angle of 0°, and b) projection angle considering a breast composed of 50% of glandular and adipose tissue.

According to Figure 6.6a, the magnitude of scattered radiation on breast compositions of 25%, 50% and 75% ranged between 0.411±0.057 and 0.498±0.040 for the projection angle of 0°. In addition, increasing the glandular composition of the breast, the SPR values can rise by up to 4% in each ROI. On the other hand, the increase in SPR throughout the breast with increasing projection angle can be seen in Figure 6.6. This effect can be explained due to the fact that with the increase of the projection angle, the distance travelled inside the breast by the X-rays increases by a factor of $\frac{1}{cos\phi}$ [43, 97], where ϕ is the projection angle.

6.8 Scatter dependence on W/Rh X-ray energy spectrum

As shown in Figure 6.7, the values of SPR tend to slowly decrease when the peak voltage of the W/Rh X-ray spectrum increases. Although other filter/anode combinations (such as the Mo/Mo, Rh/Rh, Mo/Rh or W/A) causes little or no variations on the SPR

according to the literature [47, 48, 94–96, 98, 99], the discrepancy in SPR between the 22 kVp and 42 kVp was equal to 17% for a W/Rh spectrum which is not an negligible value, especially, for breast imaging techniques that uses different peak tube voltages. For example, for DBT examinations, the peak tube voltage is usually in the range of 24 kVp to 32 kVp, therefore, the SPR for a 4 cm thick breast is between the values of 0.47 and 0.51, while, for a breast computed tomography (CT) which uses peak voltages higher than 40 kVp [132], the SPR values are going to be lower than 0.45. Namely, in the perspective to use breast CT clinically, the use of higher voltages with the W/Rh anode/filter combination, could be beneficial, because the SPR seems to be lower with respect to a lower voltage usually used in mammography or DBT.

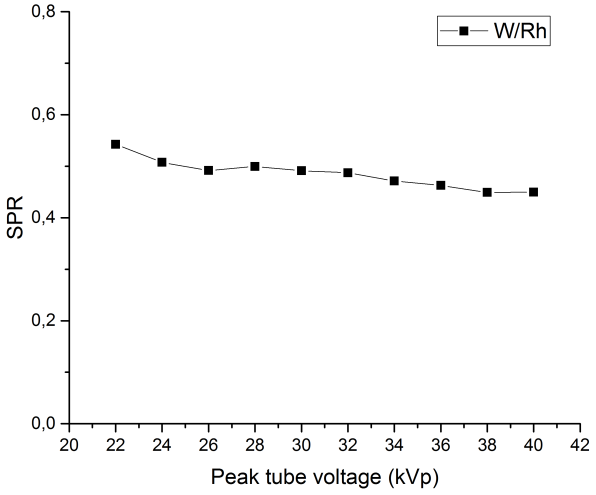

Figure 6.7: SPR as a function of W/Rh X-ray spectrum.

6.9 Pixel-by-pixel X-ray energy spectrum analysis

The entrance X-ray spectrum, together with the primary, Compton and Rayleigh photons that reach into the detector for projection angles of 0°, 12° and 24°, are shown in Figures 6.8, 6.9 and 6.10, respectively. In those figures, for each projection angle, the pulse height spectrum (PHS) (for each contributions above) was calculated in two different positions as described in Section 5.12.

According to the results, no significant changes in the energy distribution curve of primary, Compton and Rayleigh with the increase of projection angle and position of measurements is observed, except for the projection angle of 24° in pixels inside the

breast (Figure 6.10a), where the PHS for Compton photons is narrowed in comparison with the other Compton PHS.

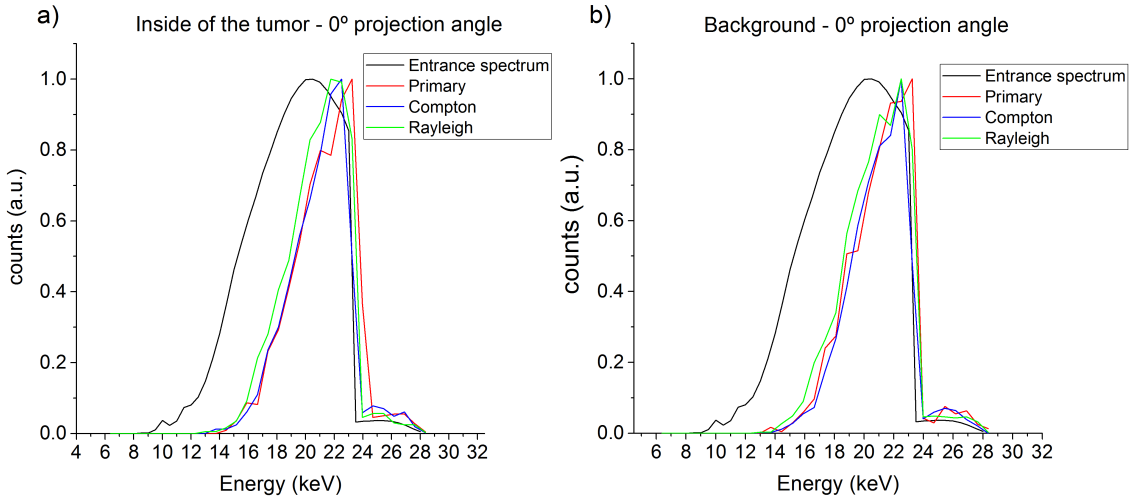

Figure 6.8: X-ray spectra simulations for each photon interactions (Compton and Rayleigh) and primary photons that are detected considering a projection angle of 0°. The spectra were determined in the pixels inside the tumor (a) and in the background near the lesion (b). For comparison, also the entrance X-ray spectrum is showed.

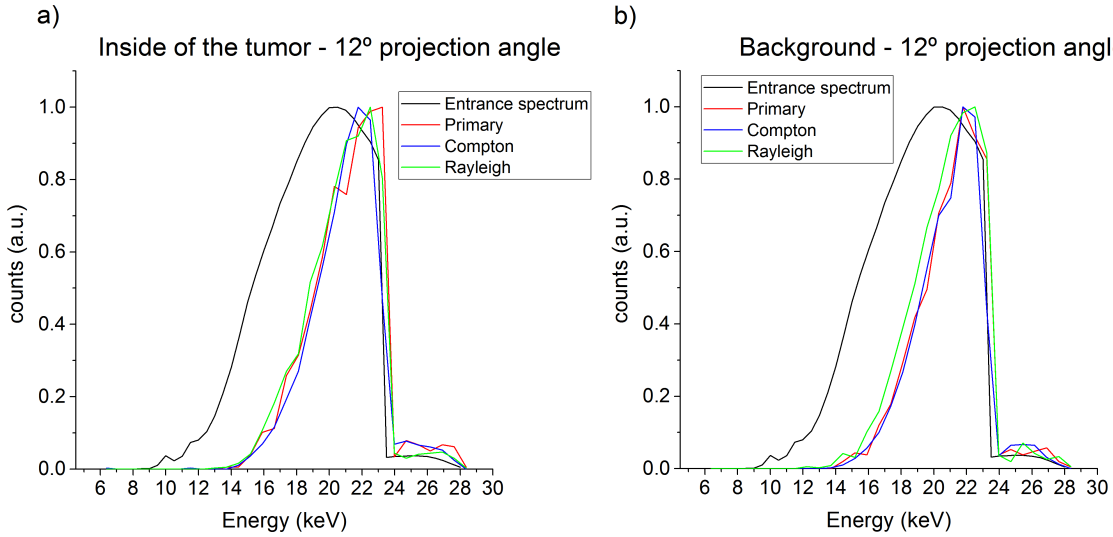

Figure 6.9: X-ray spectra simulations for each photon interactions (Compton and Rayleigh) and primary photons that are detected considering a projection angle of 12°. The spectra were determined in the pixels inside the tumor (a) and in the background near the lesion (b). For comparison, also the entrance X-ray spectrum is showed.

The main difference in these results relies on the spectrum mean energy values in comparison with the mean energy of the entrance spectrum (18.97 keV). In fact, the average energy values of primary, Compton and Rayleigh photons suffer a shift to 21.15 keV, 21.04 keV and 20.85 keV, respectively (beam hardening).

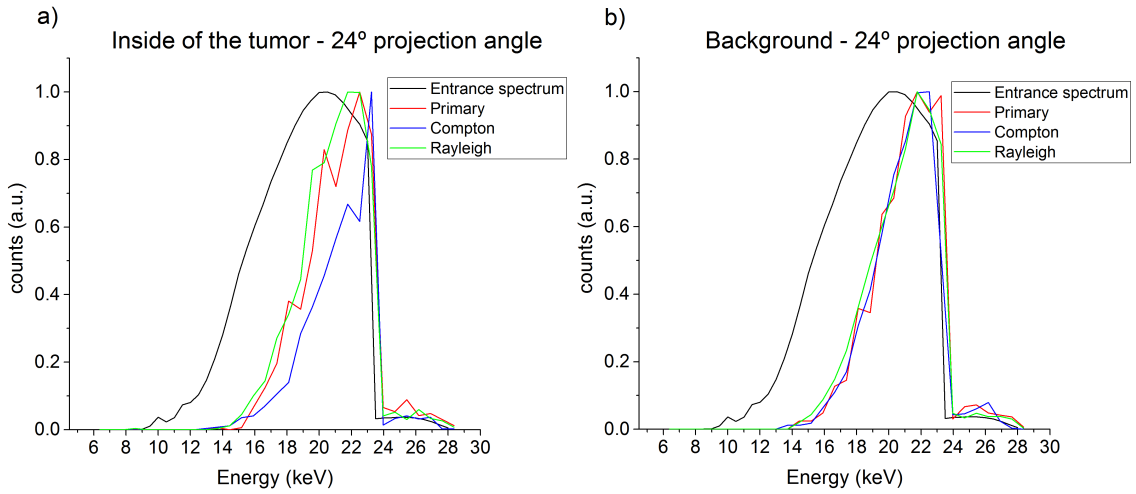

Figure 6.10: X-ray spectra simulations for each photon interactions (Compton and Rayleigh) and primary photons that are detected considering a projection angle of 24°. The spectra were determined in the pixels inside the tumor (a) and in the background near the lesion (b). For comparison, also the entrance X-ray spectrum is showed.

For each simulation considering only primary photons, 1×10^9 histories were run and for the rest of the MC simulations, 1×10^{10} histories were considered. The uncertainty of MC simulations is approximately 15% based on the uncertainty associated to the spectral data (15%) and the statistical uncertainty of the imaging tally (1%).

Regarding the SPR calculations using the formalism described in Section 5.12, another approach to determine the SPR for the same setup was used for comparison purposes. In this other approach, SPR maps are created and the values inside the lesion and in the background near the lesion are determined by using a circular ROI (see Figure 6.11). Therefore, in the imaging tally of PenEasy, the detection mode was changed to the energy integrating mode and, for each projection angle (0°, 12°, 24°), two separate images were obtained: a primary-only image and an image with all the radiation that reaches the detector. The method to create the SPR maps is described in Section 5.10.

In Table 6.11, the SPR results from both methods are presented. In order to differentiate the two methods, the SPR result using the total counts of each PSH (primary, Compton and Rayleigh) is going to be named as $SPR_{spectrum}$ and the SPR result using the SPR maps is going to be named as SPR_{ROI}.

As showed in the Table 6.11, in both methods, the SPR inside the breast is always higher than background and, in general, both increased their SPR values with the increase of projection angle. Also, as showed in the last column of Table 6.11, the SPR results obtained by the spectrum analysis are underestimated with a discrepancy of about 30%

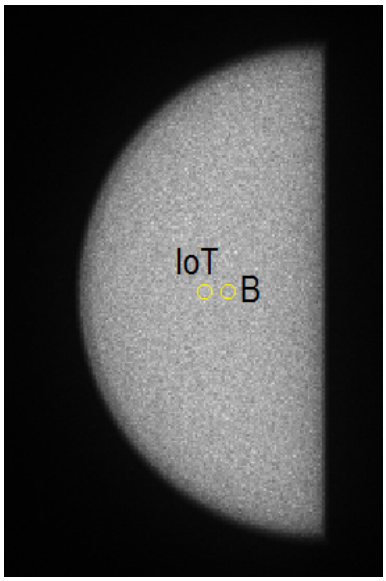

Figure 6.11: An example of a SPR map used for the determination of SPR inside the tumor and in the background using a circular ROI. This SPR image was obtained for the 0° projection.

Table 6.11: SPR results for each projection angle and position of measurement using two different methods.

Position of measurement	Projection angle (°)	$SPR_{spectrum}$	SPR_{ROI}	Relative difference (%)
Inside of tumor (IoT)	0°	0.361	0.514	29.80%
Background (B)		0.339	0.480	29.44%
IoT	12°	0.394	0.520	24.29%
B		0.331	0.513	35.50%
IoT	24°	0.405	0.556	27.22%
B		0.378	0.523	27.81%

compared with the SPR results using SPR maps. However, for each angular projection, the average of the SPR_{ROI} values between the SPR inside and out of the lesion are consistent with the values obtained in Section 6.7 for a breast composed of 50% of glandular tissue considering the ROI number 2.

$$Relative.Difference(\%) = \frac{SPR_{ROI} - SPRspectrum}{SPR_{ROI}} \times 100\% \tag{6.2}$$

It is important to mention that, in the SPR_{ROI} approach all the radiation that reaches the detector is considered, which means that secondary photons and photons that suffer more than two interactions are also being considered. Therefore, the presence of such

Table 6.12: SPR results after the second attempt to determine the SPR using the SPR maps approach.

Position of measurement	Projection angle (°)	$SPR_{spectrum}$	SPR_{ROI}	Relative difference (%)
Inside of tumor (IoT)	0°	0.361	0.362	0.32%
Background (B)		0.339	0.346	2.12%
IoT	12°	0.394	0.360	-9.36%
B		0.331	0.368	10.09%
IoT	24°	0.405	0.390	-3.75%
B		0.378	0.362	-4.29%

photons can be the cause of the great discrepancy between values of SPR. Thus, in order to test this hypothesis, another calculation of the scatter fraction by using the SPR maps was performed. In this case, three separate images were created: (1) an image with only-primary radiation, (2) an image with photons that suffered one Compton interaction until reaching the detector and (3) an image with photons that suffered one Rayleigh interaction. Through the Image J program, Compton and Rayleigh images were summed to obtain only one scatter image. Then, this scatter image (with only Compton and Rayleigh contributions) was used to obtain a SPR map. The results are shown in Table 6.12.

As it can be seen, the values of SPR calculated by the two methods are now in agreement with a maximum difference below 10%, which means that the secondary and multiscatter photons have an influence of about 30% of the total SPR value. Even if there in literature there is some attempt to try to model the scatter in mammography by simulating single-scatter events [133], this approximation could be only valid in thin breasts. The multi scatter events modeling, as shown in the results of this study, could be of paramount of importance in scatter map estimations, since its contributions could reach values of about 30%. Moreover, has showed in Table 6.11, the scatter fraction seems to slightly increase with the increasing projection angle. For this reason, exact scatter estimation is still more crucial when 3D acquisitions modes (that also do not make use of anti-scatter grids), as DBT, are considered.

Furthermore, a scatter profile from the nipple area to the chest wall was performed for each projection angle of 0°, 12° and 24° and for each SPR map used for the determination of the values of SPR_{ROI} in the first (SPR-ROI1) and second attempt (SPR-ROI2). The

results are shown in Figure 6.12.

As it can be seen, the maximum values of SPR are in the center of the breast which tends to decrease towards the breast edges. Despite the evident differences on scatter profiles between the SPR images with and without multiscatter and secondary photons, the behavior of scattered radiation over the breast area shows a great similarity.

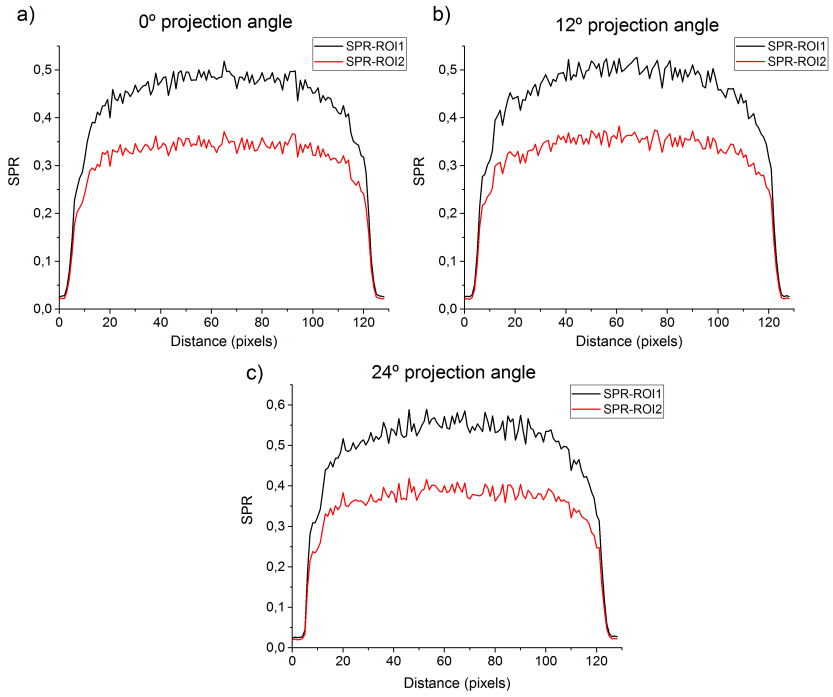

Figure 6.12: Scatter profiles to the nipple area of the breast to the chest wall considering the two SPR maps used for the scatter fraction determination for projection angles of: (a) 0°, (b) 12° and (c) 24°.

6.10 Evaluation of the subtraction-based method for scatter reduction

The method for scatter reduction was applied in three projection images at 0°, 12° and 24° of a complete DBT examination performed by a Siemens Mammomat Inspiration system. The results of SDNR, before and after the application of the method, are shown in Table 6.13.

Taking the results into consideration, the subtraction-based method, used in this work, has improved the image quality of the projection image by increasing the detectability of the calcification of 300 μm thick and of the tumor of 3.2 mm thick. Relative to calcifica-

Table 6.13: SDNR results after and before the application of the subtraction-based method for scatter reduction.

Lesion	Projection angle (°)	Pixel-by-pixel subtraction	SDNR
Calcification	0°	Before	4.340
		After	4.507
	12°	Before	3.834
		After	7.291
	24°	Before	4.348
		After	5.897
Tumor	0°	Before	0.621
		After	1.385
	12°	Before	0.750
		After	2.067
	24°	Before	0.576
		After	1.665

tions, overall, higher SDNR values than those of tumors are observed, since, calcifications are denser materials than tumors and therefore, have greater contrast. Furthermore, since tumors have a similar density to that of breast tissues, their localization inside the breast is always more complicated, even if, the position of tumors inside the MTM 100 phantom is known.

In Figure 6.13 and 6.14, images before and after undergoing through the scatter reduction method for calcification and tumor for the projection angle of 0°, 12° and 24° are shown, respectively. The calcification in the corrected image (Figure 6.13) can be easily detected. On the other hand, although the SDNR increases after the application of this scatter reduction method, the visualization of the tumor mass (Figure 6.14) in the corrected image is still quite difficult.

The methodology of this scatter reduction approach is based in a subtraction pixel-by-pixel of the scatter component from the projection image applied in a local way. This method is easy to implement and it may be an auxiliary tool for doctors, radiologists and other breast imaging technicians to improve the detectability of suspicious lesions, especially for calcifications, in order to correctly identify them. However, the MC images with reasonable statistic took several days to be generated, which can be a great limitation to the applicability of this method to clinical practice.

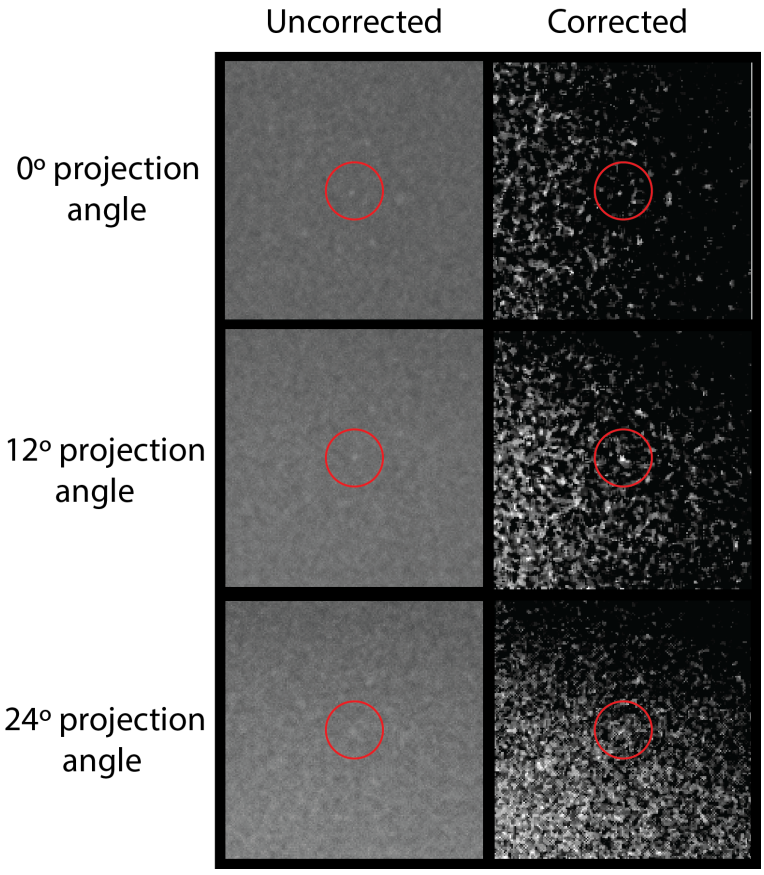

Figure 6.13: Visual result before and after the application of the subtraction-based method for scatter reduction for the projection image at 0°, 12° and 24°. In this case a calcification of 300 μm thick can be seen at the center of the ROI.

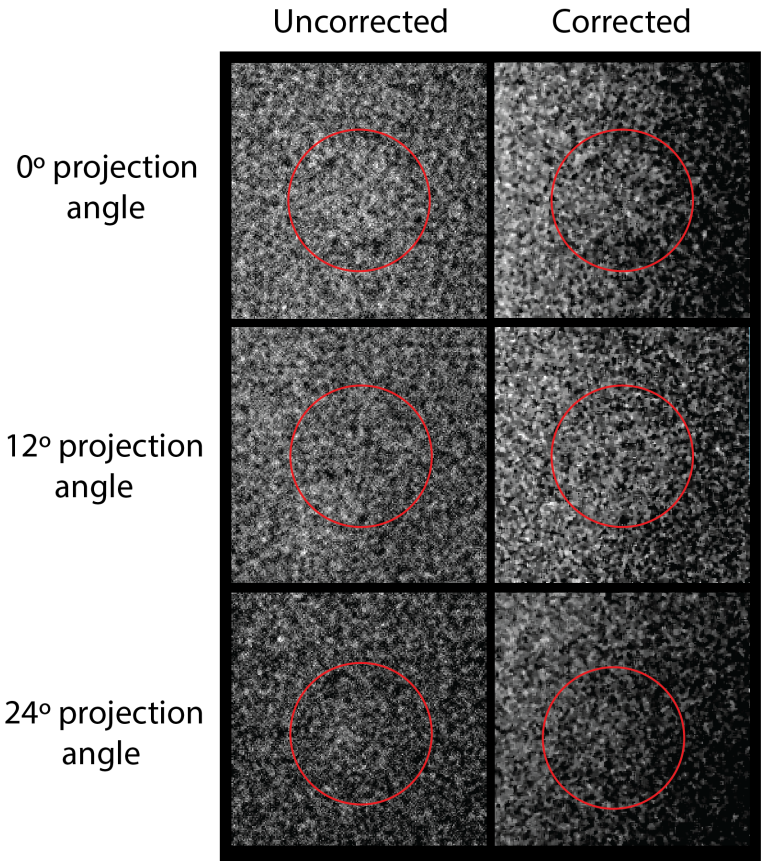

Figure 6.14: Visual result before and after the application of the subtraction-based method for scatter reduction for the projection image at 0°, 12° and 24°. In this case a calcification of 3.2 mm thick can be seen at the center of the ROI.

Chapter 7

Conclusions and Future work

The aim of this work was to study the influence of scatter on image quality optimization and dose in DBT examinations. In this thesis, four relevant areas have been studied: a dosimetric study, an image quality optimization using a figure-of-merit (FOM), a study of the X-ray scatter behavior in DBT projections through the determination of scatter-to-primary ratio (SPR) and, at last, the development and application of a subtraction-based method for scatter reduction.

Firstly using PENELOPE code, the implemented MC model of a DBT image acquisition system (Siemens Mammomat Inspiration at operation in the Instituto Português de Oncologia de Lisboa Francisco Gentil) was successfully validated against experimental measurements with a maximum discrepancy of 10.96% and 13.65% in the ESD and Kair results, respectively. Although these values may seem high, at the level of the uncertainty associated with the simulations (15%) the MC model was considered validated.

In the first part of this study, a dosimetric characterization was performed in which the backscatter factors and mean glandular dose (MGD) were calculated for experimental and simulated data and, also, the influence of the compression plate on dose was assessed. The backscatter factors were calculated for PMMA thicknesses of 20, 40, 60 and 70 mm. The simulated BSF values ranged between 1.076±0.161 and 1.123±0.168 and an agreement was found with the published data by the European protocol on dosimetry in mammography, where BSF are tabulated for HVL between 0.25 and 0.65 mmAl and ranged from 1.07 to 1.13, while in the absence of HVL information, the BSF is considered to be 1.09. On the other hand, an underestimation of about 8% of the measured BSF against the simulated results was observed. This can be explained due to the fact that

the ionization chamber has a weak angular response when used for DBT measurements and in addition its calibration was performed for the tube voltage of 28 kVp and 0° projection. Considering the MGD estimation, for PMMA thicknesses from 20 to 70 mm, the measured MGD range between 0.825±0.115 mGy and 2.314±0.324 mGy, while the simulated MGD varied from 0.712±0.107 mGy to 2.369±0.355 mGy. Concerning those results, both measured and simulated MGD are below the reference value defined by the European protocol [87] of each PMMA thickness of 20, 40, 60 and 70 mm, which are: 1.0, 2.0, 4.5 and 6.5 mGy, respectively. This conclusion is important for the future of DBT as a technique used for breast screening. Finally, considering the dosimetric characterization of the clinical DBT system, it was found that the compression plate also has an important role in reducing the absorbed dose delivered to the breast. In fact, according to the results of this work, its presence could lead to a dose saving of almost 20%.

The dosimetric characterization of the clinical DBT equipment was an important step of this work, because the exact knowledge of the doses involved in these important screening techniques such as mammography, help to increase the awareness between patients and medical staff from the radiological protection point of view.

In the second part of this work, the optimization of DBT image quality has been studied for two different cases: influence of breast thickness and breast composition. In both cases, the inclusion of scattered radiation on MC simulations revealed that the optimal energy which maximizes the FOM does not change its values, however, the absolute value of FOM decreases.

In particular it was realized that thicker breasts required the use of higher energies in order to achieve a better image quality. The optimal energy increased about 33% between the breast of 2 cm thick (16 keV) and the breast of 8 cm thick (24 keV). Furthermore, the FOM values became smaller when the breast thickness increases, which mean, that increasing breast thickness caused a deterioration of the lesion detectability. Additionally, breast thickness is one of the most important causes that contributed to the increasing of the scatter component in the total signal of the detector. Namely a signal degradation of about 78% between the maximum and minimum thicknesses due to the presence of scattered radiation was found.

In order to assess the detectability of lesions, two types of lesions (tumor mass and calcification) were also evaluated for the image quality optimization study with different

breast compositions. Relative to the detection of tumors and calcifications, a monochromatic energy of 18 keV was found to be the optimal energy for most of the tasks studied. According to the published literature, the optimal energy should slightly increase 4-6% [88,92] for denser breasts, however, since 2 keV steps between monoenergetic energies were considered, those increasing factors are small to be noticed. Therefore, the true value of the optimal energy for both tumors and calcifications for each breast composition can be located between 18 keV and 20 keV.

For fatty breasts (lower glandular composition), an increment of the FOM values was observed, which means that both lesions are easier to detect, independently of their sizes, at the same dose load for a given patient. For each lesion and thickness, the lowest degradation of the signal intensity it was found for a breast composed of 50% of glandular tissue. Furthermore, an enhanced detectability of a lesion was observed when the lesion size increases. On the other hand, in relation to the tumor mass, the FOM values of the calcifications are much higher because calcifications have a higher density which contributed for having greater contrast. However, the fraction of signal loss is always bigger for calcifications than for tumor, independently of breast composition.

The third part of this thesis was dedicated to the characterization of the scattered radiation as a function of several parameters, such as: breast composition, projection angle, position of measurements, W/Rh X-ray energy spectrum at different tube voltages and type of lesions and their dimensions.

The study of the scatter was mainly performed in terms of SPR. The SPR seems to not have a significant influence when the type of lesion (tumor mass and calcification) and its dimensions are considered. However, the SPR was always higher inside the lesion with respect to its surrounding zones (background), and both values tend to rise for an increased projection angle. A variation of SPR over the area of the breast was observed. While SPR takes its higher value at the center of the breast, towards the breast edges, the value of SPR decreases. Furthermore, an insight was obtained of the behavior of scatter with varying projection angle and it was found that for the 24° projection angle, the SPR can rise by up to about 14% with respect to the of 0° projection one. Moreover, for the projection angle of 0°, the increase of glandular fraction inside the breast led to an increase of approximately 4% in the SPR values in each ROI considered.

The DBT system used in this work only operates with a W/Rh as the anode/filter com-

bination, however, it was not found in the literature any study that evaluates the scatter dependence on an X-ray spectrum with such combination. Although, other anode/filter combinations revealed to have a little influence on the scatter fraction [47,48,94–96,98,99], the discrepancy in SPR between 22 kVp and 42 kVp was found to be equal to 17% for a W/Rh spectrum. This value is not negligible, since, two breast imaging techniques (DBT and breast computed tomography (CT)) that operates at different ranges of tube voltages can have distinct SPR intervals. Namely, through this study, it is possible to affirm that the eventual use of breast CT as diagnostic tools could be beneficial in terms of a reduced SPR in the acquired images, if higher voltages will be used.

Furthermore for each projection angle (0°, 12° and 24°), a pulse height spectrum (PHS) of primary, Compton and Rayleigh photons that reach into the detector were obtained. In the analysis of each PHS for pixels inside the lesion and in the background, no significant change in the energy distribution curve was observed for each projection angle. Due to the beam hardening, the mean energy of primary, Compton and Rayleigh photons suffered a shift to 21.5 keV, 21.04 keV and 20.85 keV, respectively, in comparison with the mean energy of the entrance X-ray spectrum (18.97 keV). Given the simulations capabilities of the MC code used, a detailed simulations of the different physics interaction in the mammography diagnostic energy range was performed. Through the discrimination of five interaction modes (primary, Compton, Rayleigh, secondary and multiscatter), it was found that the secondary and multiscatter photons have a great influence for the determination of SPR which could be of paramount of importance in scatter map estimations, since its contributions could reach values of about 30%.

Finally, a subtraction-based method was developed in order to attempt to reduce the scatter component from three DBT projection images that were acquired from a Siemens Mammomat Inspiration system. This method operates in a local way, which means that the localization of the lesion and its size has to be prior information for the scatter estimation. A SDNR analysis was performed in order to evaluate the performance of this method. After the application of the method in the projection images, the detectability of the calcification of 300 µm thick and of the tumor of 3.2 mm thick increased, nevertheless, relative to the calcification, higher SDNR values than those of tumors are observed. After the application of the method, the calcification in the corrected image can be easily detected, however, the visualization of the tumor mass is still very complicated, since, the

tumor have a similar density with breast tissues. This methodology for scatter reduction is easy to implement and it may help breast imaging technicians to properly identify suspicious lesions, especially calcifications, in a certain region of the breast. Nevertheless, the MC images required for the scatter estimation took several days to be generated, which can be the major limitation in the perspective of using such method clinically. Also, the implementation of local scatter maps in order to reduce the scatter component in clinical images for each 2D projection (the number of projections depends on the type of system considered, i.e. Siemens, Hologic), could be of paramount importance in trying to improve a relatively new technique (2D synthetic mammography) which main aim is to produce 2D images, like the standard MLO and CC mammography ones, starting from the 2D projections acquired in a DBT exam (with a consequent dose saving for the patient).

7.1 Future work

The perspectives of the future work are mainly focused on the following aspects:

(i) While this study focused on the influence of scattered radiation on image quality optimization and dose considering a Siemens Mammomat Inspiration, a similar study in other commercial DBT systems, for instance the Hologic Selenia Dimensions will be performed.

(ii) The scatter reduction method through MC scatter maps will be applied in all the 2D projections of a complete DBT acquisition and the algorithms for obtaining 2D synthetic mammography images will be tested after scatter correction.

(iii) With respect to the scatter reduction method applied in this work, it would be interesting to extend this to a wider range of tube voltages, since, for a 28 kVp X-ray spectrum the visualization of the tumor mass of 3.2 mm thick was very poor.

(iv) Finally, in order to reduce the computational time needed to estimate the scatter field, a local-lesion simulation method will be tested. That is, instead to simulate the entire breast phantom, only the part that includes the tumor/calcification lesion will be simulated. In this way, a significant computational time reduction with comparable imaging performances (with respect to the simulation of the entire breast scatter map) is envisaged.

Bibliography

[1] PORDATA. Óbitos por algumas causas de morte (%) em portugal. http://www.pordata.pt/Portugal/%C3%93bitos+por+algumas+causas+de+morte+(percentagem)-758, 2014. Accessed: 1 June 2016.

[2] Liga Portuguesa Contra o Cancro. Cancro da mama. https://www.ligacontracancro.pt/cancro-da-mama/. Accessed: 1 June 2016.

[3] World Health Organization. Cancer country profiles 2014. http://www.who.int/cancer/country-profiles/en/, 2014. Accessed: 1 June 2016.

[4] I. S. Fentiman, A. Fourquet and G. N. Hortobagyi. Male breast cancer. *Lancet*, 367:595–604, 2006.

[5] World Cancer Research Fund International. Breast cancer statistics. http://www.wcrf.org/int/cancer-facts-figures/data-specific-cancers/breast-cancer-statistics, 2012. Accessed: 1 June 2016.

[6] World Cancer Research Fund – Continuous Update Project Keeping the science current. Breast cancer 2010 report food, nutrition, physical activity and the prevention of breast cancer.

[7] World Health Organization. The global burden of disease: 2004 update, 2008.

[8] World Health Organization. Breast cancer. estimated incidence, mortality and prevalence worldwide in 2012. http://globocan.iarc.fr/old/FactSheets/cancers/breast-new.asp, 2012. Accessed: 1 June 2016.

[9] R. H. Gold, L. W. Basset and B. E. Widoff. Radiology history exhibit. *RadioGraphics*, 10:1111–1131, 1990.

[10] J. Kalaf. Mammography: a history of success and scientific enthusiasm. *Radiol. Bras.*, 47(4):VII–VIII, 2014.

[11] B. N. Joe and E. A. Sickles. The evolution of breast imaging: past and future. *Radiology*, 273:S23–S44, 2014.

[12] American College of Radiology. Acr bi-rads atlas. `http://www.acr.org/Quality-Safety/Resources/BIRADS`, 2013. Accessed: 8 June 2016.

[13] H. Koch and M. V. Koch e Castro. Quality of the interpretation of diagnostic mammographic images. *Radiol. Bras.*, 43(2):97–101, 2010.

[14] S. Orel, N. Kay, C. Reynolds and D. Sullivan. Bi-rads categorization as a predictor of malignancy. *Radiology*, 211:845–850, 1999.

[15] S. Obenauer, S. Luftner-Nagel, D. von Heyden, U. Munzel, F. Baum and E. Grabbe. Screen film vs full-field digital mammography: image quality, detectability and characterization of lesions. *Eur Radiol*, 12:1697–1702, 2002.

[16] P. Skaane and A. Skjennald. Screen-film mammography versus full-field digital mammography with soft-copy reading: randomized trial in a population-based screening program – the oslo ii study. *Radiology*, 232:197–204, 2004.

[17] A. M. Chiarelli, M. V. Prummel, D. Muradali, R. S. Shumak, V. Majpruz, P. Brown, H. Jiang, S. J. Done and M. J. Yaffe. Digital versus screen-film mammography: impact of mammography density and hormone therapy on breast cancer detection. *Breast Cancer Res Treat*, 154:377–387, 2015.

[18] L. Tabar, G. Fagerberg, Hsiu-Hsi Chen, S. Duffy, C. Smart, A. Gad and R. Smith. Efficacy of breast cancer screening by age. *Cancer*, 75:2507–2517, 1995.

[19] Independent UK Panel on Breast Cancer Screening. The benefits and harms of breast cancer screening: an independent review. *Lancet*, 380:1778–86, 2012.

[20] R. de Gelder, J. Fracheboud, E. Heijnsdijk, G. den Heeten, A. Verbeek, M. Broeders, G. Draisma and H. de Koning. Digital mammography screening: weighing reduced mortality against increased overdiagnosis. *Preventive Medicine*, 53:134–140, 2011.

[21] L. Nyström, L. Rutqvist, S. Wall, A. Lindren, M. Lindqvist, S. Rydén, I. Andersson, N. Bjurstam, G.Fagerberg, J. Frisell, L. Tabár and L. Larsson. Breast cancer screening with mammography: overview of swedish randomized trials. *Lancet*, 341:973–978, 1993.

[22] A. Miller, C. Wall, C. Baines, P. Sun, T. To and S. Narod. Twenty five year follow-up for breast cancer incidence and mortality of the canadian national breast screening study: randomized screening trial. *BMJ*, 348:348–366, 2014.

[23] P. C. Gotzsche and O. Olsen. Is screening for breast cancer with mammography justifiable? *Lancet*, 355:129–24, 2000.

[24] J. Elmore, M. Barton, V. Moceri, S. Polik, P. Arena and S. Fletcher. Ten-year risk of false positive screening mammograms and clinical breast examinations. *The New England Journal of Medicine*, 338:1089–1096, 1998.

[25] I. Gram, E. Lund and S. Slenker. Quality of life following a false positive mammogram. *Br. J. Cancer*, 62:1018–1022, 1990.

[26] C. Lerman, B. Trock, B. Rimer, C. Jepson, D. Brody and A. Boyce. Psychological side effects of breast cancer screening. *Health Psychol.*, 10(4):259–67, 1991.

[27] J. Dobbins and D. Godfrey. Digital x-ray tomosynthesis: current state of the art and clinical potential. *Phys. Med. Biol.*, 48:R65–R106, 2003.

[28] L. Niklason, B. Christian, L. Niklason, D. Kopans et al. Digital tomosynthesis in breast imaging. *Radiology*, 205:399–406, 1997.

[29] I. Sechopoulos. A review of breast tomosynthesis. part i. the image acquisition process. *Med. Phys.*, 40(1):014301–12, 2013.

[30] H. Machida, T. Yuhara, T. Mori, E. Ueno, Y. Moribe and J. Sabol. Optimizing parameters for flat-panel detector digital tomosynthesis. *RadioGraphics*, 30:549–562, 2010.

[31] J. Mainprize, X. Wang and M. Yaffe. The effect of lag on image quality for a digital breast tomosynthesis system. *Proc. of SPIE*, 7258:72580R–1, 2009.

[32] S. Feng and I. Sechopoulos. Clinical digital breast tomosynthesis system: Dosimetric characterization", radiology. *Radiology*, 263:35–42, 2012.

[33] M. Baptista, S. di Maria, S. Barros, C. Figueira, M. Sarmento, L. Orvalho and P. Vaz. Dosimetric characterization and organ dose assessment in digital breast tomosynthesis: Measurements and monte carlo simulations using voxel phantoms. *Medical Physics*, 42:3788–13, 2015.

[34] M. Alakhras, C. Mello-Thoms, R. Bourne, M. Rickard, J. Diffey and P. Brennan. Relationship between radiation dose and image quality in digital breast tomosynthesis. *Radiation Protection Dosimetry*, pages 1–10, 2016.

[35] R. Bouwman, R. van Engen, K. Young, G. den Heeten, M. Broeders, S. Schopphoven, C. Jeukens, W. Veldkamp and D. Dance. Average glandular dose in digital mammography and digital breast tomosynthesis: comparison of phantom and patient data. *Phys. Med. Biol.*, 60:7893–7907, 2015.

[36] T. Marques, A. Ribeiro, S. di Maria, A. Belchior, J. Cardoso, N. Matela, N. Oliveira, L. Janeiro, P. Almeida and P. Vaz. Effect of the glandular composition on digital breast composition tomosynthesis image quality and dose optimisation. *Radiation Protection Dosimetry*, pages 1–5, 2015.

[37] I. Sechopoulos. A review of breast tomosynthesis. part ii. image reconstruction, processing and analysis, and advanced applications. *Med. Phys.*, 40(1):014302–17, 2013.

[38] T. Wu, R. H. Moore, E. A. Rafferty and D. B. Kopans. A comparison of reconstruction algorithms for breast tomosynthesis. *Med. Phys.*, 31(9):2636–12, 2004.

[39] P. Rezentes, A. de Almeida and G. Barnes. Mammography grid performance. *Radiology*, 210:227–232, 1999.

[40] J. Zhou, B. Zhao and W. Zhao. A computer simulation platform for the optimization of a breast tomosynthesis system. *Medical Physics*, 34:1098–12, 2007.

[41] B. Liu, T. Wu, R. Moore and D. Kopans. Monte carlo simulation of x-ray scatter based on patient model from digital breast tomosynthesis. *Proc. SPIE*, 6142:61421N–61429N, 2006.

[42] L. Zhu, J. Wang and L. Xing. Noise suppression in scatter correction for cone-beam ct. *Med. Phys*, 36:741–752, 2009.

[43] G. Wu, J. Mainprize, J. Boone and M. Yaffe. Evaluation of scatter effects on image quality for breast tomosynthesis. *Med. Phys*, 36(10):4425–8, 2009.

[44] J. Boone, and V. Cooper III. Scatter/primary in mammography: Monte carlo validation. *Med. Phys.*, 27(8):1818–14, 2000.

[45] S. Feng and I. Sechopoulos. A software-based x-ray scatter correction method for breast tomosynthesis. *Med. Phys.*, 38(12):6643–11, 2011.

[46] M. Poletti, O. Gonçalves, I. Mazzaro and H. Schechter. Evaluation of the influence of scattering profiles on the resolution, scatter/primary ratio, and grid performance in mammography. *Radiation Physics and Chemistry*, 61:607–610, 2001.

[47] J. Boone, K. Lindfors, V. Cooper III and J. Seibert. Scatter/primary in mammography: Comprehensive results. *Med. Phys.*, 27(10):2408–9, 2000.

[48] I. Sechopoulos, S. Suryanarayanan, S. Vendantham, C. D'Orsi and A. Karellas. Scatter radiation in digital breast tomosynthesis of the breast. *Med. Phys.*, 32(2):564–13, 2007.

[49] O. Diaz, D. Dance, K. Young, P. Elangovan, P. Bakic and K. Wells. Estimation of scattered radiation in digital breast tomosynthesis. *Phys. Med. Biol*, 59:4375–4390, 2014.

[50] Canadian Cancer Society. Anatomy and physiology of the breast. `https://breast360.org/en/topics/2015/10/21/breast-anatomy/`. Accessed: 8 June 2016.

[51] N. F. Boyd, L. J. Martin, M. Bronskill, M. J. Yaffe, N. Duric and S. Minkin. Breast tissue composition and susceptibility to breast cancer. *J Natl Cancer Inst*, 102:1224–1237, 2010.

[52] American Cancer Society. Breast cancer facts and figures 2010-2012. Atlanta: American Cancer Society, Inc.

[53] Unidade Funcional de Patologia Mamária, Grupo Multidisciplinar da Patologia Mamária. Protocolo de diagnóstico, terapêutica e seguimento. Coimbra: bloom up, lda, 2012. pp. 8-9.

[54] P. Gordon and L. Goldenberg. Malignant breast masses detected only by ultrasound. *Cancer*, 76(4):626–630, 1995.

[55] T. M. Kolb, J. Lichy and J. H. Newhouse. Occult cancer in women with dense breasts: detection with screening us-diagnostic yield and tumor characteristics. *Radiology*, 207(1):191–199, 1998.

[56] M. Morrow, J. Waters and E. Morris. Mri for *Lancet*, 378:1804–11, 2011.

[57] P. C. Johns and M. J. Yaffe. X-ray characterization of normal and neoplastic breast tissues. *Phys. Med. Biol.*, 32(6):675–695, 1987.

[58] Direcção-Geral da Saúde. Direcção-geral da saúde. abordagem imagiológica da mama feminina. Norma nº 051/2011 de 27/12/2011.

[59] J. R. Cunningham and D. R. Dance. Diagnostic radiology physics: A handbook for teachers and students. International Atomic Energy Agency, Viena, 2013.

[60] Andrew P. Smith. Fundamentals of digital mammography: Physics, technology and pratical considerations. Hologic, Inc., R-BI-016 March 2005.

[61] P. A. Carney, D. L Miglioretti, B. C. Yankaskas, K. Kerlikowske, R. Rosenberg, C. M Rutter, B. M. Geller, L. A. Abraham, S. H. Taplin, M. Dignan, G. Cutter G and R. Ballard-Barbash. Individual and combined effects of age, breast density, and hormone replacement therapy use on the accuracy of screening mammography. *Ann Intern Med*, 138(3):168–175, 2003.

[62] C. H. van Gils, J. D. Otten, A. L. Verbeek, J. H. Hendriks and R. Holland. Effect of mammographic breast density on breast cancer screening performance: a study in nijmegen. *J Epidemiol Commun Health*, 52(4):267–271, 1998.

[63] R. Schulz-Wendtland, M. Fuchsjager, T. Wacker and K. P. Hermann. Digital mammography: An update. *European Journal of Radiology*, 27:258–265, 2009.

[64] D. G. Grant. Tomosynthesis: a three-dimensional radiographic imaging technique. *IEEE Trans Biomed Eng*, 19:20–28, 1972.

[65] J. A. Baker and J. Y. Lo. Breast tomosynthesis: State-of-the-art and review of the literature. *Acad Radiol*, 18:1298–1310, 2011.

[66] P. Skaane, A. I. Bandos, R. Gullien, E. B. Eben, U. Ekseth, U. Haakenaasen, M. Izadi, I. N. Jebsen, G. Jahr, M. Krager, L. T. Niklason, S. Hofvind and D. Gur. Comparision of digital mammography alone and digital mammography plus tomosynthesis in a population-based screening program. *Radiology*, 267(1):47–56, 2013.

[67] S. P. Poplack, T. D. Tosteson, C. A. Kogel and H. M. Nagy. Digital breast tomosynthesis: Initial experience in 98 women with abnormal digital screening mammography. *AJR*, 189:616–623, 2007.

[68] M. L. Zuley, A. I. Bandos, M. Ganott, J. H. Sumkin, A. E. Kelly, V. J. Catullo, G. Y.Rathfon, A. H. Lu and D. Gur. Digital breast tomosynthesis versus supplemental diagnostic mammographic views for evaluation of noncalcified breast lesions. *Radiology*, 266(1):89–95, 2013.

[69] D. Förnvik, S. Zackrisson, O. Ljungberg, T. Svahn, P. Timberg, A. Tingberg and I. Andersson. Breast tomosynthesis: Accuracy of tumor measurement compared with digital mammography and ultrasonography. *Acta Radiol.*, 51:240–248, 2010.

[70] I. Andersson, D. M. Ikeda, S. Zackrisson, M. Ruschin, T. Svahn, P. Timberg and A. Tingberg. Breast tomosynthesis and digital mammography: a comparision of breast cancer visibility and birads classification in a population of cancers with subtle mammographic findings. *Eur. Radiol.*, 18:2817–2825, 2008.

[71] J. M. Park, E. A. Franken, M. Garg, L. Fajardo and L. Niklason. Breast tomosynthesis: Present considerations and future applications. *RadioGraphics*, 27:S231–S240, 2007.

[72] R.S. Saunders, E. Samei, J.Y. Lo and J.A. Baker. Can compression be reduced for breast tomosynthesis? monte carlo study on mass and microcalcification conspicuity in tomosynthesis. *Radiology*, 251(3), 2009.

[73] D. Förnvik, I. Andersson, T. Svahn, P. Timberg, S. Zackrisson, and A. Tingberg. The effect of reduced breast compression in breast tomosynthesis: human observer study using clinical cases. *Radiation Protection Dosimetry*, 139(1–3):118–123, 2010.

[74] J. T. Dobbins III and D. J. Godfrey. Digital x-ray tomosynthesis: current state of the art and clinical practice. *Phys. Med. Biol.*, 48:R65–R106, 2003.

[75] E. Y. Sidky, X. Pan, I. S. Reiser et al. Enhanced imaging of microcalcifications in digital breast tomosynthesis through improved image-reconstruction algorithms. *Med. Phys.*, 36:4920–4932, 2009.

[76] E. B. Podgorsak. Radiation physics for medical physicist, chapter interactions of photons with matter. 2en/ed. Germany: Springer, 2010.

[77] F. A. Smith. A primer in applied radiation physics, chapter interaction of photons. World Scientific Publishing Co. Pte. Lda, London, 2000.

[78] ICRP. The 2007 recommendations of the international commission on radiological protection., 2007. ICRP Publication 103. Ann. ICRP 37 (2-4).

[79] H. Benmakhlouf, H. Bouchard, An. Fransson and P. Andreo. Backscatter factors and mass energy-absorption coefficient ratios for diagnostic radiology dosimetry. *Applied Radiation and Isotopes*, 50:185–203, 1999.

[80] D. R. Dance, C. L. Skinner and G. Alm Carlsson. Breast dosimetry. *Applied Radiation and Isotopes*, 50:185–203, 1999.

[81] ICRP. Protection of the patient in nuclear medicine (and statement from the 1987 como meeting of icrp, 1987. ICRP Publication 52. Ann. ICRP 17 (4).

[82] European Comission. European guidelines for quality assurance in breast cancer screening and diagnosis, 2006. Fourth edition. Luxembourg.

[83] M. Karlsson, K. Nygren, G. Wickman and G. Hettinger. Absorbed dose in mammary radiography. *Acta Radiologica Therapy Physics Biology*, 15:252–258, 1976.

[84] D. R. Dance. Monte carlo calculation of conversion factors for the estimation of mean glandular breast dose. *Phys. Med. Biol.*, 35(9):1211–1219, 1990.

[85] D. R. Dance, C. L. Skinner, K. C. Young, J. R. Beckett and C. J. Kotre. Additional factors for the estimation of mean glandular breast dose using the uk mammography dosimetry protocol. *Phys. Med. Biol.*, 45:3225–3240, 2000.

[86] D. R. Dance, K. C. Young and R. E. van Engen. Estimation of mean glandular dose for breast tomosynthesis: factors for use with the uk, european and iaea breast dosimetry protocols. *Phys. Med. Biol.*, 56:453–471, 2011.

[87] R. van Engen, H. Bosmans, R. Bouwman, D. Dance, P. Heid, B. Lazzari, N. Marshall, S. Schopphoven, C. Strudley, M. Thijssen, and K. Young. Protocol for the quality control of the physical and technical aspects of digital breast tomosynthesis systems. EUREF, The Netherlands, 2013.

[88] P. Bernhardt, T. Mertelmeier and M. Hoheisel. X-ray spectrum optimization of full- field digital mammography: Simulation and phantom study. *Medical Physics*, 33(11):4337–13, 2006.

[89] J. Beutel, J. M. Fitzpatrick, S. C. Horii, Y. Kim, H. L. Kundel, M. Sonka and R. L. Van Metter. Handbook of medical imaging: vol.1 physics and phychophysics. SPIE press, Washington (2000).

[90] G. T. Barnes. Contrast and scatter in x-ray imaging. *Radiographics*, 11:307–323, 1991.

[91] S. di Maria, M. Baptista, M. Felix, N. Oliveira, N. Matela, L. Janeiro, P. Vaz, L. Orvalho and A. Silva. Optimal photon energy comparison between digital breast tomosynthesis and mammography: A case study. *Physica Medica*, 30:482–488, 2014.

[92] S. di Maria, P. Oliva, U. Bottiggli, M. Carpinelli and B. Golosio. Image quality simulations in x-ray mammography. *Il Nuovo Cimento*, 124(2):205–222, 2009.

[93] J. M. Boone, B. A. Arnold and J. A. Seibert. Characterization of the point spread function and modulation transfer function of scattered radiation using a digital imaging system. *Medical Physics*, 13(2):254–256, 1986.

[94] G. T. Barnes and I. A. Brezovich. The intensity of scattered radiation in mammography. *Radiology*, 126:243–247, 1978.

[95] J. M. Boone and J. A. Seibert. Monte carlo simulation of the scattered radiation distribution in diagnostic radiology. *Medical Physics*, 15(5):713–720, 1988.

[96] V. N. Cooper III, J. M. Boone, J. A. Seibert and C. J. Pellot-Barakat. An edge spread technique for measurement of the scatter-to-primary ratio in mammography. *Medical Physics*, 27(5):845–853, 2000.

[97] O. Díaz Montesdeoca. Scattered radiation in projection x-ray mammography and digital breast tomosynthesis. (Doctoral dissertation), June 2013.

[98] D. R. Dance, J. Persliden and G. A. Carlsson. Calculation of dose and contrast for two mammographic grids. *Phys. Med. Biol.*, 37(1):235–248, 1992.

[99] D. M. Cunha, A. Tomal and M. E. Poletti. Evaluation of scatter-to-primary ratio, grid performance and normalized average glandular dose in mammography by monte carlo simulation including interface and energy broadening effects. *Phys. Med. Biol.*, 55:4335–4359, 2010.

[100] D. R. Dance and G. J. Day. The computation of scatter in mammography by monte carlo methods. *Phys. Med. Biol.*, 29(3):237–247, 1984.

[101] J. M. Boone, J. A. Selbert, Cha-Mel Tang and S. M. Lane. Grid and slot scan scatter reduction in mammography: Comparison by using monte carlo techniques. *Medical Physics*, 225:519–527, 2002.

[102] U. Neitzel. Grids or air gaps for scatter reduction in digital radiography: A model calculation. *Medical Physics*, 19(2):475–481, 1992.

[103] S. S. J. Feng, C. J. D'Orsi, M. S. Newell, R. L. Seidel, B. Patel and I. Sechopoulos. X-ray scatter correction in breast tomosynthesis with a precomputed scatter map library. *Medical Physics*, 41(3):031912–7, 2014.

[104] A. Krol, D. A. Bassano, C. C. Chamberlain and s. C. Prasad. Scatter reduction in mammography with air gap. *Medical Physics*, 23(7):1263–1270, 1996.

[105] J. H. Siewerden, M. J. Daly, B. Bakhtiar, D. J. Moseleu, S. Richard, H. Keller and D. A. Jaffray. A simple, direct method for x-ray scatter estimation and correction in digital radiography and cone-beam ct. *Medical Physics*, 33(1):187–197, 2006.

[106] J. L. Ducote and S. Molloi. Scatter correction in digital mammography based on image deconvolution. *Phys. Med. Biol.*, 55:1295–1309, 2010.

[107] J. A. Siebert and J. M. Boone. X-ray scatter removal by deconvolution. *Med. Phys.*, 15(4):567–09, 1988.

[108] K. Nykänen and S. Siltanen. X-ray scattering in full-field digital mammography. *Med. Phys.*, 30(7):1864–10, 2003.

[109] Siemens. Mammomat inspiration – digital mammography platform for screening, diagnostic, biopsy and tomosynthesis. Data Sheet.

[110] Gammex Inc. Mammographic phototimer consistency test tool 159a acrylic. United States.

[111] Fantome pour mammographie mtm 100/100r. http://www.xraystore.fr/4514-fantome-pour-mammographie.html. Accessed: 11 August 2016.

[112] PTW. Detectors- including codes of practice, 2011.

[113] F. Salvat and J. M. Fernández-Varea. Overview of physical interaction models for photon and electron transport used in monte carlo codes. *Metrologia*, 46:S112–S138, 2009.

[114] J. M. Berger and S. M. Seltzer. Monte carlo transport of electrons and photons ed t m jenkins et al, 1988. (New York: Plenum) chapters 7–9.

[115] W. R. Nelson, H. Hirayama and D. W. O. Rogers. The egs4 code system, 1985. Report SLAC-265 (Stanford, CA: Stanford Linear Accelerator Center).

[116] F. Salvat, J. M. Fernandez-Varea and J. Sempau. Penélope - 2006: A code system for monte carlo simulation of electron and photon transport., 2006. Barcelona, Spain : Workshop proceedings.

[117] J. Briesmeister. Mcnp - a general monte carlo n-particle transport code version 4c, 2000. Report LA 1265-M. New Mexico, USA : Los Alamos Laboratory.

[118] D. B. Pelonitz. Mcnpx user's manual. report la - cp - 05 - 0369, versão 2.0.5, 2005. USA : Los Alamos International Laboratory.

[119] J. Allison et al. Geant4 developments and applications. *IEEE Trans. Nucl. Sci.*, 53:270–8.

[120] B. Pastircak. Fluka monte carlo simulation code as used for radiation studies in the alice experiment, 2008.

[121] J. Sempau, A. Badal and L. Brualla. A penelope-based system for the automated monte carlo simulation of clinacs and voxelized geometries–application to far-from-axis fields. *Med. Phys.*, 38:5887–5895, 2011.

[122] A. B. i Soler. Development of advanced geometric models and acceleration techniques for monte carlo simulation in medical physics., Aoril 2008.

[123] G. Richard Hammerstein, D. W. Miller, D. R. White, M. E. Masterson, H. Q. Woodard and J. S. Laughlin. Absorbed radiation dose in mammography. *Radiology*, 130:485–491.

[124] Siemens OEM Products. Simulation of x-ray spectra. http://www.oem-products.siemens.com/x-ray-spectra-simulation. Accessed: 1 June 2016.

[125] J. M. Boone and J. A. Seibert. An accurate method for computed-generating tungsten anode x-ray spectra from 30 to 140 kv. *Med. Phys.*, 24(11):1661–1670, 1997.

[126] J. M. Boone, T. R. Fewell and R. J. Jennings. Molybdenum, rhodium, and tungsten anode spectral models using interpolating polynomials with application to mammography. *Med. Phys.*, 24(12):1863–1874, 1997.

[127] W. Rasband. Imagej 1.50i. National Institues of Health, USA, http://imagej.nih.gov/ij. Accessed: 1 June 2016.

[128] J. Zoetelief, M. Fitzgerald, W. Leitz, and M. Sabel. in european protocol on dosimetry in mammography. *EUREF, European Commission, Luxembourg,*, 16263 EN, 1996.

[129] M. Baptista, S. di Maria, C. Figueira, L. Orvalho and P. Vaz. Determination of backscatter factors in breast tomosynthesis using mcnpx simulations and measurements. *Radiation Protection Dosimetry*, pages 1–6, 2015.

[130] L. R. Bradley, A-K Carton and A. D. A. Maidment. Angular dependence of mammographic dosimeters in digital breast tomosynthesis. *Proc. of SPIE*, pages 7622–76255L, 2010.

[131] I. H. R. Hauge and H. M. Olerud. Uncertainties involved in the estimation of mean glandular dose for women in the norwegian breast cancer screening program(nbcsp). *Radiation Protection Dosimetry*, 155(1):81–87, 2013.

[132] I. Sechopoulos, S. S. J. Feng and C. J. D'Orsi. Dosimetric characterization of a dedicated breast computed tomography clinical prototype. *Med. Phys.*, 37(8):4110–4120, 2010.

[133] J. M. Boone, M. H. Buonocore and V. Cooper III. Monte carlo validation in diagnostic radiological imaging. *Medical Physics*, 27(6):1294–1304, 2000.

Appendix A

Conversion factors for MGD calculation

Table A.1: g-factors for different breast thickness and equivalent PMMA thickness [85].

PMMA thickness (mm)	Equiv. breast thickness (mm)	Gland of equiv. breast(%)	g-factors (mGy/mGy) HVL (mm Al)										
			0.30	0.35	0.40	0.45	0.50	0.55	0.60	0.65	0.70	0.75	0.80
20	21	97	0.378	0.421	0.460	0.496	0.529	0.559	0.585	0.609	0.631	0.650	0.669
30	32	67	0.261	0.294	0.326	0.357	0.388	0.419	0.448	0.473	0.495	0.516	0.536
40	45	41	0.183	0.208	0.232	0.258	0.285	0.311	0.339	0.366	0.387	0.406	0.425
45	53	29	0.155	0.177	0.198	0.220	0.245	0.272	0.295	0.317	0.336	0.354	0.372
50	60	20	0.135	0.154	0.172	0.192	0.214	0.236	0.261	0.282	0.300	0.317	0.333
60	75	9	0.106	0.121	0.136	0.152	0.166	0.189	0.210	0.228	0.243	0.257	0.272
70	90	4	0.086	0.098	0.111	0.123	0.136	0.154	0.172	0.188	0.202	0.214	0.227
80	103	3	0.074	0.085	0.096	0.106	0.117	0.133	0.149	0.163	0.176	0.187	0.199

Table A.2: c-factors for different breast thickness and equivalent PMMA thickness [85].

PMMA thickness (mm)	Equiv. breast thickness (mm)	Gland of equiv. breast(%)	g-factors (mGy/mGy) HVL (mm Al)										
			0.30	0.35	0.40	0.45	0.50	0.55	0.60	0.65	0.70	0.75	0.80
20	21	97	0.889	0.895	0.903	0.908	0.912	0.917	0.921	0.924	0.928	0.933	0.937
30	32	67	0.940	0.943	0.945	0.946	0.949	0.952	0.953	0.956	0.959	0.961	0.964
40	45	41	1.043	1.041	1.040	1.039	1.037	1.035	1.034	1.032	1.030	1.028	1.026
45	53	29	1.109	1.105	1.102	1.099	1.096	1.091	1.088	1.082	1.078	1.073	1.068
50	60	20	1.164	1.160	1.151	1.150	1.144	1.139	1.134	1.124	1.117	1.111	1.103
60	75	9	1.254	1.245	1.235	1.231	1.225	1.217	1.207	1.196	1.186	1.175	1.164
70	90	4	1.299	1.292	1.282	1.275	1.270	1.260	1.249	1.236	1.225	1.213	1.200
80	103	3	1.307	1.299	1.292	1.287	1.283	1.273	1.262	1.249	1.238	1.226	1.213

Table A.3: s-factors for different x-ray spectra used in clinical practice [85].

Target material	Filter material	Filter thickness (μ m)	s-factors
Mo	Mo	30	1.000
Mo	Rh	25	1.017
Rh	Rh	25	1.061
W	Rh	50-60	1.042
W	Ag	50-75	1.042

Table A.4: T-factors for different scan ranges [86].

PMMA thickness (mm)	Equivalent breast thickness (mm)	Conversion factor T for projection range of (degrees)				
		-10 to +10	-15 to +15	-20 to +20	-25 to +25	-30 to +30
20	21	0.993	0.988	0.981	0.971	0.959
30	32	0.992	0.985	0.976	0.964	0.949
40	45	0.992	0.983	0.972	0.959	0.943
45	53	0.991	0.982	0.970	0.956	0.940
50	60	0.989	0.981	0.969	0.955	0.939
60	75	0.989	0.980	0.968	0.954	0.938
70	90	0.987	0.977	0.965	0.952	0.937
80	103	0.987	0.976	0.964	0.951	0.934